Excitation and Direct Measurement of Electron Bernstein Waves in a Torus Plasma

Xingyu Guo

Abstract

Electron Bernstein waves (EBWs), generated by a coherent motion of electrons, are a special kind of short-wavelength electrostatic waves in magnetized hot plasmas. EBWs do not have density limits, express a strong cyclotron damping at all harmonics, and can achieve parallel refractive index much larger than one. Therefore, they are very suitable for heating and driving currents in high-beta plasmas in various types of magnetic confinement devices such as stellarator or spherical tokamak, in contrast to the conventional electromagnetic waves. Previous evidence of successful EBW generation mainly came from indirect measurements, such as measurements of plasma energy, density, temperature, soft/hard X-ray, electron Bernstein emission (EBE), H-α, stray microwave radiation, etc. Direct measurement of the wave field was only performed in a few experiments. Up to now, there is no direct observation of two-dimensional (2-D) wave pattern in torus configuration. For this reason, direct measurement experiments were conducted in Low Aspect ratio Torus Experiment (LATE). The purpose of this research is to experimentally verify the whole process of electromagnetic mode propagation, mode conversion, EBW excitation, propagation and damping.

The EBW excitation and detection system consists of a waveguide launcher with arbitrary polarization, a specially designed five-pin probe antenna, a two-dimensional (2-D) mechanical probe driving system, and a homodyne-type mixer circuit. The excitation and detection process is as follows: (1) 2.45 GHz heating microwave ($\sim$400 W) is generated by a continuous-wave (CW) magnetron and injected from 8R port in O-mode obliquely to the toroidal magnetic field. Via O-X-B conversion scheme, an overdense ECR plasma can be produced by EBW of 2.45 GHz microwave, which is uniform along the ECR layer and fills the vacuum vessel. (2) 1.5 GHz detecting microwave ($\sim$20 W) is generated by a RF power generator, mode converted to desired polarization in an open circular waveguide launcher, and eventually, injected into the target plasma from 6R port for EBW excitation. (3) The five-pin probe antenna inserted from the lower part of the LATE device is swept by the 2-D mechanical probe driving system, so the wave field pattern

inside the plasma is measured. (4) The signal received by the probe antenna is sent to the mixer circuit, and time-independent wave pattern is detected by interferometric method.

In the case of O-mode injection, an EBW-like wave pattern has been detected for the first time, in a localized region near the UHR layer. 1-D variation of phase shows that the pattern has a short wavelength of about 2 mm, the pattern has a phase velocity which is directed towards the low field side (outside), and the pattern is electrostatic as the pin detection direction is nearly the same as the wave propagation direction (both almost radial). These characteristics suggest that EBW has been directly observed. The reason for localized observation of the EBW wave pattern is considered to be the critical requirement for achieving high O-X-B mode conversion efficiency, and high collisional damping rate of EBW. In the case of X-mode injection, 2-D wave pattern is quite different from O-mode injection case and no short-wavelength wave pattern can be observed. Under present experimental conditions, the X-B mode conversion efficiency is at a very low level and EBW is not expected to be excited effectively. By slightly adjusting the toroidal magnetic field, both the position and size of the localized EBW region have changed, in accordance with the efficient O-X-B conversion region.

Contents

Chapter 1

Introduction

1.1 Energy crisis and fusion power

Since the middle of the 20th century, global energy consumption has increased dramatically due to economic development and population growth. In 2018, the world's main primary energy sources consisted of petroleum (34%), coal (27%), and natural gas (24%), amounting to an 85% share for nonrenewable fossil fuels in primary energy consumption in the world. The burning of fossil fuels produces around 35 billion tonnes of carbon dioxide (CO_2) per year, or about 89% of all carbon dioxide emissions. Since carbon dioxide is a greenhouse gas that increases radiative forcing, fossil fuels are the main source of greenhouse gas emissions causing global warming and ocean acidification. Non-fossil sources included nuclear (4.4%), hydroelectric (6.8%), and other renewable energy sources (4.0%, including geothermal, solar, tidal, wind, wood, and waste). The share of renewable sources (including traditional biomass) in the world's total final energy consumption was 18% in 2018 [1].

Since renewable energy sources power density per land area is at best three orders of magnitude smaller than fossil or nuclear power, renewable power plants tends to occupy thousands of hectares causing environmental concerns and opposition from local residents, especially in densely populated countries. Besides, renewable electricity production from sources such as wind power and solar power, is variable which results in reduced capacity factor and require energy storage, dispatchable generation and base load power sources from non-intermittent sources. Although nuclear power is considered to be a sustainable energy source that reduces carbon emissions, it poses many threats to people and the environment (i.e., Chernobyl disaster in the Soviet Union in 1986, the Fukushima Daiichi nuclear disaster in Japan in 2011), and it is also too expensive and slow to deploy when compared to

alternative sustainable energy sources.

Fusion power is a proposed form of power generation that would generate electricity by using heat from nuclear fusion reactions. In a fusion process, two or more atomic nuclei are combined to form one or more different atomic nuclei and subatomic particles (neutrons or protons), while releasing energy. Nuclear fusion is also the process that powers active or main sequence stars and other high-magnitude stars. As a source of power, nuclear fusion is expected to have many advantages over nuclear fission. These include reduced radioactivity in operation and little high-level nuclear waste, ample fuel supplies, and increased safety. Research into fusion reactors began in the 1940s, but to date, no design has produced more fusion power output than the electrical power input. The current leading designs are the tokamak and inertial confinement (ICF) by laser. Both designs are under research at very large scales, most notably the International Thermonuclear Experimental Reactor (ITER) in France, and the National Ignition Facility (NIF) in the United States.

1.2 Spherical tokamak and electron cyclotron waves

Thermonuclear fusion processes require fuel and a confined environment with sufficient temperature, pressure, and confinement time to create a plasma. The combination of these figures that results in a power-producing system is known as the Lawson criterion. In a tokamak, a powerful magnetic field is used to confine plasma in the shape of a torus. A measure of success across the magnetic fusion energy world is the beta number β. Every machine containing plasma magnetically, can be compared using this number.

$$\beta = \frac{p}{p_{\mathrm{mag}}} = \frac{nk_{\mathrm{B}}T}{(B^2/2\mu_0)} \tag{1.1}$$

This is the ratio of the plasma pressure to the magnetic field pressure [2]. Improving beta means that you need to use, in relative terms, less energy to generate the magnetic fields for any given plasma pressure (or density). The price of magnets scales roughly with $\sqrt{\beta}$, so reactors operating at higher betas are less expensive for any given level of confinement. Conventional tokamaks operate at relatively low betas, the record being just over 12%, but various calculations show that practical designs would need to operate as high as 20%. The limiting factor in reducing beta is the size of the magnets. Tokamaks use a series of ring-shaped magnets around the confinement area,

and their physical dimensions mean that the hole in the middle of the torus can be reduced only so much before the magnet windings are touching. This limits the aspect ratio, $A = R/a$, of the reactor to about 2.5; the diameter of the reactor as a whole could be about 2.5 times the cross-sectional diameter of the confinement area.

During the 1980s, researchers at Oak Ridge National Laboratory (ORNL), led by Ben Carreras and Tim Hender, were studying the operations of tokamaks as A was reduced. They noticed, based on magnetohydrodynamic considerations, that tokamaks were inherently more stable at low aspect ratios [3]. In 1984, Martin Peng of ORNL proposed an alternate arrangement of the magnet coils that would greatly reduce the aspect ratio while avoiding the erosion issues of the compact tokamak [4]. Instead of wiring each magnet coil separately, he proposed using a single large conductor in the center, and wiring the magnets as half-rings off of this conductor. This layout was named the "spherical tokamak", or ST. These studies suggested that the ST layout would include all the qualities of the advanced tokamak, the compact tokamak, would strongly suppress several forms of turbulence, reach high beta, have high self-magnetism and be less costly to build. Construction of the Small Tight Aspect Ratio Tokamak (START) began in 1990 at Culham, UK, it was assembled rapidly and started operation in January 1991. Its earliest operations quickly put any theoretical concerns to rest. Using ohmic heating alone, START demonstrated betas as high as 12%. START proved Peng and Strickler's predictions; the ST had performance an order of magnitude better than conventional designs, and cost much less to build as well. This sparked off a series of ST developments around the world. In particular, the National Spherical Torus Experiment (NSTX) and Pegasus experiments in the US, Globus-M in Russia, and the UK's follow-on to START, MAST.

In a ST, non-inductive start-up without assistance of central solenoid (CS) is required for realization of low-cost fusion reactors. Among start-up scenarios without CS, use of electron cyclotron heating and current drive (ECH/ECCD) by means of electron cyclotron waves (electromagnetic waves in the electron cyclotron range of frequency, ECWs) is promising, because breakdown and current initiation can be fulfilled simultaneously and the required equipment for microwave power injection is only a small launcher remote from the plasma. The characteristic ability of ECH and ECCD to deposit power or current in a highly localized, robustly controllable way makes these techniques applicable to many objectives not addressable by other heating or current drive approaches. ECH and ECCD have been applied to such objectives as plasma generation and global heating, the support and maintenance of desired profiles of current density and plasma pressure in tokamaks and neutralization of the bootstrap current in stellarators, stabilization of

magnetohydrodynamic (MHD) instabilities like neoclassical tearing modes, and studies of plasma transport through localized heating [5].

The use of electron cyclotron waves has practical advantages as well. Chief among these is that the ECW propagates in vacuum and couples efficiently to the plasma at its boundary, unlike other rf techniques. Furthermore, the wave may propagate as a narrow, well-defined beam. This means that the wave launcher may be distant from the plasma and that the coupling is insensitive to the conditions at the plasma boundary [5].

Although electron cyclotron waves have many distinct advantages, they cannot reach the core region of a high-beta plasma. When the plasma frequency becomes larger than the microwave frequency, ECWs are reflected at the plasma cutoff layer. To overcome this disadvantage, an alternative is the use of so-called electron Bernstein waves (EBWs), which will be introduced next.

1.3 Electron Bernstein waves

Electron Bernstein waves (EBWs) are a special kind of short-wavelength electrostatic waves in magnetized hot plasmas. Unlike the conventional electromagnetic waves, EBWs do not have density limits, so they can efficiently heat over-dense plasmas. Due to their electrostatic character, EBWs can achieve parallel refractive index much larger than one, which is favorable for efficient current drive. The EBWs also express a strong cyclotron damping at all harmonics, which enabled efficient plasma heating [6].

The theory of EBWs was proposed by I. B. Bernstein [7] after whom the waves were named in 1958. EBWs are space charge waves. They do not exist in vacuum and can only be excited inside a magnetized plasma. In a table-top experiment, EBWs can be excited by electrostatic antennas, which are inserted into the plasma. This is not useful for millimeter waves which are necessary in high temperature fusion plasmas, since the antenna structures have to be of the order of the electron gyro radius ($<$0.1 mm). Such structures cannot survive in the high temperature fusion plasma environment. Therefore, only mode conversion from electromagnetic waves is the adequate method to produce EBWs in fusion plasmas. Three mode conversion methods had been proposed: high field side launch, X-B, and O-X-B. The detailed theoretical overview is given in chapter 2. Here we introduce some experiments utilizing these schemes in fusion plasmas.

In 1997, the first EBW heating experiment was demonstrated at the W7-AS stellarator [8]. The experiments were performed with two 70 GHz gyrotrons with 110 kW power each. The central magnetic field was set between

1.25 and 2.0 T and the edge rotational transform, taken from the magnetic reconstruction, near 0.35 according to the experimental requirements. The central density of the neutral beam injection (NBI) sustained target plasma was up to 1.6×10^{20} m^{-3}, which is more than twice the 70 GHz O-mode cutoff density. Co- and counter-NBI, with 380 kW power each, were used to compensate the momentum transfer to the plasma.

Efficient O-X-B heating with 70 GHz electron cyclotron waves was clearly demonstrated for resonant and nonresonant fields. Both, the angular dependence of the O-X conversion and the parametric instability which is typical for X-B conversion, could be experimentally verified. In addition to the heating effect, clear evidence for both mode conversion steps was detected for the first time. Density fluctuations at the cutoff layer play a significant role in the O-X conversion process and need to be taken into account. The results are shown in figure 1.1.

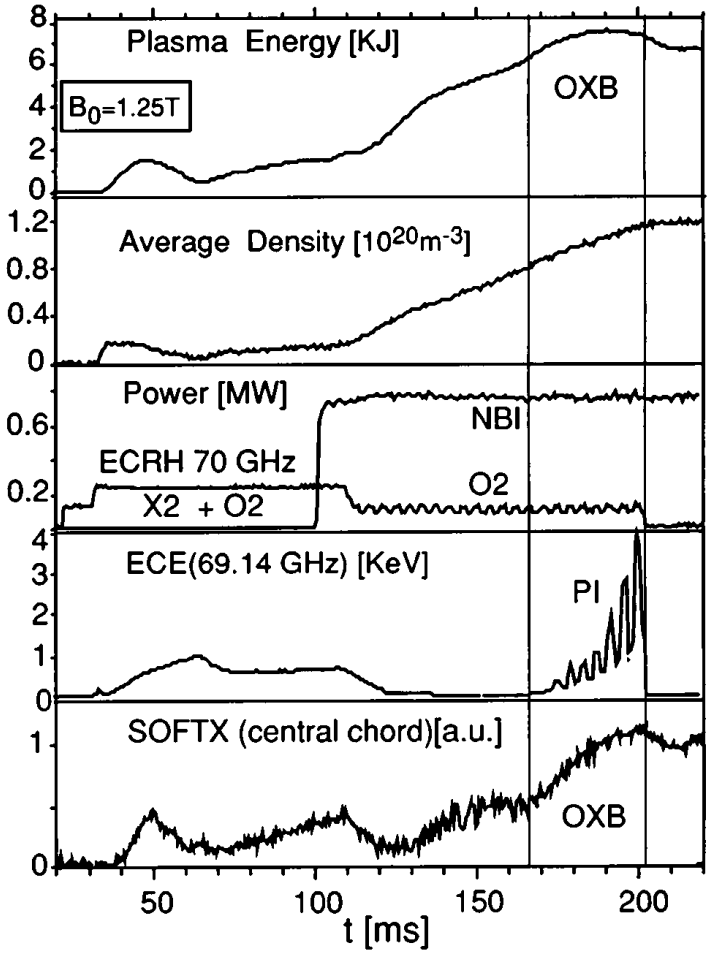

Figure 1.1: Temporal development of some plasma parameters during an O-X-B heated discharge. From the top: plasma energy estimated from the diamagnetic signal, average density from the interferometric measurement, heating power, intensity from ECE and PI, and central soft X signal. The markers show the O-X-B heating interval. Figure from [8].

Later O-X-B experiments were conducted in LHD [9], CHS [10], TCV [11], WEGA [12], MAST [13], LATE [14], etc.

In 2007, the first demonstration of electron-Bernstein-wave heating by double-mode conversion from the O to the X mode in an overdense H-mode tokamak plasma was achieved in the Tokamak à Configuration Variable device [11]. The sensitive dependence of the O-X mode conversion on the microwave launching direction has been verified experimentally, and localized power deposition consistent with theoretical predictions has been observed

at densities well above the conventional cutoff.

High field side launch experiments were performed and shown effective for both heating and current drive in WT-3 [15], COMPASS-D [16], LHD [17] and MAST [18].

In 2001, extraordinary waves were perpendicularly injected for electron Bernstein wave heating into an Ohmically heated plasma from the inboard side in the WT-3 tokamak [15]. The toroidal field is $B_{t0} < 1.75$ T at $R = 65$ cm. The ECH power is generated by a gyrotron (48 GHz, 150 kW maximum), transmitted to a top port via corrugated wave guides, guided into the vacuum vessel through a ceramic vacuum window, and injected perpendicularly to the toroidal field in the form of a Gaussian beam by a couple of mirrors toward a corrugated polarizer attached on the inboard vessel wall.

Measurements show that absorption does not take place at the electron cyclotron resonance layer nor the upper hybrid resonance layer, but does happen midway between them. The poloidal field and poloidal inhomogeneity of toroidal field lead the EBWs to have a large parallel refractive index, and the EBWs are damped away via the Doppler-shifted cyclotron resonance. The results are shown in figure 1.2.

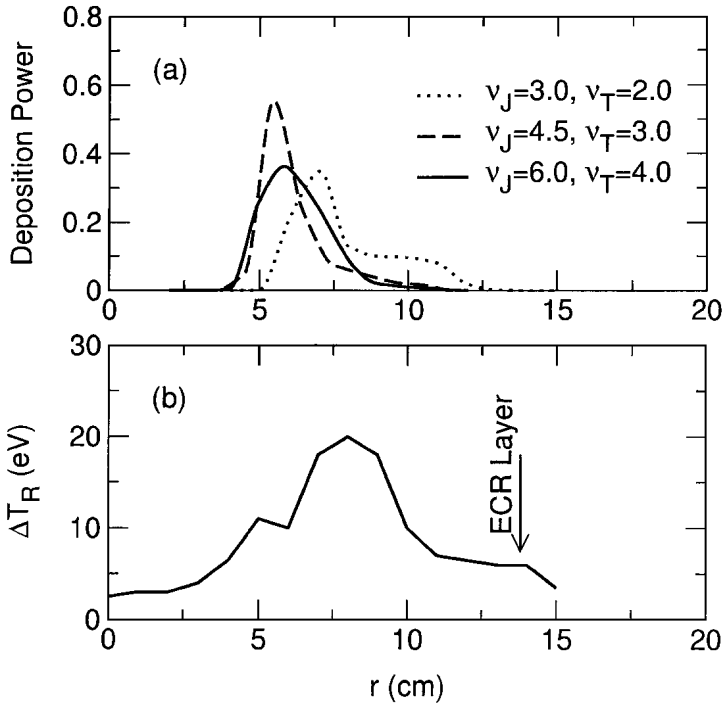

Figure 1.2: Radial profiles of (a) EBW power deposition from multi-ray calculation and (b) decremental ECE radiation temperature. Calculation parameters are $n_0 = 2.16 \times 10^{13}$ cm^{-3}, $T_0 = 480$ eV, $I_\mathrm{p} = 60$ kA, and $\nu_\mathrm{n} = 2$. Figure from [15].

In 2002, electron Bernstein waves were excited in the plasma by mode converted extraordinary waves launched from the high field side of the COMPASS-D tokamak at different toroidal angles [16]. It has been found experimentally that X-mode injection perpendicular to the magnetic field provides maximum heating efficiency. Noninductive currents of up to 100 kA were found to be driven by the EBW mode with countercurrent drive.

Direct X-B heating experiments had been performed at TST-2 [19] and MST [20].

In 2006, an EBW was excited by mode conversion of an X-mode cyclotron wave injected from the low magnetic field side of the TST-2 spherical tokamak [19]. Toroidal magnetic field at major radius ($R = 0.38$ m) $B_\mathrm{t} = 0.3$ T, and plasma current $I_\mathrm{p} = 0.14$ MA. Microwave power (200 kW at 8.2 GHz) was injected through eight horn antennas located on the low-field side of the torus.

Evidence of electron heating was observed as increases in the stored energy and soft x-ray emission. The increased emission was concentrated in the

plasma core region. A heating efficiency of over 50% was achieved, when the density gradient in the mode conversion region was sufficiently steep. The results are shown in figure 1.3.

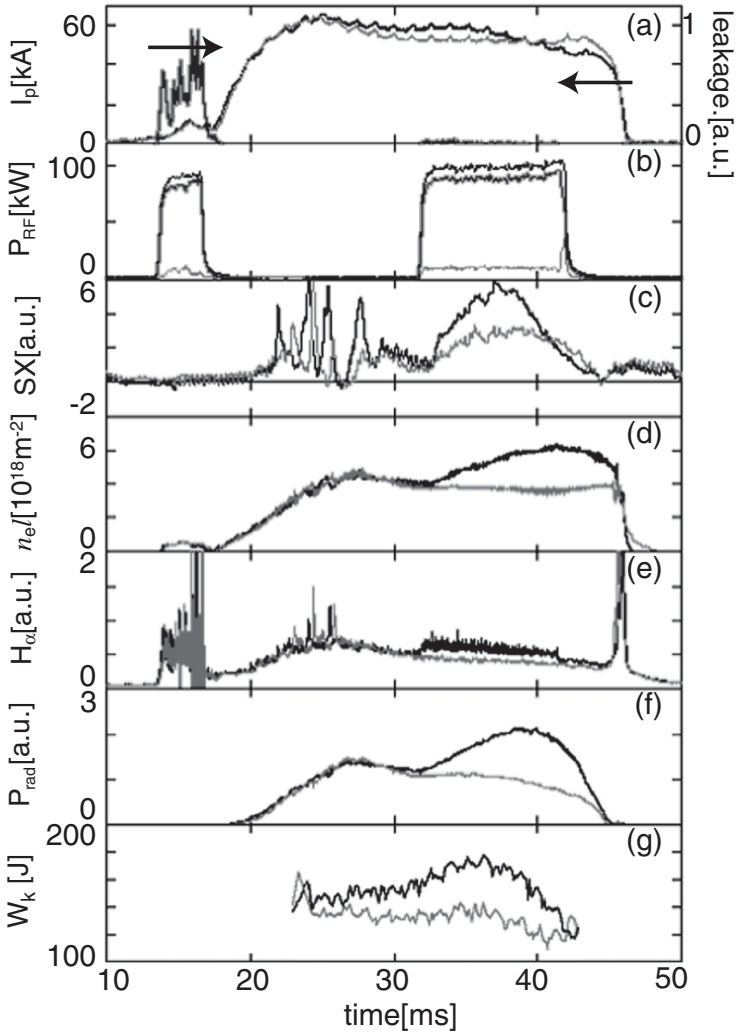

Figure 1.3: Time evolutions of discharges with 90 kW net rf injection (302787 in black) and without rf power (302788 in grey). (a) Plasma current and rf leakage power, (b) forward, reflected, and net rf powers, (c) SX (1–10 keV) emission, (d) line-integrated density at $R = 0.38$ m ($l \approxeq 0.55$ m), (e) H-α (f) P_{rad} (broadband radiation over the range 0.01-7 keV), and (g) plasma stored energy. Figure from [19].

In 2017, the first observation of rf heating in the reversed field pinch (RFP) using the electron Bernstein wave was demonstrated on the Madison

Symmetric Torus, for fundamental and higher harmonics ($n = 17$) utilizing X-B mode conversion in the near field of a waveguide antenna [20]. Propagation across and heating in regions of magnetic stochasticity were demonstrated.

Previous evidence of successful EBW generation mainly came from indirect measurements, such as measurements of plasma energy, density, temperature, soft/hard X-ray, electron Bernstein emission (EBE), H-α, stray microwave radiation, etc. Direct measurement of the wave field was considered to be difficult due to its short wavelength, and was only performed in a few experiments.

In 1981, Sugai observed conversion into short-wavelength Bernstein waves near the UHR in a linear machine with a short wire antenna [21]. The plasma characteristics were $\kappa T_e \cong 1.5$ eV, $\kappa T_i \cong 0.2$ eV, density $n = 10^9 - 10^{12}$ cm^{-3}, diameter $d \cong 70$ cm, length$\cong 3$ m, and uniform axial magnetic field $B_0 < 500$ G. Microwaves of frequencies 0.75-3.0 GHz were launched radially from open-waveguide antennas located outside the plasma column. Spatial profiles of microwave field in the plasma were detected with a short (3 mm) coax-fed wire antenna movable radially. The detected signal was amplified and applied to an interferometer circuit whose output is proportional to the wave power $p(r)\cos(k_\perp r)$. The results are shown in figure 1.4.

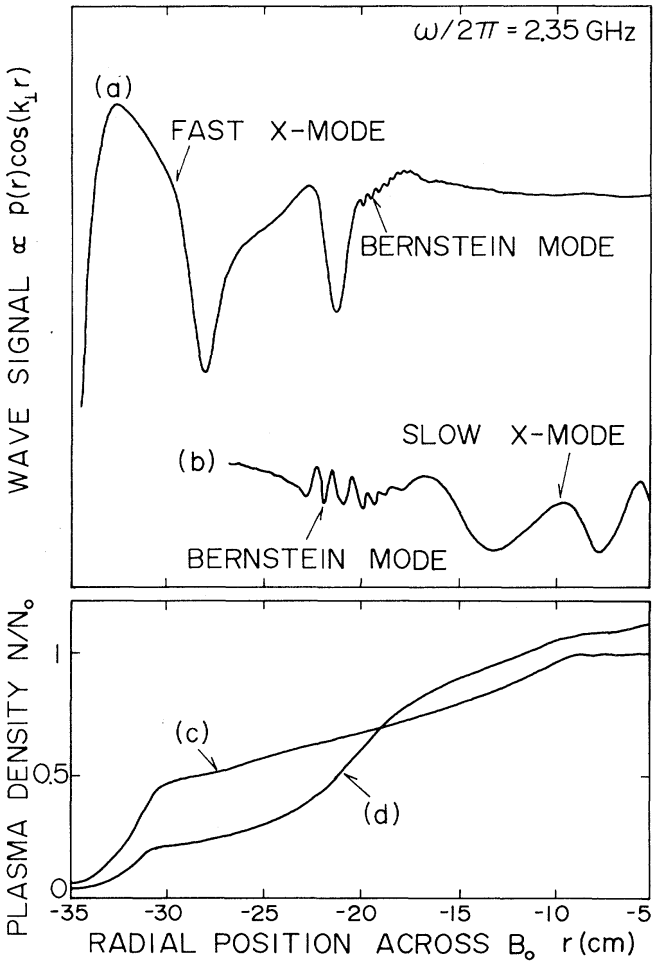

Figure 1.4: Interferometer traces for the microwave incident (a) from outside the plasma at $\omega/\omega_c = 1.95$, and (b) from within the plasma at $\omega/\omega_c = 1.97$, together with (c) gentle and (d) steep radial profiles of the plasma density. Figure from [21].

In 2007, Podoba *et al.* demonstrated conversion from an O-wave to an X-wave by probe measurements of amplitude and phase of the wave field in the WEGA stellarator [12]. The plasma was generated by up to 26 kW of 2.45 GHz electron-cyclotron-resonance heating (ECRH) power in a steady state discharge typically for 30 s in hydrogen, helium, and argon. The electric field of the waves was measured with a small electrostatic probe and the magnetic field of the waves was measured with two magnetic loop probes oriented perpendicular and parallel to the toroidal magnetic field. The results are shown in figure 1.5.

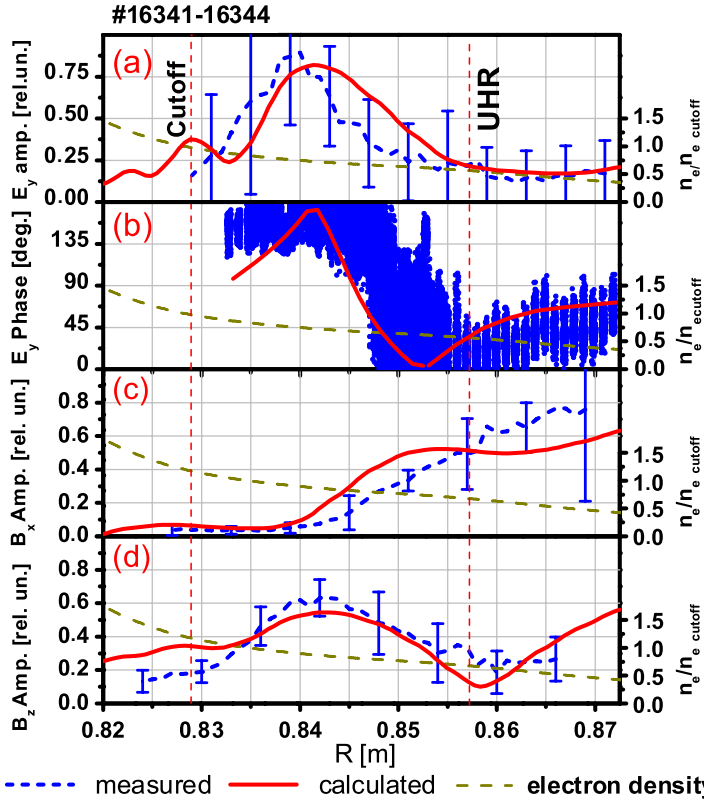

Figure 1.5: Radial profiles of measured and full-wave calculations of E_y amplitude (a), E_y phase (b), B_x (c), and B_z (d) wave components. Calculated (full wave) and measured values are compared. Also the density profile is shown and the locations of the cutoff and the UHR are given. Figure from [12].

In 2015, Uchijima *et al.* conducted direct measurement experiments on the mode conversion to EBW in the Mini-RT by three mode-conversion scenarios. Plasmas were produced and heated by ECH with continuous microwaves at the frequency of 2.45 GHz with a power of 1.0-2.5 kW. Electric and magnetic field profiles were measured by inserting small antennas into plasma. Although observed signals have most characteristics of the EBWs, their wavelengths are about one-order larger than theoretical one [22]. The results are shown in figure 1.6.

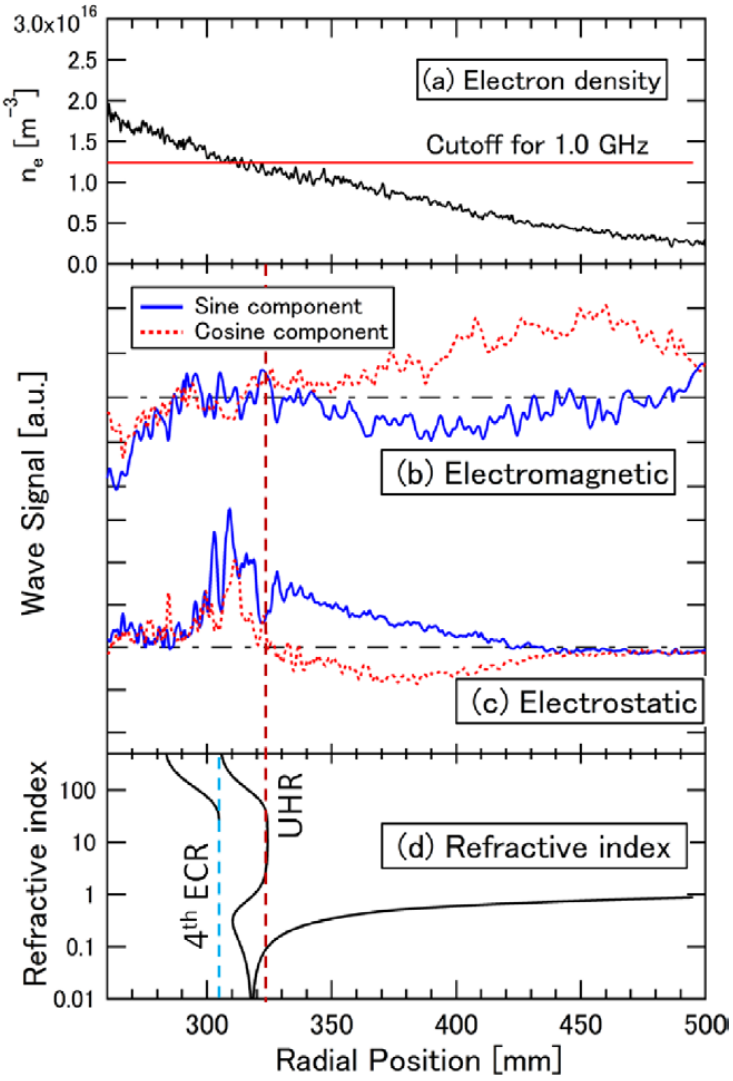

Figure 1.6: (a) An electron density profile, (b) electromagnetic B_z and (c) electrostatic E_x components, and (d) the refractive index for O-X-B conversion experiment. The diagnostic microwave with the frequency of 1.0 GHz is injected from the upper region of the vacuum vessel with the injection angle of $\theta = 71.1^{\circ}$. The P-cutoff for the O-mode is located around $R_{\rm p} = 320$ mm. Figure from [22].

All these direct measurement experiments were limited in one dimension. Up to now, there is no direct observation of two-dimensional (2-D) wave pattern in torus configuration. For this reason, direct measurement experiments were conducted in Low Aspect ratio Torus Experiment (LATE). The purpose

of this research is to experimentally verify the whole process of electromagnetic mode propagation, mode conversion, EBW excitation, propagation and damping.

Chapter 2

Theoretical overview

2.1 Electron cyclotron waves

In the electron cyclotron range of frequency, ion motion can usually be neglected. For a single electron in an electromagnetic field, the equation of motion is

$$m\frac{\mathrm{d}\boldsymbol{v}}{\mathrm{d}t} = q\left(\boldsymbol{E} + \boldsymbol{v} \times \boldsymbol{B}\right) \tag{2.1}$$

The Maxwell equations are

$$\begin{aligned} \nabla \times \boldsymbol{E} &= -\frac{\partial \boldsymbol{B}}{\partial t} \\ \nabla \times \boldsymbol{B} &= \mu_0 \left(\boldsymbol{j} + \epsilon_0 \frac{\partial \boldsymbol{E}}{\partial t}\right) \end{aligned} \tag{2.2}$$

The total current is

$$\boldsymbol{j} = nq\boldsymbol{v} \tag{2.3}$$

Since the plasma has been presumed to be uniform and homogeneous in both space and time, we may Fourier transform these equations as

$$\begin{aligned} \boldsymbol{E} &= \boldsymbol{E}_1 \mathrm{e}^{i(\boldsymbol{k}\cdot\boldsymbol{r}-\omega t)} \\ \boldsymbol{B} &= \boldsymbol{B}_0 + \boldsymbol{B}_1 \mathrm{e}^{i(\boldsymbol{k}\cdot\boldsymbol{r}-\omega t)} \\ \boldsymbol{v} &= \boldsymbol{v}_1 \mathrm{e}^{i(\boldsymbol{k}\cdot\boldsymbol{r}-\omega t)} \end{aligned} \tag{2.4}$$

and $\boldsymbol{B}_0$ is the static magnetic field and is taken to be in the z-direction, and $|\boldsymbol{B}_1| \ll |\boldsymbol{B}_0|$. With these inserted into equation 2.1, we may rewrite that equation in linear form as

$$-i\omega m\boldsymbol{v}_1 = q\left(\boldsymbol{E}_1 + \boldsymbol{v}_1 \times \boldsymbol{B}_0\right) \tag{2.5}$$

where the second order terms have been neglected because we have assumed the waves are of sufficiently low amplitude that the linear approximation is valid. The solution of equation 2.5 for the velocity and current density are

$$\begin{aligned} v_x &= \frac{iq}{m\left(\omega^2-\omega_{\mathrm{c}}^2\right)}\left(\omega E_x + i\omega_{\mathrm{c}} E_y\right) \\ v_y &= \frac{iq}{m\left(\omega^2-\omega_{\mathrm{c}}^2\right)}\left(-i\omega_{\mathrm{c}} E_x + \omega E_y\right) \\ v_z &= \frac{iq}{m\omega} E_z \end{aligned} \tag{2.6}$$

$$\begin{aligned} j_x &= i\epsilon_0 \frac{\omega_{\mathrm{p}}^2}{\left(\omega^2-\omega_{\mathrm{c}}^2\right)}\left(\omega E_x + i\omega_{\mathrm{c}} E_y\right) \\ j_y &= i\epsilon_0 \frac{\omega_{\mathrm{p}}^2}{\left(\omega^2-\omega_{\mathrm{c}}^2\right)}\left(-i\omega_{\mathrm{c}} E_x + \omega E_y\right) \\ j_z &= i\epsilon_0 \frac{\omega_{\mathrm{p}}^2}{\omega} E_z \end{aligned} \tag{2.7}$$

where

$$\omega_{\mathrm{c}} = \frac{qB_0}{m} \tag{2.8}$$

is the cyclotron frequency for electrons and

$$\omega_{\mathrm{p}} = \sqrt{\frac{nq^2}{m\epsilon_0}} \tag{2.9}$$

is the plasma frequency for electrons.

Now combine the plasma current and the displacement current such that

$$\boldsymbol{j} - i\omega\epsilon_0 \boldsymbol{E} = -i\omega\epsilon_0 \boldsymbol{K}\cdot\boldsymbol{E} \tag{2.10}$$

then the resulting equivalent dielectric tensor is given by

$$\boldsymbol{K} = \begin{pmatrix} K_1 & -iK_2 & 0 \\ iK_2 & K_1 & 0 \\ 0 & 0 & K_3 \end{pmatrix} \tag{2.11}$$

where the dielectric tensor elements are defined by

$$
\begin{aligned}
K_1 &= 1 - \frac{\omega_{\mathrm{p}}^2}{\omega^2 - \omega_{\mathrm{c}}^2} \\
K_2 &= \frac{\omega_{\mathrm{c}}\omega_{\mathrm{p}}^2}{\omega\left(\omega^2 - \omega_{\mathrm{c}}^2\right)} \\
K_3 &= 1 - \frac{\omega_{\mathrm{p}}^2}{\omega^2}
\end{aligned}
\tag{2.12}
$$

The Maxwell equations of equation 2.2 are now written as

$$
\begin{aligned}
i\boldsymbol{k} \times \boldsymbol{E} &= i\omega \boldsymbol{B} \\
i\boldsymbol{k} \times \boldsymbol{B} &= -i\omega\epsilon_0\mu_0 \boldsymbol{K} \cdot \boldsymbol{E}
\end{aligned}
\tag{2.13}
$$

the wave equation is

$$
\boldsymbol{N} \times (\boldsymbol{N} \times \boldsymbol{E}) + \boldsymbol{K} \cdot \boldsymbol{E} = 0 \tag{2.14}
$$

where $\boldsymbol{N} = \boldsymbol{k}c/\omega$ is the index of refraction vector whose direction is the direction of the wave vector $\boldsymbol{k}$ and whose magnitude is the index of refraction. Equation 2.14 can be written as

$$
\begin{pmatrix}
K_1 - N_y^2 - N_z^2 & N_x N_y - iK_2 & N_x N_z \\
N_x N_y + iK_2 & K_1 - N_x^2 - N_z^2 & N_y N_z \\
N_x N_z & N_y N_z & K_3 - N_x^2 - N_y^2
\end{pmatrix}
\begin{pmatrix}
E_x \\ E_y \\ E_z
\end{pmatrix} = 0 \tag{2.15}
$$

In order to have a nontrivial solution, one requires that the determinant of coefficients vanish. This condition gives the cold plasma dispersion relation for the electron cyclotron waves

$$
\begin{aligned}
&K_1\left(N_x^4 + N_y^4 + 2N_x^2 N_y^2\right) \\
&- \left[\left(K_3 - N_z^2\right)\left(K_1 + K_3\right) - K_2^2\right]\left(N_x^2 + N_y^2\right) \\
&+ K_3\left[\left(K_1 - N_z^2\right)^2 - K_2^2\right] = 0
\end{aligned}
\tag{2.16}
$$

From the dispersion relation, we can calculate the positions of the cutoff and resonance.

For $N_x = N_y = 0$, we have

$$
K_3\left[\left(K_1 - N_z^2\right)^2 - K_2^2\right] = 0 \tag{2.17}
$$

which gives the plasma cutoff (PC)

$$
\omega = \omega_{\mathrm{p}} \tag{2.18}
$$

left-hand cutoff (LC)

$$\omega = \frac{1}{2}\left(\sqrt{\omega_{\rm c}^2 + \frac{4\omega_{\rm p}^2}{1-N_z^2}} - \omega_{\rm c}\right) = \omega_{\rm L} \tag{2.19}$$

and right-hand cutoff (RC)

$$\omega = \frac{1}{2}\left(\sqrt{\omega_{\rm c}^2 + \frac{4\omega_{\rm p}^2}{1-N_z^2}} + \omega_{\rm c}\right) = \omega_{\rm R} \tag{2.20}$$

For $N_x \to \infty$, we have

$$K_1 = 0 \tag{2.21}$$

which gives the upper hybrid resonance (UHR)

$$\omega = \sqrt{\omega_{\rm c}^2 + \omega_{\rm p}^2} \tag{2.22}$$

The roots of equation 2.16 are plotted in figure 2.1, which gives the fast X (FX), O and slow X (SX) branches.

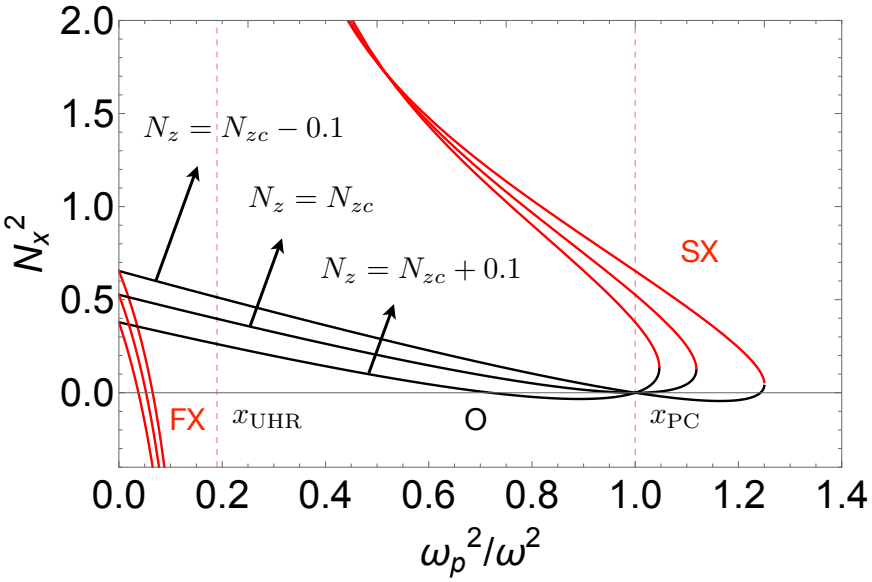

Figure 2.1: The dispersion relation of the electron cyclotron waves for different N_z. $N_{zc} = \sqrt{\omega_{\rm c}/(\omega_{\rm c}+\omega)}$, $\omega_{\rm c}/\omega = 0.9$, $N_y = 0$. The FX, O and SX branches are marked. The positions of the UHR ($x_{\rm UHR}$) and PC ($x_{\rm PC}$) are also marked by vertical dashed lines.

2.2 Electron Bernstein waves

Near the UHR, the wavelength becomes comparable to the electron Larmor radius and the cold plasma approximation breaks down, so it is necessary to consider the finite Larmor radius effect of electrons.

In the unperturbed state, the electrons are motionless in cold plasma. However, in hot plasma, the electrons move along spiral trajectories even in the unperturbed state. The analysis of the behavior due to a perturbation of the system must be based on Boltzmann's equation. The distribution function $f(\boldsymbol{r}, \boldsymbol{v}, t)$ of electrons is given by

$$\begin{aligned}
&\frac{\partial f}{\partial t} + \boldsymbol{v} \cdot \nabla_{\boldsymbol{r}} f + \frac{q}{m}(\boldsymbol{E} + \boldsymbol{v} \times \boldsymbol{B}) \cdot \nabla_{\boldsymbol{v}} f = 0 \\
&\nabla \cdot \boldsymbol{E} = \frac{1}{\epsilon_0} q \int v f \mathrm{d}\boldsymbol{v} \\
&\frac{1}{\mu_0} \nabla \times \boldsymbol{B} = \epsilon_0 \frac{\partial \boldsymbol{E}}{\partial t} + q \int v f \mathrm{d}\boldsymbol{v} \\
&\nabla \times \boldsymbol{E} = -\frac{\partial \boldsymbol{B}}{\partial t} \\
&\nabla \cdot \boldsymbol{B} = 0
\end{aligned} \tag{2.23}$$

We indicate zeroth order quantities (the unperturbed state) by a subscript 0 and the 1st order perturbation terms by a subscript 1. The 1st order terms are expressed in the form of $\mathrm{e}^{i(\boldsymbol{k}\cdot\boldsymbol{r}-\omega t)}$.

$$\begin{aligned}
&f = f_0(\boldsymbol{r}, \boldsymbol{v}) + f_1 \\
&\boldsymbol{B} = \boldsymbol{B}_0 + \boldsymbol{B}_1 \\
&\boldsymbol{E} = 0 + \boldsymbol{E}_1
\end{aligned} \tag{2.24}$$

We can linearize equation 2.23 as follows:

$$\boldsymbol{v}\cdot\nabla_{\boldsymbol{r}}f_0+\frac{q}{m}\left(\boldsymbol{v}\times\boldsymbol{B}_0\right)\cdot\nabla_{\boldsymbol{v}}f_0=0$$

$$q\int f_0\mathrm{d}\boldsymbol{v}=0$$

$$\frac{1}{\mu_0}\nabla\times\boldsymbol{B}_0=q\int\boldsymbol{v}f_0\mathrm{d}\boldsymbol{v}=\boldsymbol{j}_0$$

$$\frac{\partial f_1}{\partial t}+\boldsymbol{v}\cdot\nabla_{\boldsymbol{r}}f_1+\frac{q}{m}\left(\boldsymbol{v}\times\boldsymbol{B}_0\right)\cdot\nabla_{\boldsymbol{v}}f_1=-\frac{q}{m}\left(\boldsymbol{E}_1+\boldsymbol{v}\times\boldsymbol{B}_1\right)\cdot\nabla_{\boldsymbol{v}}f_0 \quad (2.25)$$

$$i\boldsymbol{k}\cdot\boldsymbol{E}_1=\frac{1}{\epsilon_0}q\int f_1\mathrm{d}\boldsymbol{v}$$

$$\frac{1}{\mu_0}\boldsymbol{k}\times\boldsymbol{B}_1=-\omega\left(\epsilon_0\boldsymbol{E}_1+\frac{i}{\omega}q\int\boldsymbol{v}f_1\mathrm{d}\boldsymbol{v}\right)$$

$$\boldsymbol{B}_1=\frac{1}{\omega}\left(\boldsymbol{k}\times\boldsymbol{E}_1\right)$$

The dielectric tensor of the hot plasma is defined by

$$\boldsymbol{E}_1+\frac{i}{\epsilon_0\omega}\boldsymbol{j}=\boldsymbol{E}_1+\frac{i}{\epsilon_0\omega}q\int\boldsymbol{v}f_1\mathrm{d}\boldsymbol{v}=\boldsymbol{K}\cdot\boldsymbol{E}_1 \quad (2.26)$$

The linear relation of $\boldsymbol{E}_1$ is

$$\boldsymbol{k}\times\left(\boldsymbol{k}\times\boldsymbol{E}_1\right)+\frac{\omega^2}{c^2}\boldsymbol{K}\cdot\boldsymbol{E}_1=0 \quad (2.27)$$

and the dispersion relation is obtained by equating the determinant of the coefficient matrix of the linear equation to zero. Consequently if f_1 can be solved from equation 2.26, then, $\boldsymbol{K}$ can be obtained.

We assume a Maxwellian velocity distribution function and neglect relativistic effects. After a lengthy and formidable derivation, the hot plasma dielectric tensor can be obtained as

$$\boldsymbol{K}=\mathbf{1}+\frac{\omega_{\mathrm{p}}^2}{\omega^2}\zeta_0\sum_{\mathrm{n}=-\infty}^{\infty}\boldsymbol{S}_{\mathrm{n}} \quad (2.28)$$

where

$$\boldsymbol{S}_{\mathrm{n}}=\begin{bmatrix}\frac{\mathrm{n}^2}{\mu}\widetilde{I}_{\mathrm{n}}Z_{\mathrm{n}} & i\mathrm{n}\widetilde{I}_{\mathrm{n}}Z_{\mathrm{n}} & -\mathrm{n}\sqrt{\frac{2}{\mu}}\widetilde{I}_{\mathrm{n}}\left(1+\zeta_{\mathrm{n}}Z_{\mathrm{n}}\right)\\ -i\mathrm{n}\widetilde{I}_{\mathrm{n}}Z_{\mathrm{n}} & \left(\frac{\mathrm{n}^2}{\mu}\widetilde{I}_{\mathrm{n}}-2\mu\widetilde{I}_{\mathrm{n}}\right)Z_{\mathrm{n}} & i\sqrt{2\mu}\widetilde{I}_{\mathrm{n}}\left(1+\zeta_{\mathrm{n}}Z_{\mathrm{n}}\right)\\ -\mathrm{n}\sqrt{\frac{2}{\mu}}\widetilde{I}_{\mathrm{n}}\left(1+\zeta_{\mathrm{n}}Z_{\mathrm{n}}\right) & -i\sqrt{2\mu}\widetilde{I}_{\mathrm{n}}\left(1+\zeta_{\mathrm{n}}Z_{\mathrm{n}}\right) & 2\zeta_n\widetilde{I}_{\mathrm{n}}\left(1+\zeta_{\mathrm{n}}Z_{\mathrm{n}}\right)\end{bmatrix}$$

(2.29)

and

$$
\begin{aligned}
&\zeta_{\mathrm{n}} = \left(\omega + \mathrm{n}\omega_{\mathrm{c}}\right) / \left(\left|k_z\right| v_{\mathrm{th}}^2\right) \\
&\mu = 0.5 k_{\perp}^2 v_{\mathrm{th}}^2 / \omega_{\mathrm{c}}^2 \\
&v_{\mathrm{th}} = \left(2 k_{\mathrm{B}} T / m\right)^{1/2} \\
&\widetilde{I}_{\mathrm{n}} = \mathrm{e}^{-\mu} I_{\mathrm{n}}(\mu) \\
&Z_{\mathrm{n}} = Z\left(\zeta_{\mathrm{n}}\right) \\
&Z\left(\zeta_{\mathrm{j}}\right) = \frac{1}{\sqrt{\pi}} \int_{-\infty}^{\infty} \frac{\mathrm{e}^{-s^2}}{s - \zeta_{\mathrm{j}}} \mathrm{d}s
\end{aligned}
\tag{2.30}
$$

k_{B} is the Boltzmann constant and I_{n} is nth modified Bessel function of the first kind.

The hot plasma dielectric tensor is a not only a function of ω_{c} and ω_{p} but also a function of the temperature and the wave vector $\boldsymbol{k}$. This leads to a new kind of solutions of the dispersion relation, the electrostatic modes. The sum over the Bessel functions gives rise to a large number of possible roots for a given $\boldsymbol{N}$. These new waves are named electron Bernstein waves (EBWs), in honor of I. B. Bernstein and of his fundamental paper in 1958 [7].

EBWs are electrostatic waves propagating at right angles to $\boldsymbol{B}_0$ at harmonics of the electron cyclotron frequency. They are generated by a coherent motion of electrons around their guiding center, which are characterized by wavelength of the order of four times the electron Larmor radius, as shown in figure 2.2.

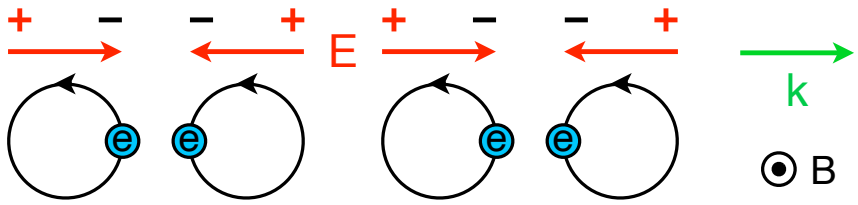

Figure 2.2: A schematic diagram of the EBW propagation (periodic charge accumulation).

To get the dispersion relation of EBW, the electric field $\boldsymbol{E}$ of waves is expressed by electrostatic potential ϕ

$$
\boldsymbol{E} = -\nabla\phi \tag{2.31}
$$

Since

$$\begin{aligned} \frac{\partial \boldsymbol{B}_1}{\partial t} &= \nabla \times \boldsymbol{E} \\ \boldsymbol{B}_1 &= \frac{\boldsymbol{k} \times \boldsymbol{E}}{\omega} = 0 \end{aligned} \tag{2.32}$$

the dispersion relation is reduced from Poisson's equation to

$$k_x^2 K_{xx} + 2k_x k_z K_{xz} + k_z^2 K_{zz} = 0 \tag{2.33}$$

After simplification, we obtain the general dispersion relation for electron Bernstein waves:

$$1 + \frac{\omega_{\mathrm{p}}^2 k_x^2}{\omega_{\mathrm{c}}^2 \mu} \frac{1}{k_x^2 + k_z^2} \mathrm{e}^{-\mu} \sum_{\mathrm{n}=-\infty}^{\infty} I_{\mathrm{n}}(\mu) \left(1 + \zeta_0 Z_{\mathrm{n}}\right) = 0 \tag{2.34}$$

For high-frequency waves in which the ions do not move, they are not sensitive to small deviations from perpendicular propagation, and we may set $k_z = 0$, so that $\zeta_{\mathrm{n}} \to \infty$. For large ζ_n, we may replace Z_{n} by $-1/\zeta_{\mathrm{n}}$. The $\mathrm{n} = 0$ term in the second sum of equation 2.34 then cancels out, and we can divide the sum into two sums, as follows:

$$k_x^2 + \frac{\omega_{\mathrm{p}}^2 k_x^2}{\omega_{\mathrm{c}}^2 \mu} \mathrm{e}^{-\mu} \left(\sum_{\mathrm{n}=1}^{\infty} I_{\mathrm{n}}(\mu) \left(1 - \zeta_0/\zeta_{\mathrm{n}}\right) + \sum_{\mathrm{n}=1}^{\infty} I_{-\mathrm{n}}(\mu) \left(1 - \zeta_0/\zeta_{-\mathrm{n}}\right) \right) = 0 \tag{2.35}$$

or

$$k_x^2 + \frac{\omega_{\mathrm{p}}^2 k_x^2}{\omega_{\mathrm{c}}^2 \mu} \mathrm{e}^{-\mu} \sum_{\mathrm{n}=1}^{\infty} I_{\mathrm{n}}(\mu) \left(2 - \frac{\omega}{\omega + \mathrm{n}\omega_{\mathrm{c}}} - \frac{\omega}{\omega - \mathrm{n}\omega_{\mathrm{c}}} \right) = 0 \tag{2.36}$$

The bracket collapses to a single term upon combining over a common denominator, which is the well-known $k_z = 0$ dispersion relation

$$1 = \frac{\omega_{\mathrm{p}}^2}{\omega_{\mathrm{c}}^2} \frac{2}{\mu} \mathrm{e}^{-\mu} \sum_{\mathrm{n}=1}^{\infty} \frac{I_{\mathrm{n}}(\mu)}{\left(\omega/\mathrm{n}\omega_{\mathrm{c}}\right)^2 - 1} \tag{2.37}$$

as shown in figure 2.3.

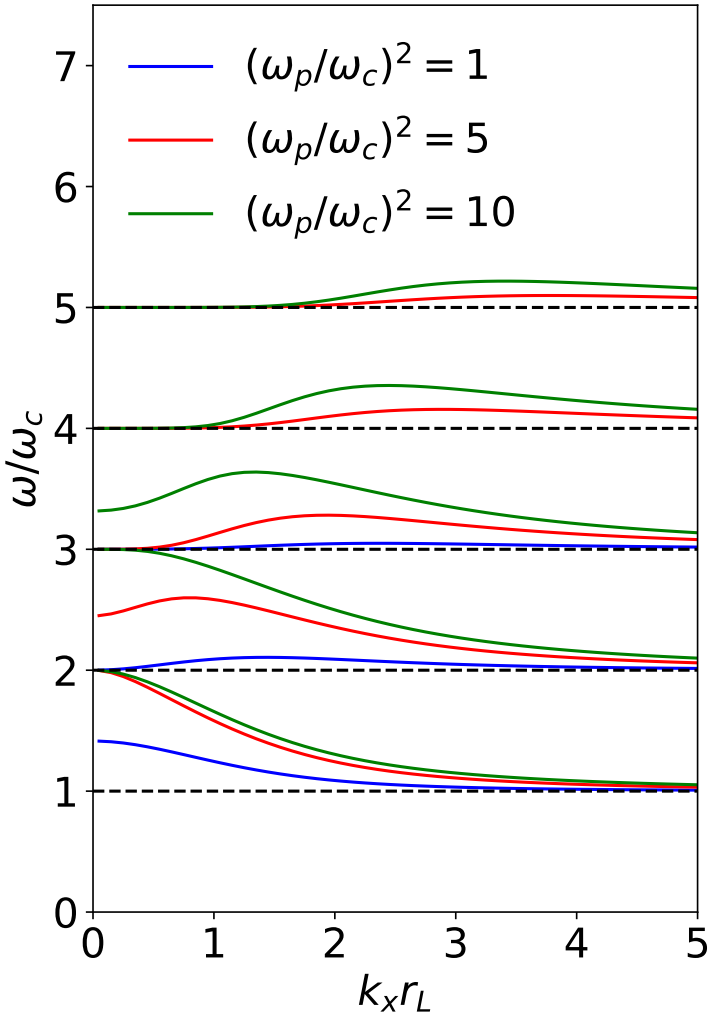

Figure 2.3: The dispersion relation of EBW.

The main characteristics of EBW are: (1) no cutoff density, (2) electrostatic mode, (3) short wavelength (same order with electron Larmor radius), (4) backward wave.

2.3 Mode conversion

EBWs are space charge waves. They do not exist in vacuum and can only be excited inside a magnetized plasma. Therefore, mode conversion from electromagnetic waves is required for excitation. Three mode conversion methods had been proposed.

The first method, called high field side launch, is to launch the first harmonic X-wave from the high field side. The slow X-wave (SX-mode) approaches the upper hybrid resonance (UHR) and is converted to EBWs. The second method, called direct X-B conversion, is to launch an X-wave from vacuum into plasma. The fast X-wave (FX-mode) tunnels through the evanescent region between the right-hand cutoff (RC) and UHR and couples to the SX-mode, which eventually converts to EBWs at the UHR [23]. The third method, called O-X-B conversion, is to launch an O-wave (O-mode) from the outside with an oblique angle of incidence. For an optimal injection angle there is a coincidence of the plasma cutoff (PC) and left-hand cutoff (LC), which means that the O-mode will be totally converted to the SX-mode. Then the SX-mode propagates back to the UHR and is converted to EBWs [24, 25].

Here we discuss the O-X-B mode conversion in some details. The O-X-B mode conversion consists of two processes, the O-SX conversion and the SX-B conversion.

2.3.1 O-SX conversion

For the O-SX conversion, assume that both the electron density and magnetic field changes linearly in one dimension as

$$\begin{aligned} \omega_{\mathrm{p}}^2 &= \omega^2 \left(1 + \frac{x}{L_n}\right) \\ \omega_{\mathrm{c}} &= \omega_{\mathrm{c0}} \left(1 + \frac{x}{L_B}\right) \end{aligned} \tag{2.38}$$

where L_n and L_B are the density and magnetic field scale lengths, respectively. If these inhomogeneity scale lengths are much larger than the wavelength, $k_0 L_n \gg 1$ and $k_0 L_B \gg 1$, the solution of the wave equation can be expressed as the WKB approximation

$$\mathbf{E} = \mathbf{E}_0(x) \exp\left[ik_y y + ik_z z + \int ik_x\left(x'\right) \mathrm{d}x' - i\omega t\right] \tag{2.39}$$

where $\mathbf{E}_0$ and k_x are slow-varying functions of x. The coordinate system is shown in figure 2.4.

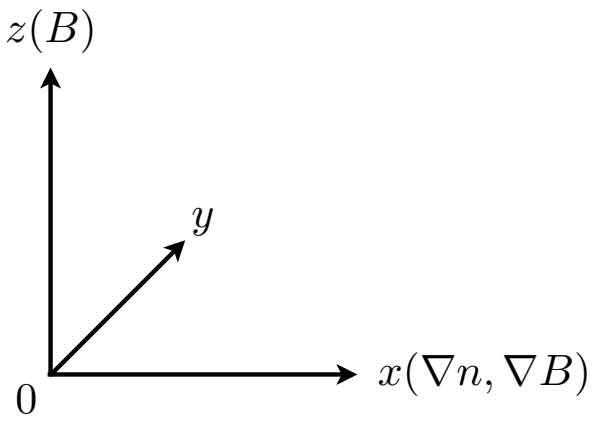

Figure 2.4: The coordinate system.

The localized dispersion relation from the WKB approximation has the same form as equation 2.16. To understand the behavior of the dispersion relation near the plasma cutoff with an injection angle close to the optimal value, the following assumptions are made

$$\begin{aligned} &N_x \sim O(\epsilon) \\ &N_y \sim O(\epsilon) \\ &K_3 \sim O(\epsilon) \\ &\sqrt{K_1 + K_2} - N_z \sim O(\epsilon) \end{aligned} \tag{2.40}$$

where ϵ is first-order small variable.

Now we can neglect third-order and fourth-order terms in equation 2.16, the simplified dispersion relation is

$$N_x^2 = -N_y^2 + \frac{4\left(\sqrt{K_1 + K_2} - N_z\right) K_3}{\sqrt{K_1 + K_2}} \tag{2.41}$$

Substitute equation 2.38 into equation 2.41, expand near $x = 0$ and neglect third-order and fourth-order terms, we have

$$N_x^2 = -N_y^2 + \frac{2\omega\left(L_B - N_{zc}^2 L_n\right) x^2}{\omega_{c0} L_B L_n^2} + \frac{4\left(N_z - N_{zc}\right) x}{N_{zc} L_n} \tag{2.42}$$

where

$$N_{zc} = \sqrt{\frac{\omega_{c0}}{\omega_{c0} + \omega}} \tag{2.43}$$

The O-SX conversion efficiency can be obtained by continuing the WKB solution through the evanescent region along the decaying branch as

$$C_{\mathrm{O-SX}} = \exp\left(-2\left|\mathrm{Im}\int_{x_{\mathrm{PC}}}^{x_{\mathrm{LC}}} k_x \mathrm{d}x\right|\right) \tag{2.44}$$

where the integration domain is the width of the evanescent region between the PC and LC. By using the following formula

$$\int_{x_{\mathrm{PC}}}^{x_{\mathrm{LC}}} \left[\left(x - x_{\mathrm{PC}}\right)\left(x - x_{\mathrm{LC}}\right)\right]^{1/2} \mathrm{d}x = i\frac{\pi}{8}\left(x_{\mathrm{PC}} - x_{\mathrm{LC}}\right)^2 \tag{2.45}$$

the O-SX conversion efficiency can be calculated as

$$\begin{aligned} C_{\mathrm{O-SX}} = \exp\Bigg[&-\pi k_0 L_n \sqrt{\frac{\omega_{\mathrm{c0}}}{2\omega}} \\ &\times \frac{2(1+\omega_{\mathrm{c0}}/\omega)\left(N_z - N_{zc}\right)^2 + {N_y}^2\left(1 - L_n {N_{zc}}^2/L_B\right)}{\left(1 - L_n {N_{zc}}^2/L_B\right)^{3/2}}\Bigg] \end{aligned} \tag{2.46}$$

When $L_B \to \infty$, $\omega_{\mathrm{c0}} = \omega_{\mathrm{c}}$, equation 2.46 reduces to the well-known formula for the O-SX conversion efficiency [25]

$$C_{\mathrm{O-SX}} = \exp\left\{-\pi k_0 L_n \sqrt{\frac{\omega_{\mathrm{c}}}{2\omega}}\left[2\left(1 + \frac{\omega_{\mathrm{c}}}{\omega}\right)\left(N_z - N_{zc}\right)^2 + N_y^2\right]\right\} \tag{2.47}$$

From equation 2.46, it can be seen that the magnetic field gradient decreases the O-SX conversion efficiency and it has opposite effect to the density gradient. According to equations 2.46 and 2.47, the conversion efficiencies as functions of N_z are plotted in figure 2.5. Clearly, the optimal parallel refractive index for the O-SX conversion is not affected by L_B, but the conversion window is slightly narrowed due to the increase of the tunneling length.

For comparison, a kinetic full wave simulation is performed. The details are given in chapter 5 and the numerical results are also plotted in figure 2.5.

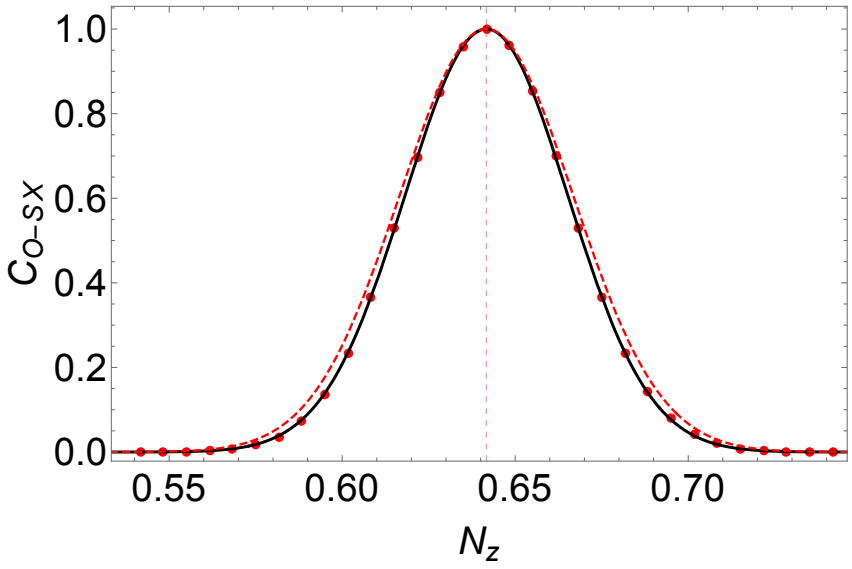

Figure 2.5: The O-SX conversion efficiency as a function of N_z. The parameters are chosen as $k_0 L_n = 40\pi$, $k_0 L_B = 200\pi$, $\omega_{c0}/\omega = 0.7$, $N_y = 0$. The solid and dashed lines are results from equations 2.46 and 2.47, respectively. The dots are the numerical results.

It is shown that in the WKB regime, the analytical expression of the O-SX conversion efficiency given in equation 2.46 agrees very well with the numerical results. For large fusion devices, $k_0 \sim 500$ m^{-1}, $L_\mathrm{B} \sim 1$ m, and effect of the magnetic field gradient is negligible. For small fusion devices, $k_0 \sim 50$ m^{-1}, $L_\mathrm{B} \sim 0.1$ m, while $L_n \sim 0.05$ m, so the conversion window is much wider and effect of the magnetic field gradient is still negligible.

2.3.2 SX-B conversion

For the SX-B conversion, the dispersion relation for the X-mode is

$$N_x^2 = \frac{d_1 - \sqrt{d_2}}{2K_1} \tag{2.48}$$

where

$$\begin{aligned} d_1 =& -2K_1 N_y^2 - (K_1 + K_3) N_z^2 + \left(K_1^2 + K_1 K_3 - K_2^2\right) \\ d_2 =& \left(-K_1^2 + K_1 K_3 + K_2^2\right)^2 \\ &+ N_z^2 \left[\left(N_z^2 - 2K_1\right)(K_3 - K_1)^2 + 2(K_3 + K_1) K_2^2\right] \end{aligned} \tag{2.49}$$

Choose the position of the UHR as $x = 0$ and assume that both the electron density and magnetic field changes linearly in one dimension as

$$\begin{aligned}
\omega_{\mathrm{p}}^2 &= \omega_{\mathrm{pU}}^2 \left(1 + \frac{x}{L_n}\right) \\
\omega_{\mathrm{c}} &= \omega_{\mathrm{cU}} \left(1 + \frac{x}{L_B}\right) \\
\alpha &= \frac{\omega_{\mathrm{pU}}}{\omega_{\mathrm{cU}}}
\end{aligned} \tag{2.50}$$

The dielectric tensor components can be expanded at the UHR as

$$\begin{aligned}
K_1 &= K_1' x \\
K_2 &= \frac{1}{\sqrt{1+\alpha^2}} + K_2' x \\
K_3 &= \frac{1}{1+\alpha^2} + K_3' x
\end{aligned} \tag{2.51}$$

where

$$\begin{aligned}
K_1' &= -\frac{2}{\alpha^2 L_B} - \frac{1}{L_n} \\
K_2' &= \frac{2L_n + \alpha^2 \left(L_B + L_n\right)}{\alpha^2 L_B L_n \sqrt{1+\alpha^2}} \\
K_3' &= -\frac{\alpha^2}{\left(1+\alpha^2\right) L_n}
\end{aligned} \tag{2.52}$$

The dispersion relation for the X-mode can be modeled as a cutoff-resonance pair (which is equivalent to the Budden potential)

$$N_x^2 = d_3 + \frac{d_4}{x} \tag{2.53}$$

where

$$\begin{aligned}
d_3 &= -\frac{N_z^2}{1+N_z^2}\frac{\alpha^2}{1+\alpha^2} - \frac{N_z^2 K_3'}{K_1'} - N_y^2 - \frac{2K_2'}{\sqrt{1+\alpha^2} K_1'} \\
d_4 &= -\frac{1+N_z^2}{\left(1+\alpha^2\right) K_1'}
\end{aligned} \tag{2.54}$$

The modeled cutoff-resonance pair is shown in figure 2.6.

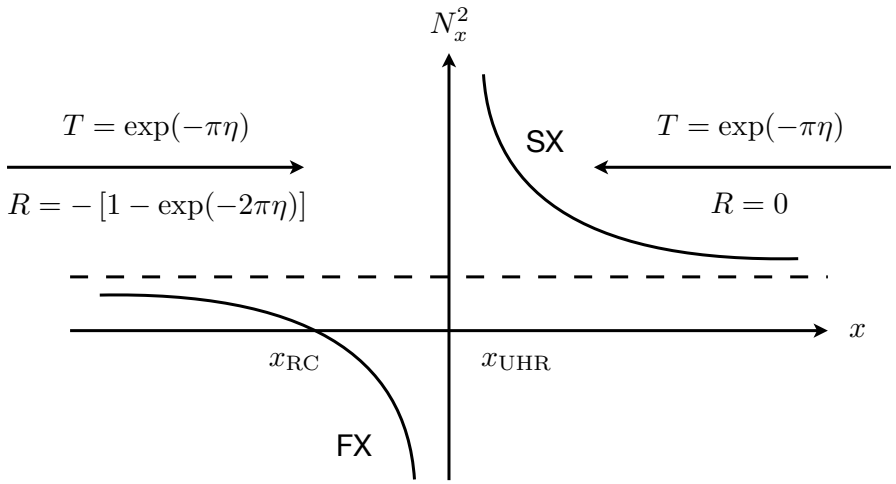

Figure 2.6: The modeled cutoff-resonance pair for the X-mode dispersion relation.

The normalized distance between the UHR and the RC (the width of the evanescent region) is

$$\Delta = k_0 \left| x_{\mathrm{UHR}} - x_{\mathrm{RC}} \right| \tag{2.55}$$

For $L_B \to \infty$ and $N_y = 0$, equation 2.55 can be reduced to

$$\Delta = \frac{k_0 L_n \left(1 + N_z^2\right)^2}{\alpha^2 N_z^2 \left(2 + N_z^2\right)} \tag{2.56}$$

It is clear that for $k_0 L_n \gg 1$, the width of the evanescent region between the UHR and the RC is large, so the tunneling loss of the SX-mode can be neglected and the SX-B conversion is almost perfect. However, for $k_0 L_n < 1$, the tunneling loss cannot be neglected and the SX-B conversion is not perfect.

For the Budden problem, the tunneling factor is given by

$$\eta = k_0 d_4 / \sqrt{d_3} \tag{2.57}$$

Since the process only involves conversion and transmission, the SX-B conversion efficiency can be given as

$$C_{\mathrm{SX-B}} = 1 - \exp(-\pi\eta) \tag{2.58}$$

For $L_B \to \infty$ and $N_y = 0$, equation 2.58 can be reduced to

$$C_{\mathrm{SX-B}} = 1 - \exp\left\{ \frac{-\pi k_0 L_n \left(1 + N_z^2\right)}{\sqrt{\left(1 + \alpha^2\right)\left[2 - \alpha^2 N_z^2 - \alpha^2 N_z^2 / \left(1 + N_z^2\right)\right]}} \right\} \tag{2.59}$$

From equation 2.59 it can be seen that the SX-B conversion efficiency increases with paralel refractive index monotonically.

The total O-SX-B conversion efficiency can be written as

$$C_{\mathrm{O-SX-B}} = C_{\mathrm{O-SX}} C_{\mathrm{SX-B}} \tag{2.60}$$

Since $C_{\mathrm{SX-B}}$ is smaller than unity and increases with N_z monotonically, the O-SX-B conversion window will be suppressed and shifted compared with the O-SX conversion. That is, the optimal parallel refractive index for the O-SX-B conversion should be larger than conventional optimal value in equation 2.47.

Assume $N_y = 0$, the optimal parallel refractive index for the O-SX-B conversion can be approximately obtained by finding the maximum of $C_{\mathrm{O-SX-B}}$

$$N_{zc-\mathrm{O-SX-B}} \simeq N_{zc} + \frac{\mathrm{e}^{-\pi\eta(N_{zc})}\eta'\left(N_{zc}\right)}{a\left[1-\mathrm{e}^{-\pi\eta(N_{zc})}\right]} \tag{2.61}$$

where

$$\begin{aligned} a &= \frac{2k_0 L_n \sqrt{2(\omega_{\mathrm{c0}}/\omega)}(1+\omega_{\mathrm{c0}}/\omega)}{\left(1-N_{zc}^2 L_n/L_B\right)^{3/2}} \\ \eta'\left(N_{zc}\right) &= \left.\frac{\partial\eta}{\partial N_z}\right|_{N_z=N_{zc}} \end{aligned} \tag{2.62}$$

To further show the influence of this shift, the O-SX, SX-B and O-SX-B conversion efficiencies as functions of N_z are plotted in figure 2.7. The O-SX-B conversion efficiencies calculated from kinetic full wave simulation are also plotted in figure 2.7.

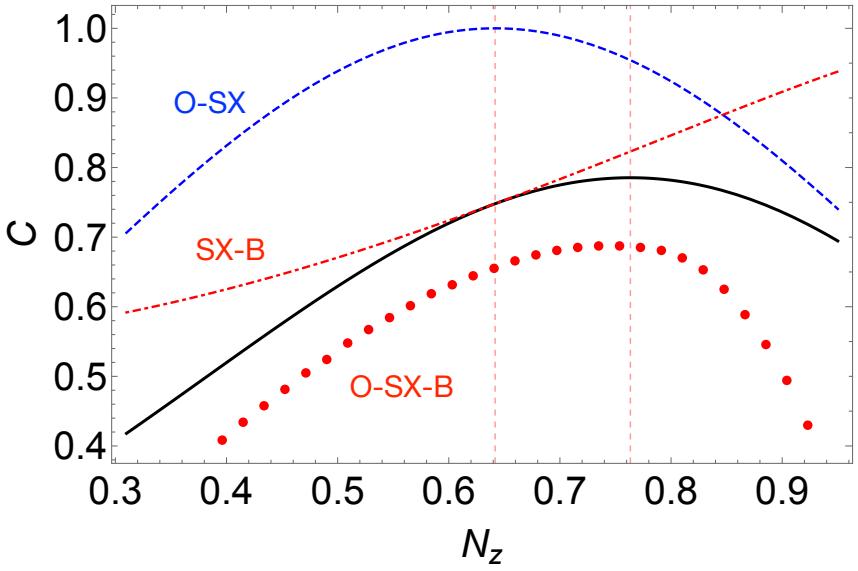

Figure 2.7: The O-SX (dashed), SX-B (dotdashed) and O-SX-B (solid) conversion efficiencies as functions of N_z. The parameters are chosen as $k_0 L_n = 0.5$, $\alpha = 1$, $\omega_c/\omega = 0.7$, $N_y = 0$. The solid, dashed and dotdashed lines are results from equations 2.60, 2.47 and 2.59, respectively. The dots are the numerical results.

Here in figure 2.7, $k_0 L_n = 0.5$, the degradation of the total conversion efficiency and the shift of the optimal parallel refractive index are both obvious. For large fusion devices, $k_0 \sim 500$ m^{-1}, $L_n \sim 0.5$ m, and these effects are negligible. For small fusion devices, $k_0 \sim 50$ m^{-1}, $L_n \sim 0.05$ m, and these effects are non-negligible for certain cases, such as steep density profile where $k_0 L_n < 1$.

Chapter 3

Experimental setup

3.1 LATE device

The Low Aspect ratio Torus Experiment (LATE) is a spherical tokamak which has no central solenoid and aims to generate plasmas using only microwaves in the electron cyclotron range of frequency. Major and minor radius of the device are 28 and 22 cm, respectively. The main components of LATE consist of the vacuum vessel, the vacuum pump, the gas introduction system, the toroidal and vertical magnetic field coils, and the microwave injection system.

3.1.1 Vacuum vessel

The vacuum vessel of LATE is a stainless steel cylinder with an inner diameter of 100 cm and an inner height of 100 cm. The vessel has 6 circular ports on the top, bottom, and radial side (called T port, B port, and R port, respectively). Each port is numbered clockwise when viewed from above, as shown in figure 3.1. In addition, the coordinate system is selected as that 3R is in the positive direction of the x axis, 12R is in the positive direction of the y axis, and the vertical upward direction is in the positive direction of the z axis.

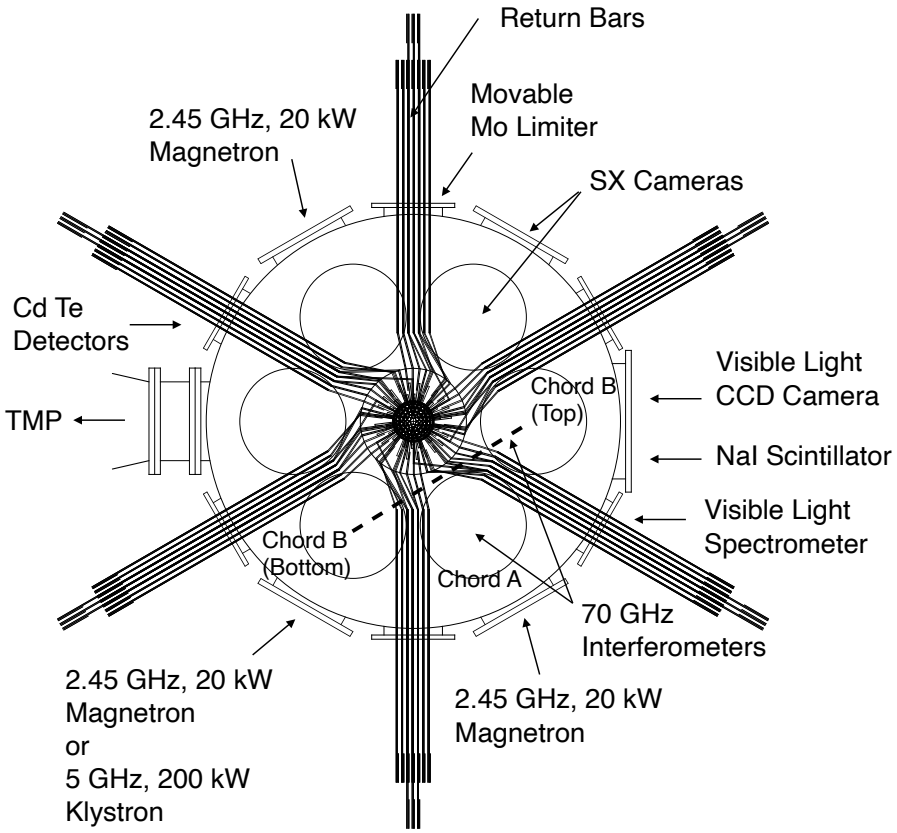

Figure 3.1: Topview of the LATE device.

3.1.2 Gas introduction system

The vacuum vessel is constantly exhausted by the turbo molecular pump (TMP) installed at 12R port, and maintains a vacuum degree of about 5×10^{-5} Pa. In the experiment, hydrogen gas is introduced by the gas puffing method through the piezo valve installed at 12T port. The timing and amount of gas introduction are controlled by the number of cycles, period, and pulse length of the pulse voltage applied to the piezo element.

3.1.3 Toroidal and vertical magnetic field coils

The center post of LATE is a stainless steel cylinder with an outer diameter of 11.4 cm and an inner diameter of 10.8 cm, and 60 copper pipes (outer diameter 10 mm and inner diameter 6 mm) are fixed inside it with epoxy resin. The copper pipe is continuous via a copper return rim (width 100 mm and thickness 3 mm), and the toroidal magnetic field B_{t} is generated by

passing the electric current I_{t} in the same direction. The toroidal magnetic field can be calculated as

$$B_{\mathrm{t}} = 60 \times \frac{\mu_0 I_{\mathrm{t}}}{2\pi R} \tag{3.1}$$

The power supply for generating the toroidal magnetic field can be energized for up to 10 seconds at a maximum rating of 120 V and 1 kA.

The vertical magnetic field is formed by passing currents in the same direction through three pairs of independent annular coils ($B_{\mathrm{v-in}}$, $B_{\mathrm{v-out}}$, $B_{\mathrm{v-R}}$) shown in figure 3.2. The center position and number of turns of each coil are shown in table 3.1.

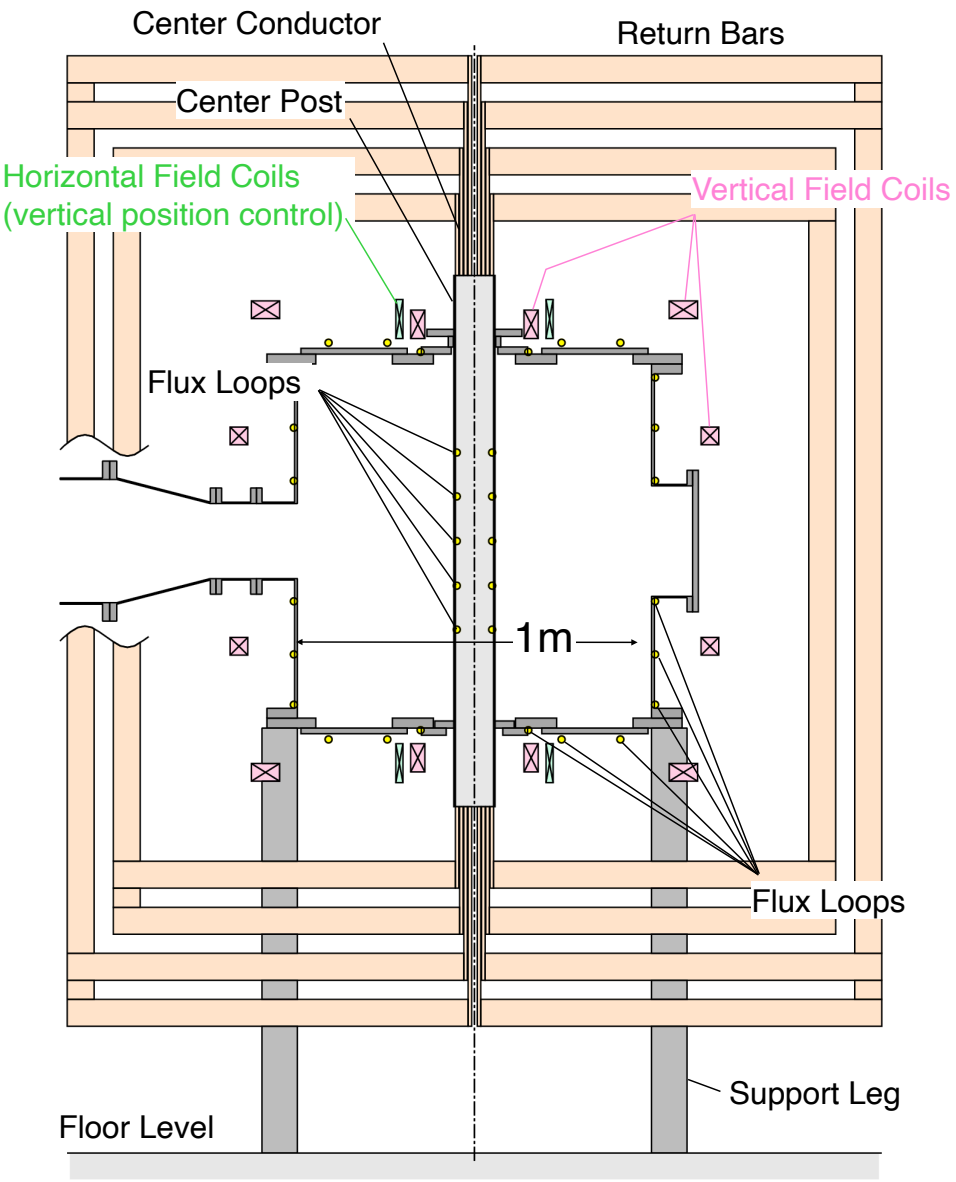

Figure 3.2: Sideview of the LATE device.

Table 3.1: The center position and number of turns of the vertical magnetic field coil.

	R (mm)	Z (mm)	number of turns
$B_{\mathrm{v-in}}$ coil	178	±583	41
$B_{\mathrm{v-out}}$ coil	553	±658	20
$B_{\mathrm{v-R}}$ coil	652	±275	20

Three pairs of coil current values are determined by using the values of the vertical magnetic field strength B_{v}, decay index, and $I_{\mathrm{v-in}}/I_{\mathrm{v-out}}$ ratio as control parameters. The individual coil systems are excited by different constant current sources and preprogrammed using a computer-controlled arbitrary waveform generator.

3.1.4 Microwave injection system

Plasma is generated by electron cyclotron resonance heating using microwaves. The microwave source is a continuous-wave (CW) magnetron with a frequency of 2.45 GHz and a maximum output power of 5 kW. The microwave generated by the magnetron is in the rectangular TE_{01} mode, and then converted to the circular TE_{11} mode by the rectangular-circular mode converter. After passing through the arbitrary polarization tube combined with a Teflon plate, the microwave is injected obliquely with respect to the toroidal magnetic field into the vacuum vessel from 8R port. In present experiments, the injection mode is counterclockwise circularly polarized wave and the injection angle is 75°.

3.2 EBW excitation and detection system

The EBW excitation and detection system consists of four parts: a waveguide launcher with arbitrary polarization, a specially designed five-pin probe antenna, a 2-D mechanical probe driving system, and a homodyne-type mixer circuit. Sideview and topview of the whole system are shown in figure 3.3 and figure 3.4, respectively.

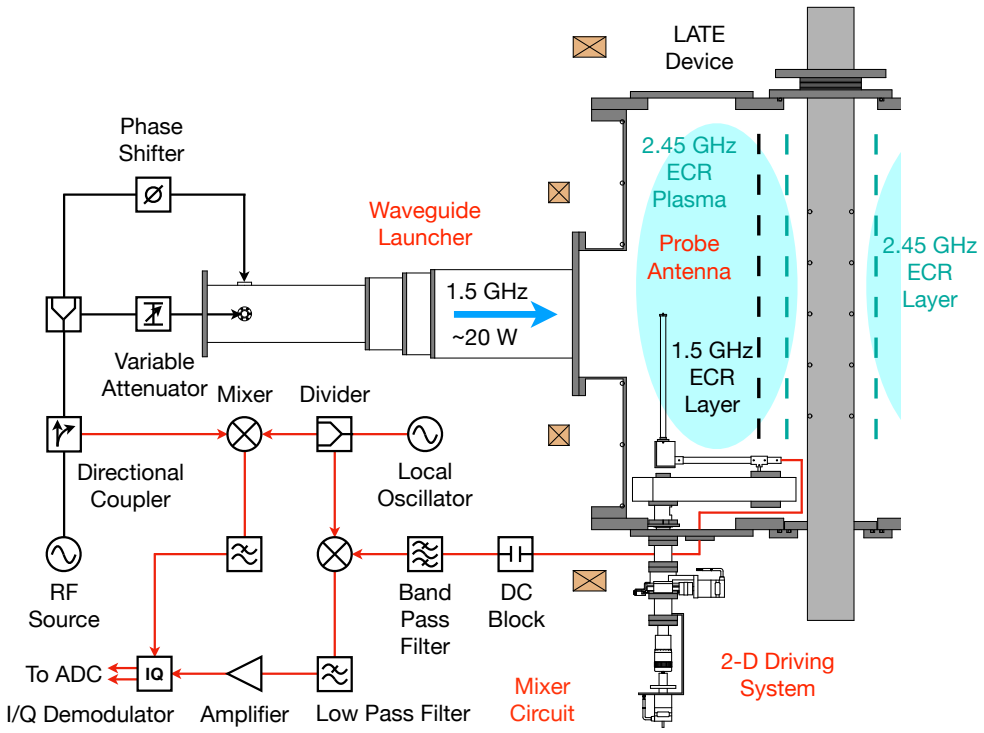

Figure 3.3: Sideview of the EBW excitation and detection system. Both the LATE device, waveguide launcher, 2-D driving system and mixer circuit are shown here.

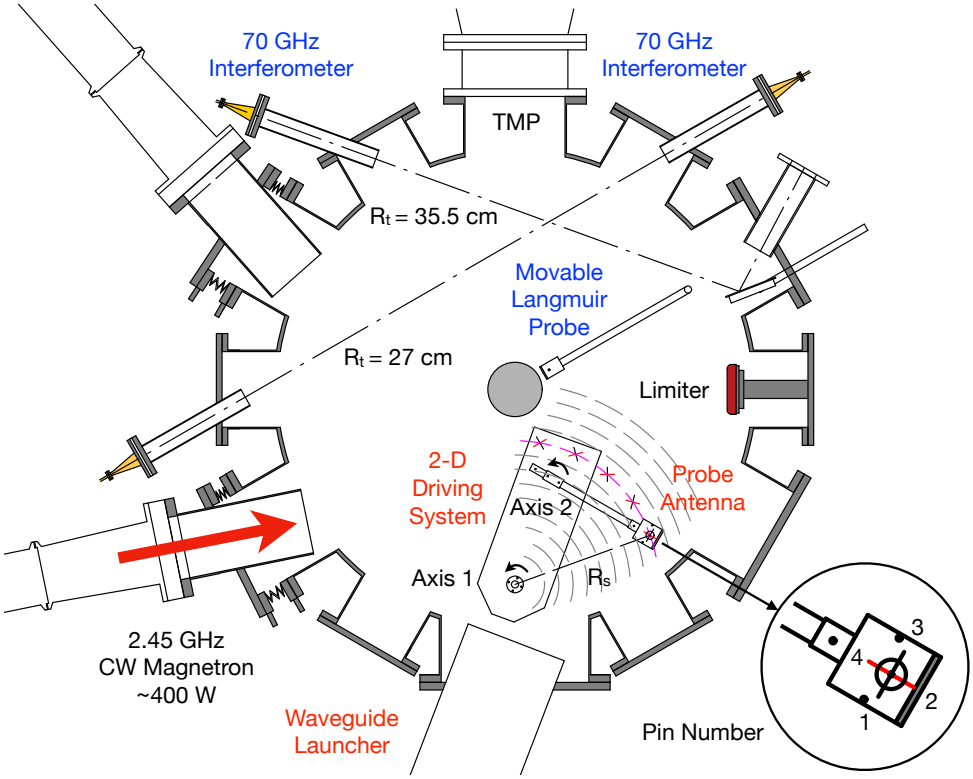

Figure 3.4: Topview of the EBW excitation and detection system. The measurement area of the probe antenna is shown by the dashed curves, while the antenna direction is indicated by a cross. The pin number is marked on the right bottom side. The density and temperature measurement system (70 GHz interferometers and movable Langmuir probe) is also shown here.

The excitation and detection process is as follows: (1) 2.45 GHz heating microwave (∼400 W) is generated by a continuous-wave (CW) magnetron and injected from 8R port in O-mode obliquely to the toroidal magnetic field. Via O-X-B conversion scheme, an overdense ECR plasma can be produced by EBW of 2.45 GHz microwave, which is uniform along the ECR layer and fills the vacuum vessel. (2) 1.5 GHz detecting microwave (∼20 W) is generated by a RF power generator, mode converted to desired polarization in an open circular waveguide launcher, and eventually, injected into the target plasma from 6R port for EBW excitation. (3) The five-pin probe antenna inserted from the lower part of the LATE device is swept by the 2-D mechanical probe driving system, so the wave field pattern inside the plasma is measured. (4) The signal received by the probe antenna is sent to the mixer circuit, and time-independent wave pattern is detected by interferometric method.

3.2.1 Waveguide launcher

In order to excite EBW, the O-X-B method by oblique microwave incidence from the low magnetic field side (outside) is used in this study. 1.5 GHz microwave is generated by an RF power generator, converted to waveguide mode by a waveguide launcher, and eventually, injected into the plasma from 6R port of LATE for EBW excitation.

The launcher is made of SUS304 with an outer diameter of 215 mm, an inner diameter of 208.3 mm and a total length of 995.7 mm. ICF034 conflat flanges are attached to the horizontal (x) side and vertical (y) side of the launcher, which are 103.4 mm from the bottom end, respectively. Two stainless steel rods with a diameter of 7 mm and a length of 44.7 mm are installed inside, to form a coaxial waveguide converter. A schematic diagram of the waveguide launcher is shown in figure 3.5.

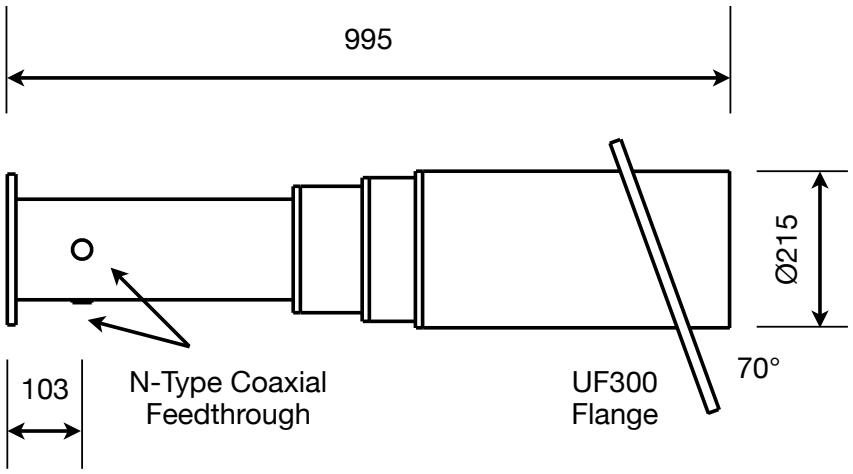

Figure 3.5: A schematic diagram of the waveguide launcher. All dimensions are in units millimeter.

When a high-frequency current flows through the stainless steel rod, the TE_{11} mode, with the electric field oscillating in the same direction as the rod (x, y direction), is generated. The electric field in the x and y directions can be written as

$$\begin{aligned} E_x &= A_x \cos(\phi_x - \omega t) \\ E_y &= A_y \cos(\phi_y - \omega t) \end{aligned} \tag{3.2}$$

By adjusting the relative amplitude A_x/A_y and phase $\phi_y - \phi_x$, arbitrary polarization (linear, circular and elliptical) can be generated. In the experiment, a variable attenuator and a phase shifter are used for such adjustment.

The polarization of the waveguide launcher is tested in the air by using a rotating monopole antenna, which is placed at the center position, about 10 cm in front of the launcher. The test results are shown in figure 3.6.

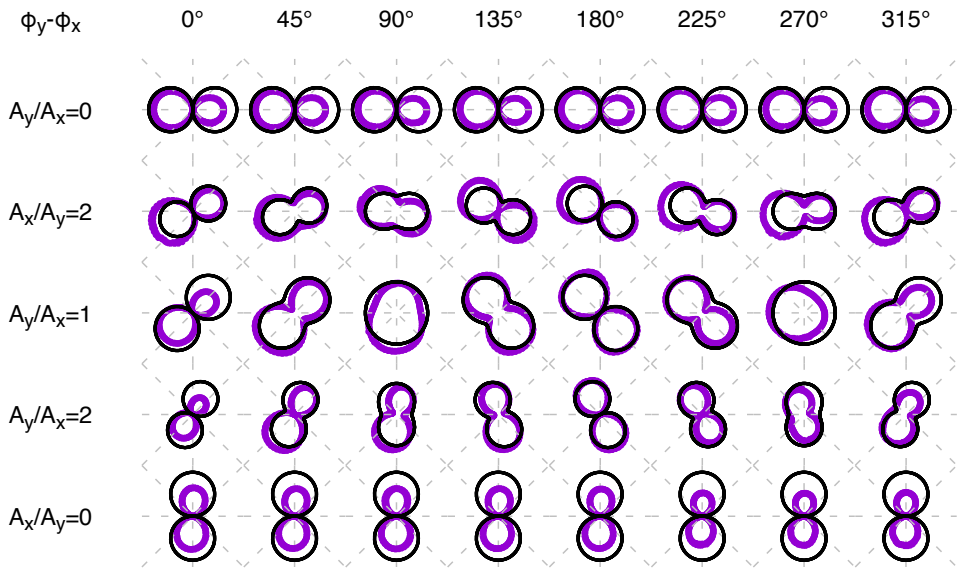

Figure 3.6: Waveguide launcher polarization test results. Measured and theoretical results are shown in purple and black curves, respectively.

The RF power is fixed at 4 W in the test. Measured results are normalized by linear polarization and fixed antenna direction test results. From figure 3.6, it is noted that theoretical and measured results of the polarization agree relatively well, which means the launcher performance is reliable. The differences between them are partly due to incomplete excitation of the waveguide launcher, and partly due to inaccurate placement of the monopole antenna (not exactly at the center position and vertical to the horizontal plane).

The reflectance of the launcher is also investigated by using a network analyzer (Agilent 8719ET), which is shown in figure 3.7. Measurement results show that the reflection rate in the frequency range of 1.45 to 1.55 GHz used in present experiments is -8 dB (16%) or less.

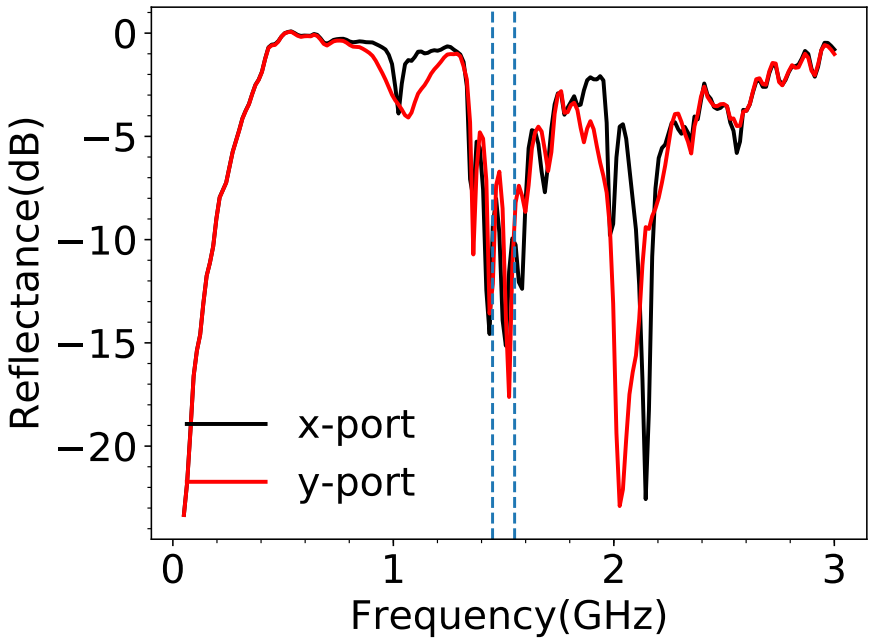

Figure 3.7: The reflectance of the waveguide launcher.

3.2.2 Five-pin probe antenna

Monopole and dipole antennas used in previous experiments [12, 21, 22] are pretty suitable for detecting long-wavelength electromagnetic modes, but not suitable for detecting short-wavelength electrostatic modes. In the case of LATE experiment, the electron temperature, toroidal magnetic field, and cutoff density for 1.5 GHz microwave are about 5 eV, 300 G, and 2.8×10^{16} m^{-3}, then the wavelength of EBW is about 3.6 mm. Therefore, a monopole antenna with the antenna chip oriented in the direction of the electric field cannot obtain sufficient spatial resolution for this short-wavelength wave, as the chip length is comparable to the wavelength. To detect EBWs directly, a specially designed five-pin probe antenna is developed.

A schematic diagram of the five-pin probe antenna is shown in figure 3.8. The antenna consists of five mineral-insulated (MI) cables, two ceramic tubes, one stainless steel pipe and one boron nitride (BN) cap.

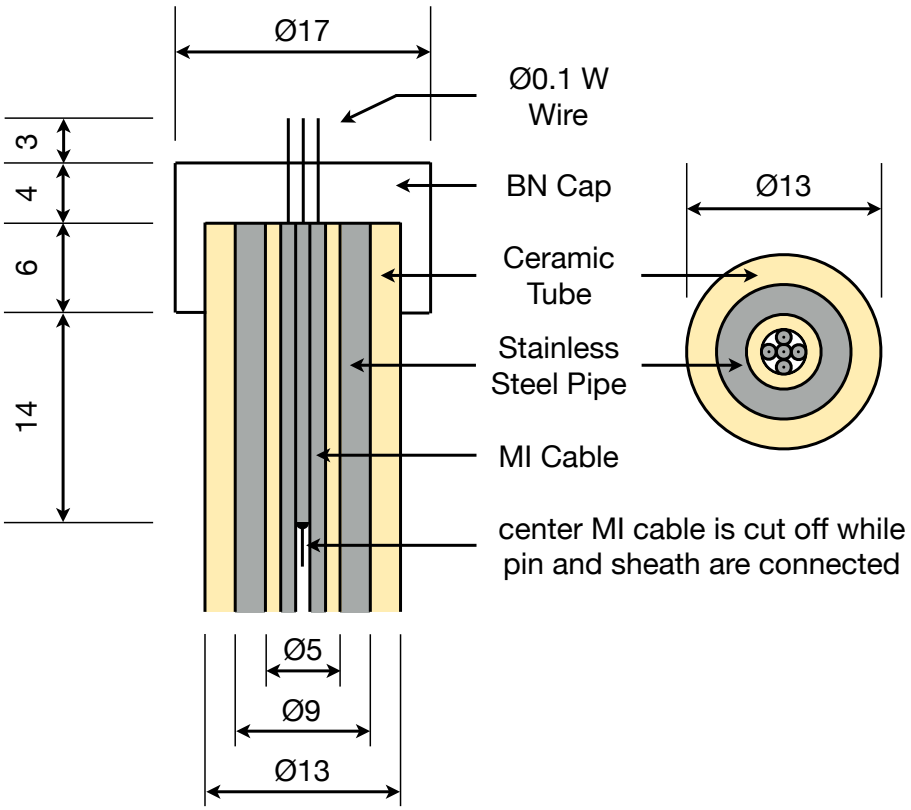

Figure 3.8: A schematic diagram of the five-pin probe antenna. All dimensions are in units millimeter.

For the MI cable, the core wire is made of tungsten with a diameter of 0.1 mm, the sheath is made of stainless steel with an outer diameter of 1.14 mm, and the dielectric insulator between them is silicon dioxide (SiO_2). The characteristic impedance of the MI cable is 65 Ω, which is expected to be well matched to the mixer circuit's 50 Ω impedance. The center MI cable (center pin) is cut off at about 2 cm, and the core wire and sheath are electrically connected by scraping out the insulator from the end and crushing the sheath. By inserting it into the gaps between the four corner MI cables (four corner pins), the core wire of the center MI cable and the sheaths of the four corner MI cables are equipotential.

Five pins are guided vertically at the end, fixed and protected by a BN cap (with five holes). The exposed core wire length is 3 mm, and the distance between the center pin and each corner pin is 1 mm.

Five MI cables pass through a ceramic tube for insulation, and outside there is a stainless steel pipe connected to the vacuum vessel, which acts as an electromagnetic shield. And the outermost part is a ceramic tube for

protection from the plasma.

To prevent the pins from shaking during antenna movement, the stainless steel pipe that shields the MI cable is fixed to a stainless steel box below by using a small flange. The MI cables switch to the coaxial cables inside the box, through SMA connectors, which are fixed to a PEEK plate so that the sheath does not touch the box. The coaxial cable is Fujikura RG188A/U type with a PTFE protective film for heat resistance. The cables go through a flexible stainless tube and exit to the atmosphere from the current inlet terminals at 6B port.

The basic idea of the five-pin probe antenna comes from a two-pin antenna method, in which two pins are perpendicular to the electric field and the potential difference between the pins is measured [12]. In principle, a current that is proportional to the potential difference between the center pin and the corner pin is induced in the corner MI cable, therefore, four corner pins can measure electric fields in two orthogonal directions (from the corner pin to the center pin). Since the distance between the center pin and each corner pin is only 1 mm, the antenna is highly sensitive to mm-level short-wavelength modes.

3.2.3 2-D mechanical probe driving system

Previous experiments of EBW measurement [12, 21, 22] were all limited in one dimension. In the O-X-B method, microwave is injected obliquely with respect to the magnetic field, so it is necessary to measure wave electric field two-dimensionally. In order to perform 2-D measurement of the wave pattern on the mid-plane, a 2-D mechanical probe driving system is developed and installed at 6B port of LATE device.

The mechanical system has two rotation axes, which are driven by two stepping motors, respectively. Axis 1 is a hollow-type rotation introduction machine KRP-70 (Kitano Seiki), and axis 2 is a bellows-type rotation introduction machine IRC-70 (Irie Koken). Axis 1 rotates the pulley box itself, while axis 2 rotates the stainless steel pipe and associated antenna box through the belt and pulley in the pulley box. A schematic diagram of the 2-D mechanical probe driving system is shown in figure 3.9.

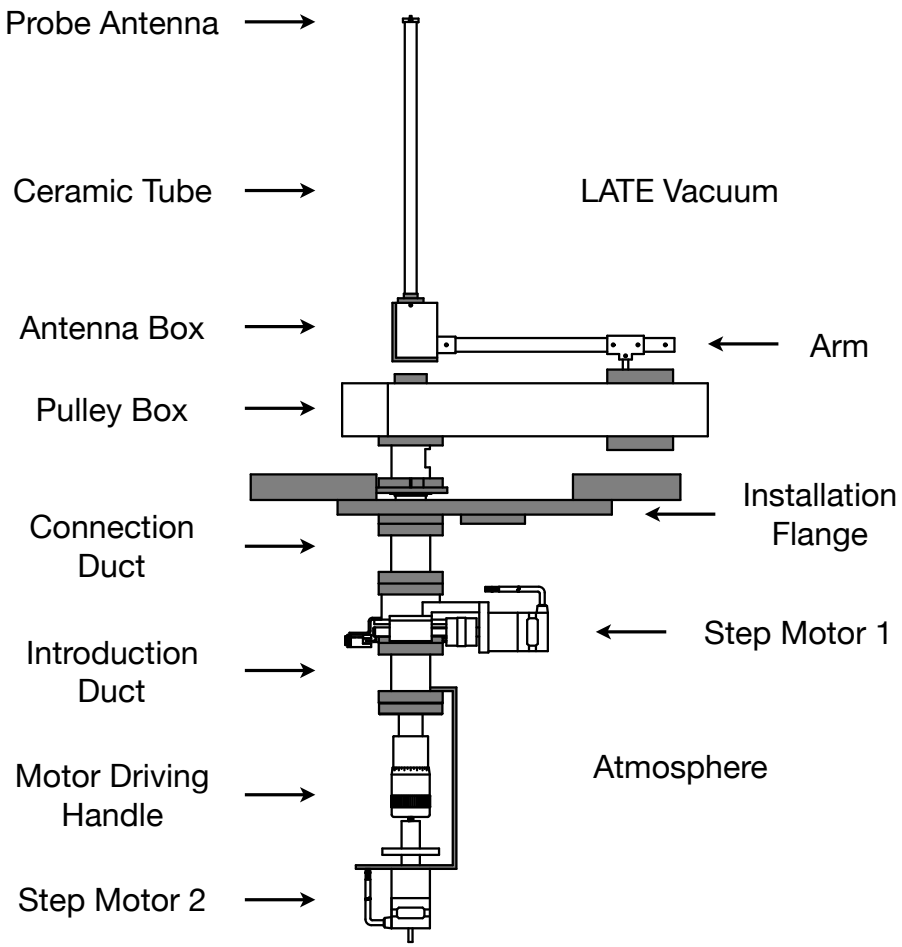

Figure 3.9: A schematic diagram of the 2-D mechanical probe driving system.

In order to know the position of the probe antenna, the gear of each axis is attached to a variable resistor, whose resistance depends on the rotation angle. With DC voltage applied to the variable resistor, the rotation angle of each axis and the position of the probe antenna can be easily determined from the voltage change.

It should be mentioned that backlash for axis 1 can be neglected due to tight connection between the pulley box and motor 1, and backlash for axis 2 cannot be neglected as the arm is driven through multiple transmissions. However, such backlash effect can be compensated if extra steps are added when motor reverses direction, and then the arm is rotated back to the zero position. The variable resistor for axis 1 is next to motor 1, while the variable resistor for axis 2 is next to the arm (inside the pulley box, in the vacuum), so both outputs are considered to be accurate.

In the experiment, axis 2 is fixed at a certain value first, while axis 1 is rotated to sweep the antenna during one shot. The sweeping trajectory is shown by a dashed curve in figure 3.4. Then axis 2 is rotated to change the sweeping radius R_s (the distance between the probe antenna and axis 1 as shown in figure 3.4), and axis 1 is rotated again during next shot. In present experiments, the sweeping radius is in the range of $R_s = 70$ to 440 mm, and the interval between the sweeps is 10 mm, so there are 38 sweeps in total for one complete 2-D measurement. The measurement area is approximately 25 $\times$ 30 cm as shown by the dashed curves in figure 3.4.

It should be noted that the cross on the trajectory in figure 3.4 indicates the relative direction of the five-pin probe antenna, and the direction changes as the antenna moves. This direction is important as it determines the detecting direction of the antenna, and it can be calculated from the rotation angle of axis 1 and 2.

The spacial resolution of the antenna position is determined from the angular speed of axis 1, the sweeping radius R_s and the sampling rate of the analog-to-digital (A/D) converter. In present experiments, the angular speed of axis 1 is 27°/s and the sampling rate is 100 kS/s, so the spatial resolution is 0.0003 to 0.002 mm in the measurement area, which is much smaller than the EBW wavelength.

3.2.4 Mixer circuit

Homodyne detection is a useful method of extracting information as phase and amplitude of an oscillating signal, by comparing that signal with a standard oscillation. For direct measurement experiments, a homodyne-type mixer circuit is used to obtain phase and amplitude of the wave pattern. A schematic diagram of the mixer circuit is shown in figure 3.10.

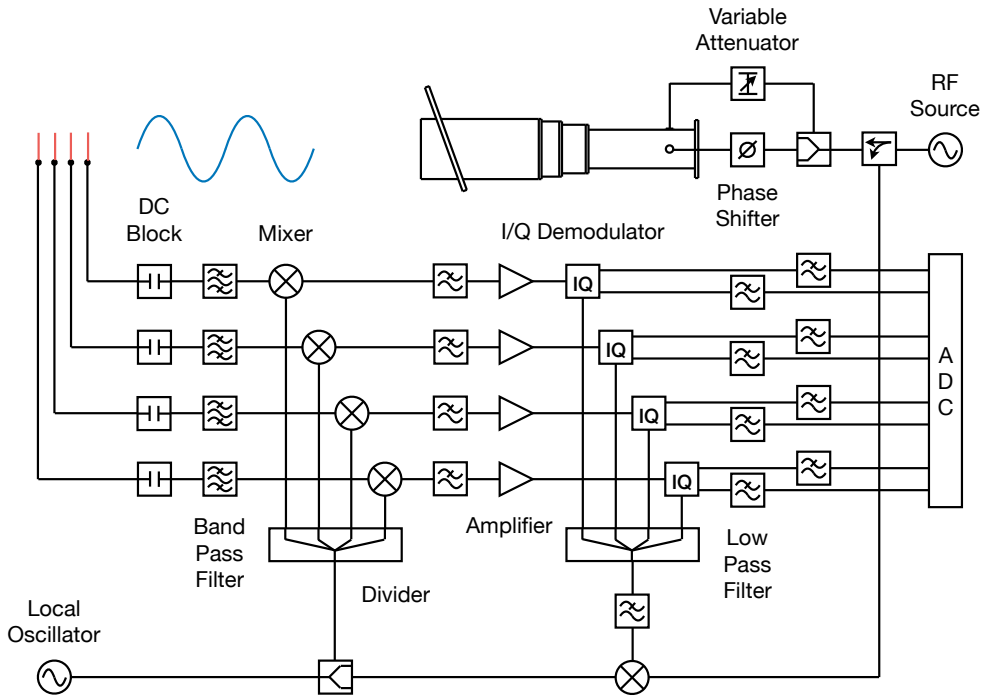

Figure 3.10: A schematic diagram of the mixer circuit.

1.5 GHz microwave is generated from the RF oscillator and divided into two parts by the directional coupler, which can be written as

$$V_{\mathrm{RF}} = A_{\mathrm{RF}} \cos(\omega t + \phi_{\mathrm{RF}}) \tag{3.3}$$

The output part goes to the phase shifter and variable attenuator, and eventually, to the waveguide launcher for EBW excitation. The coupling part goes to the circuit as a reference 1.5 GHz RF signal.

Detected wave signal from the probe antenna goes to the DC block and band pass filter first, to cut out the large DC voltage from the plasma and keep only 1.5 GHz signal which is of interest. Then this signal,

$$V = A \cos(\omega t + \phi) \tag{3.4}$$

is mixed with a reference 1.57 GHz LO signal generated from the local oscillator,

$$V_{\mathrm{LO}} = A_{\mathrm{LO}} \cos[(\omega + \Delta\omega)t + \phi_{\mathrm{LO}}] \tag{3.5}$$

The mixing signal goes to the low pass filter and amplifier, to keep only 70 MHz signal which contains wave signal information and increase the signal to noise (S/N) ratio, which can be written as

$$V_{70} = A A_{\mathrm{LO}} \cos(\Delta\omega t + \phi_{\mathrm{LO}} - \phi) \tag{3.6}$$

Reference 1.5 GHz RF signal and 1.57 GHz LO signal are mixed and low pass filtered so that a reference 70 MHz LO signal is generated as

$$V_{70-\mathrm{Ref}} = A_{\mathrm{RF}} A_{\mathrm{LO}} \cos(\Delta\omega t + \phi_{\mathrm{LO}} - \phi_{\mathrm{RF}}) \tag{3.7}$$

These two 70 MHz signals are imported into the in-phase/quadrature-phase (I/Q) demodulator, so time-independent sine and cosine signals are exported, as

$$\begin{aligned} I &= A\cos\phi \\ Q &= A\sin\phi \end{aligned} \tag{3.8}$$

Here constant factors for amplitude and constant shifts for phase are both omitted. Therefore, phase and amplitude information of the wave pattern can be extracted, as

$$\begin{aligned} \phi &= \tan^{-1}(Q/I) \\ A &= \sqrt{Q^2 + I^2} \end{aligned} \tag{3.9}$$

There are four pins in total, and each pin measures phase and amplitude for certain direction and trajectory as shown in figure 3.9. Eight-channel I/Q outputs go to the analog-to-digital (A/D) converter (NI9215) with a sampling rate of 100 kS/s. A schematic diagram of the signal processing for one channel is shown in figure 3.11.

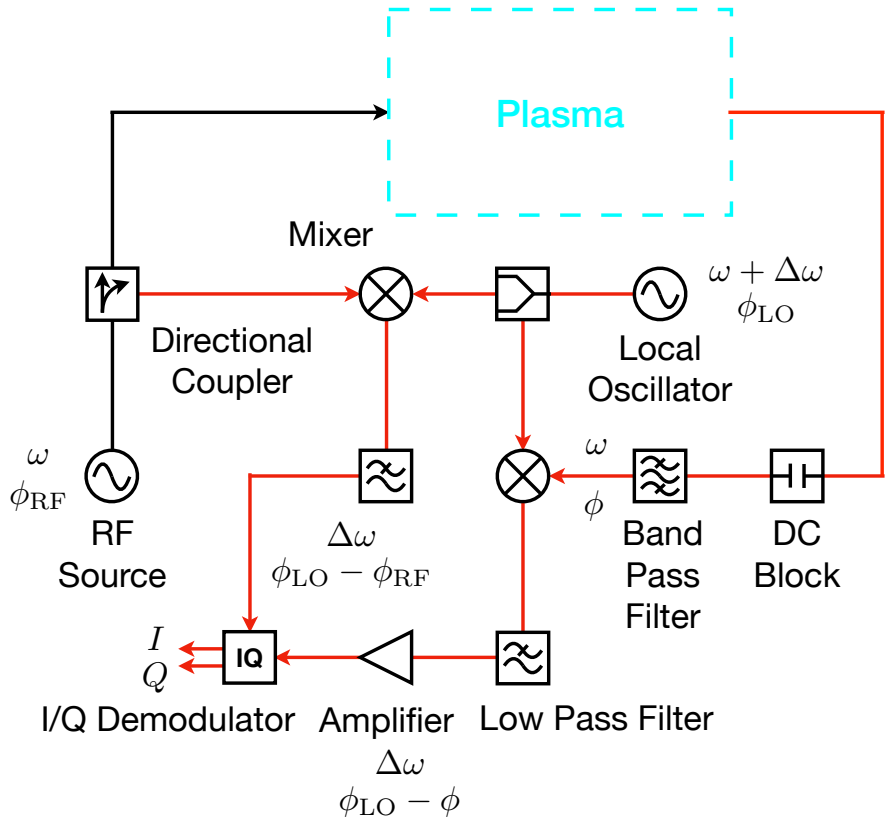

Figure 3.11: A schematic diagram of the the signal processing for one channel.

Semi-rigid cables are used for high-frequency signal transmission to suppress losses. The entire circuit is placed inside a shielded box covered with copper mesh to further reduce electromagnetic noises.

The power loss of the band pass filter, mixer, low pass filter, I/Q demodulator and cables is about 15 dB, the power gain of the amplifier is 25.6 dB, so the total power gain of the circuit is about 10.6 dB. For output amplitude level of about 10 mV, the sensitivity of the circuit is about 3 mV.

To verify the reliability of the mixer circuit, 1.5 GHz microwave is connected with a phase shifter and divided into four parts, which are injected to four channels of the circuit. By adjusting the phase shifter from 0 to 360 degree, variations of eight-channel I/Q outputs are recorded. Phase of the wave signal can be calculated from output I/Q signals as $\phi = \tan^{-1}(Q/I)$. A schematic diagram of the circuit test is shown in figure 3.12.

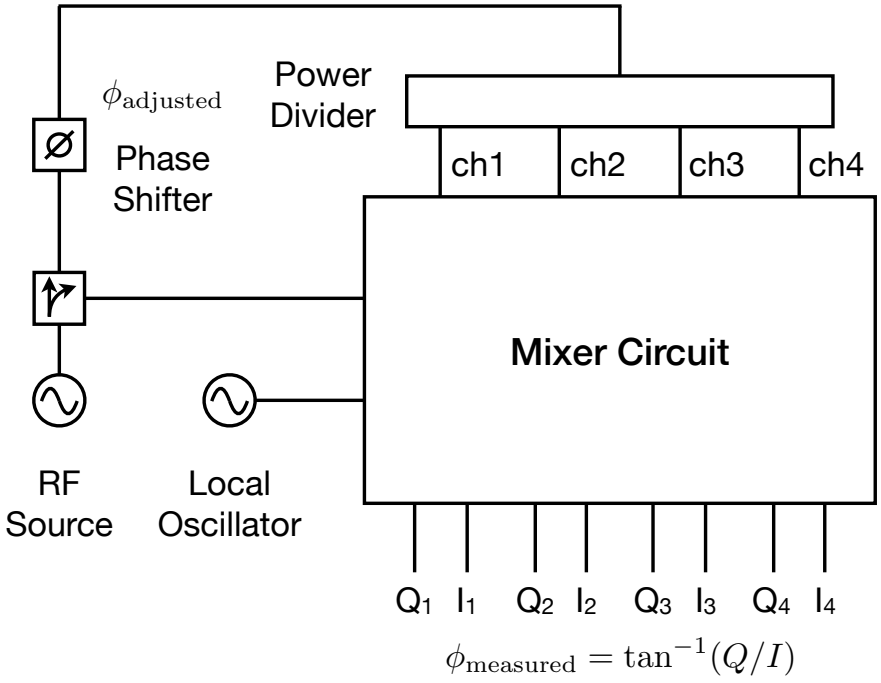

Figure 3.12: A schematic diagram of the circuit test.

The relationship between measured phase calculated form output I/Q signals and adjusted phase from the phase shifter is shown in figure 3.13.

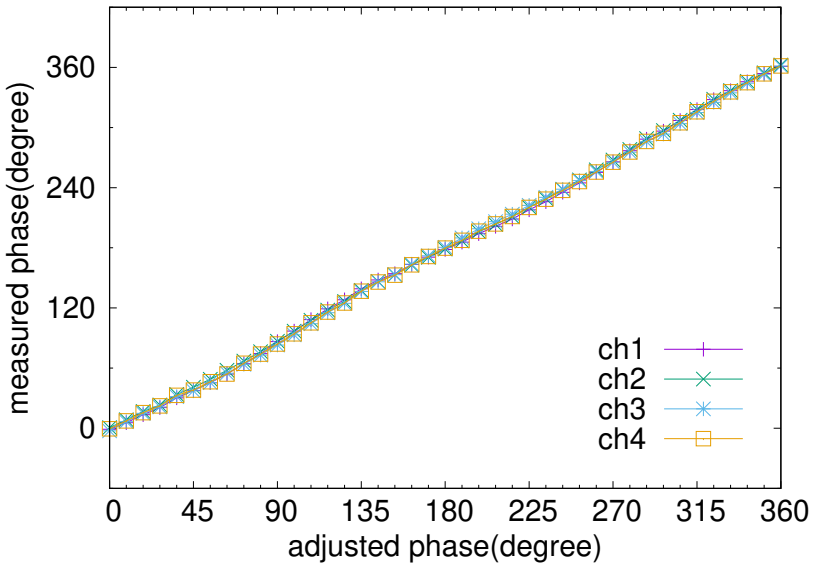

Figure 3.13: Mixer circuit test results.

From figure 3.13, it is noted that there is a very good linearity between the measured phase calculated form output I/Q signals and adjusted phase from the phase shifter, and there is also a good identicalness between four channels.

3.3 Density and temperature measurement system

The density and temperature measurement system consists of one movable Langmuir probe and two 70 GHz microwave interferometers, which is shown in figure 3.4.

The movable Langmuir probe is installed at 2T port and used to measure the electron density and temperature profiles. The probe is controlled by two stepping motors, which enable it to rotate around and slid along its vertical axis. Therefore, the probe tip covers the whole range form $R = 10$ to 47.5 cm and also from $Z = -24$ to $+24$ cm. But in present experiments, the probe tip is fixed on the mid-plane and only one motor is used, since only profiles on the mid-plane is of our interest.

The probe tip is made of tungsten with a diameter of 0.5 mm and a length of 5 mm. Other parts of the probe are nested with an SSA-S protective tube with an inner diameter of 0.8 mm and an outer diameter of 1.2 mm, a SUS304 pipe with an inner diameter of 1.45 mm and an outer diameter of 1.81 mm, and an SSA-S protective tube with an inner diameter of 2.0 mm and an outer diameter of 3.0 mm. It is covered so that it does not contact with the plasma. In addition, the base of the probe tip and the base of the outer ceramic tube are fixed with Aron Ceramic, a heat-resistant inorganic adhesive. The tungsten wire is inserted into a copper pipe inside the box and crimped to the core wire of the coaxial cable, and the coaxial cable is connected to the circuit on the atmosphere side via the current introduction terminal. For this coaxial cable, RG188A/U made by Fujikura, which has a PTFE protective film, is used in consideration of heat resistance. The pickup resistance can be switched between 10, 51, 100, 510, 1000 and 5000 Ω, and is selected according to the magnitude of the probe current.

At tangency radius $R_\mathrm{t} = 35.5$ cm (system A) and 27 cm (system C) on the mid-plane, two 70 GHz microwaves are injected into the plasma and the line-integrated electron densities along two chords are measured. The line-of-sight lengths of system A and system C are about 83 cm and 70 cm, respectively.

In the experiment, two methods are used to measure the electron density and temperature profiles: the ion saturation current profile measurement and the $I - V$ characteristics measurement. In the first method, the probe is rotated during the discharge with a constant negative voltage applied to it, and the ion saturation current profile is measured in one shot. Under the assumption that the electron density is proportional to the ion saturation current, $n_\mathrm{e} = \text{factor} \times I_\mathrm{is}$, the multiplication factor can be obtained from the interferometer data as follows,

$$nl_{R_\mathrm{t}} = 2 \times \int_0^{\sqrt{R_0^2 - R_\mathrm{t}^2}} \text{factor} \times f\left(\sqrt{x^2 + R_\mathrm{t}^2}\right) \mathrm{d}x \tag{3.10}$$

where nl_{R_t} is the line-integrated electron density along chord at tangency radius R_t, R_0 is the radius of LATE vacuum vessel, $f(R)$ is the fitting function of the ion saturation current profile over large radius. In the second method, the probe is fixed during the discharge with a sawtooth voltage applied to it, and the electron density and temperature are obtained from the $I - V$ characteristics and effective area of the probe. The density and temperature profiles can be measured in multiple shots by changing the position of the probe.

Chapter 4

Experimental results

4.1 O-mode injection

For the O-X-B experiments, the RF power generator is connected to the horizontal side of the waveguide launcher and 1.5 GHz microwave is injected as O-mode. Both the electron density and temperature profiles, 1-D and 2-D wave pattern of phase and amplitude are measured and analyzed.

4.1.1 Target plasma and discharge waveform

A typical discharge waveform is shown in figure 4.1. Toroidal magnetic field coil current is set to 900 A, so the second harmonic ECR layer for 2.45 GHz microwave is at $R_{2\mathrm{nd}-\mathrm{ECR}} = 246.8$ mm. Vertical magnetic field B_v and its decay index $-(R/B_\mathrm{v}) \cdot (\partial B_\mathrm{v}/\partial R)$ are set to 10 G and 0.15, respectively, for the production of trapped high energy electrons and suppression of density fluctuations. Puffs of hydrogen gas are introduced into the vacuum vessel at 0.1 s, for a filling gas pressure of 2.0×10^{-2} Pa. 2.45 GHz microwave is injected at a constant level of 400 W between 0.3 to 4.3 s. After microwave injection, gas pressure quickly decreases to the level of 0.6×10^{-2} Pa, while plasma current ramps up to 50 A, and an overdense plasma (for 1.5 GHz microwave) is generated. The target ECR plasma is similar to the one produced in previous low power experiments [27]. For EBW excitation, 1.5 GHz microwave is injected at a power level of 20 W between 0.75 to 4.0 s, when the plasma is at steady state. The probe antenna starts sweeping from 0.8 s, at a constant angular speed of 27°/s with respect to axis 1 (after about 0.2 s acceleration), and stops before 4.0 s according to the sweeping trajectory length, for the measurement of the wave pattern.

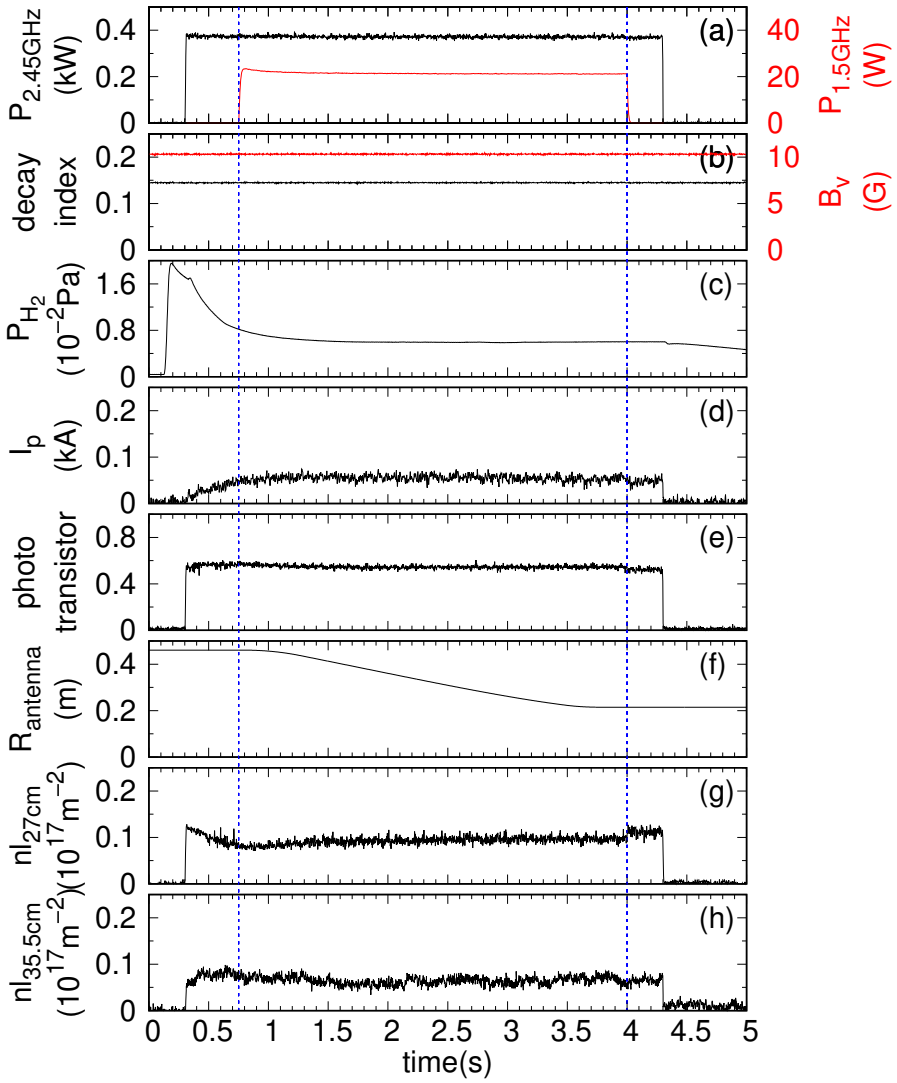

Figure 4.1: A typical discharge waveform for O-mode injection: (a) 2.45 GHz heating microwave power and 1.5 GHz detecting microwave power, (b) vertical magnetic field B_v and its decay index $-(R/B_\mathrm{v}) \cdot (\partial B_\mathrm{v}/\partial R)$, (c) gas pressure, (d) plasma current, (e) plasma light, (f) radial position of the probe antenna, (g) and (h) line-integrated electron densities along 27 and 35.5 cm chord. The steady state period (0.75 to 4.0 s) is marked by vertical dashed lines.

Typical I/Q signals during one sweep $R_\mathrm{s} = 220$ mm are shown in figure

4.2. Between 0 to 0.75 s and 4.0 to 5.0 s, I/Q signals are at a constant level of zero with only a background noise of about 4 mV. Since 1.5 GHz microwave is not injected in these periods, such results indicate that unwanted signals (not 1.5 GHz) are almost completely filtered by the mixer circuit. Between 0.75 to 4.0 s, I/Q signals reach a level of about 80 mV and show clear variations over time, indicating a high S/N ratio of about 20.

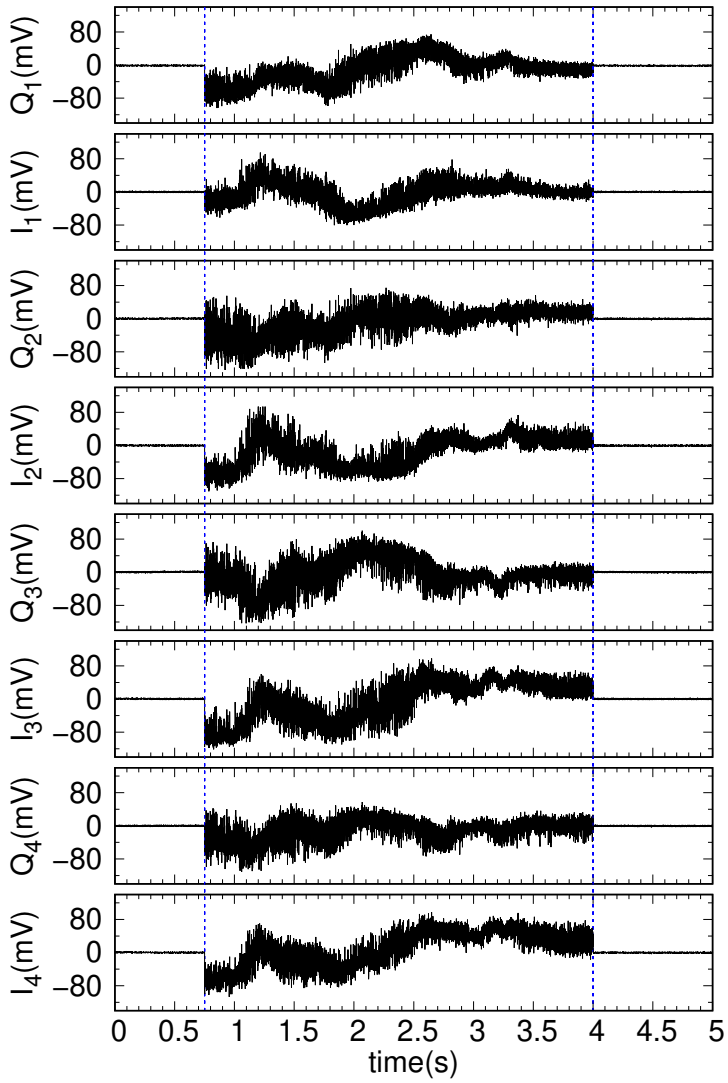

Figure 4.2: Typical I/Q signals for O-mode injection during one sweep R_s = 220 mm. The suffix numbers indicate the antenna pin numbers, and there are eight channels for four pins.

The electron density and temperature profiles obtained from two methods are shown in figure 4.3. It should be mentioned that in the experiment, the movable Langmuir probe has a much larger disturbance to the plasma than the EBW antenna in the range of $R \leq 220$ mm, as the plasma usually breaks down and the discharge is terminated once the probe reaches in the core

region. Therefore, the measurable range is limited to $R = 230$ to 475 mm in present experiments. For the electron density profile, it is noted that the two methods are almost the same in the range of $R = 270$ to 475 mm, so the ion saturation current measurement is considered effective and efficient, which will be used in later analysis. The multiplication factor is calculated to be 10.7×10^{16} m^{-3}/mA. It is also noted that the plasma is highly overdense for 1.5 GHz microwave, as the peak density (1.8×10^{17} m^{-3}) is about 6 times the cutoff density (2.8×10^{16} m^{-3}), and the peak position approximately coincides with the second harmonic ECR layer for 2.45 GHz microwave. Since the UHR, PC, and ECR (for 1.5 GHz microwave) layers are well separated at $R_{\mathrm{UHR}} = 362.5$ mm, $R_{\mathrm{PC}} = 337.6$ mm, $R_{\mathrm{ECR}} = 201.5$ mm, respectively, the whole process of excitation, propagation and damping of EBW can be studied in detail. For the electron temperature profile, it is noted that the electron temperature is at a pretty low level of about 3.6 eV in the range of $R = 330$ to 475 mm, and it gradually increases to about 6.8 eV at $R = 270$ mm. Such low electron temperature will protect the probe antenna from being damaged by the plasma, but it will also decrease the EBW wavelength and increase the EBW collisional damping rate.

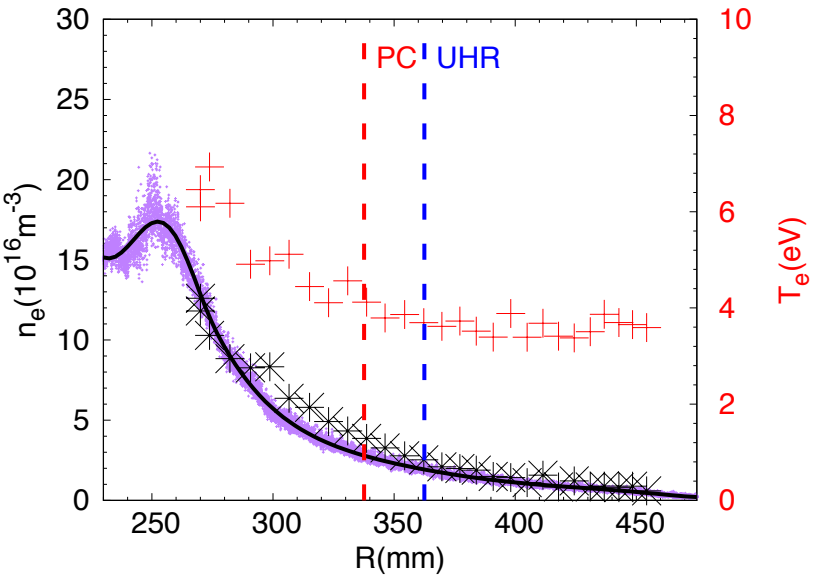

Figure 4.3: The electron density and temperature profiles for O-mode injection. The ion saturation current measurement results and the fitting curve (after 10.7×10^{16} m^{-3}/mA factor multiplication) are plotted by purple points and a black line, respectively. The electron density and temperature obtained from the $I-V$ characteristics are plotted by black stars and red crosses, respectively. The UHR and PC layers are marked by vertical dashed lines.

4.1.2 2-D wave pattern

Two-dimensional plots of phase and amplitude pattern measured by four pins are shown in figure 4.4 and figure 4.5. For each plot, the sweeping radius is in the range of $R_s = 70$ to 440 mm with 10 mm interval, so there are 38 sweeps in total. The measurement region is almost the same as in figure 3.4. It should be mentioned that the reliability of 2-D measurement depends on the reproducibility of both the plasma and wave pattern. To verify these, the electron density profile is measured multiple times after different sweeps and compared, while I/Q signals are also measured multiple times for the same sweep and compared. The comparison results indicate that both the plasma and wave pattern can be well reproduced and 2-D measurement is reliable.

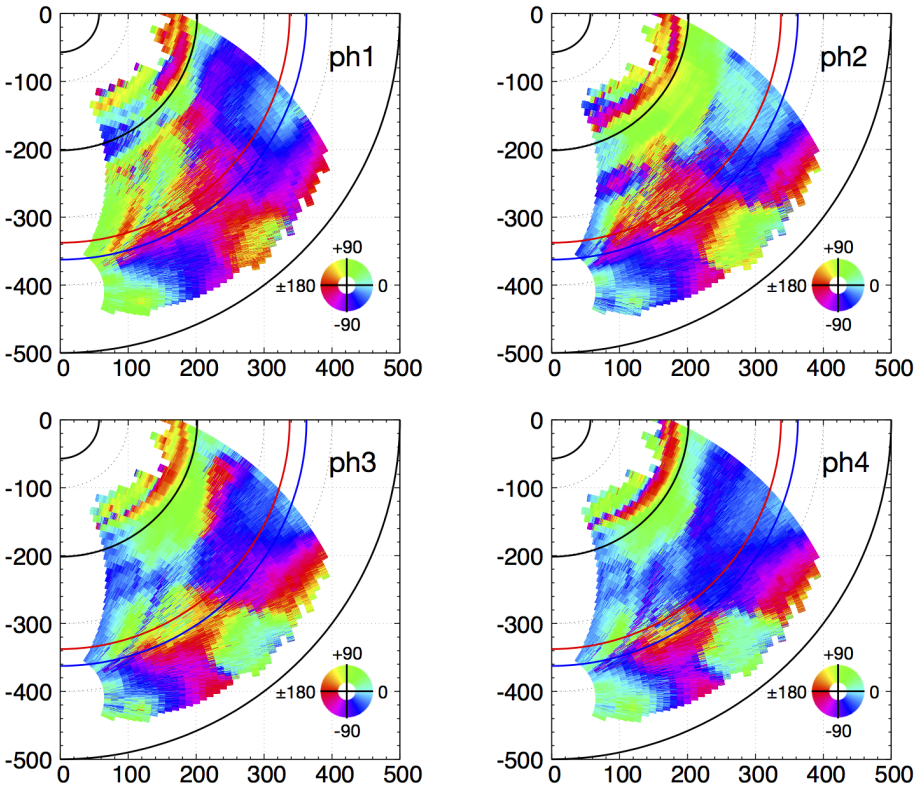

Figure 4.4: Two-dimensional plots of phase pattern measured by four pins for O-mode injection. Phase calculated from I/Q signals of pin 1 is shown by ph1, and so on. The LATE wall, UHR, PC, ECR layers and center post are marked by five solid curves from outside to inside, respectively. The phase and coordinate unit are degree and millimeter, respectively. The short-wavelength region is encircled and expanded for ph2 and ph4.

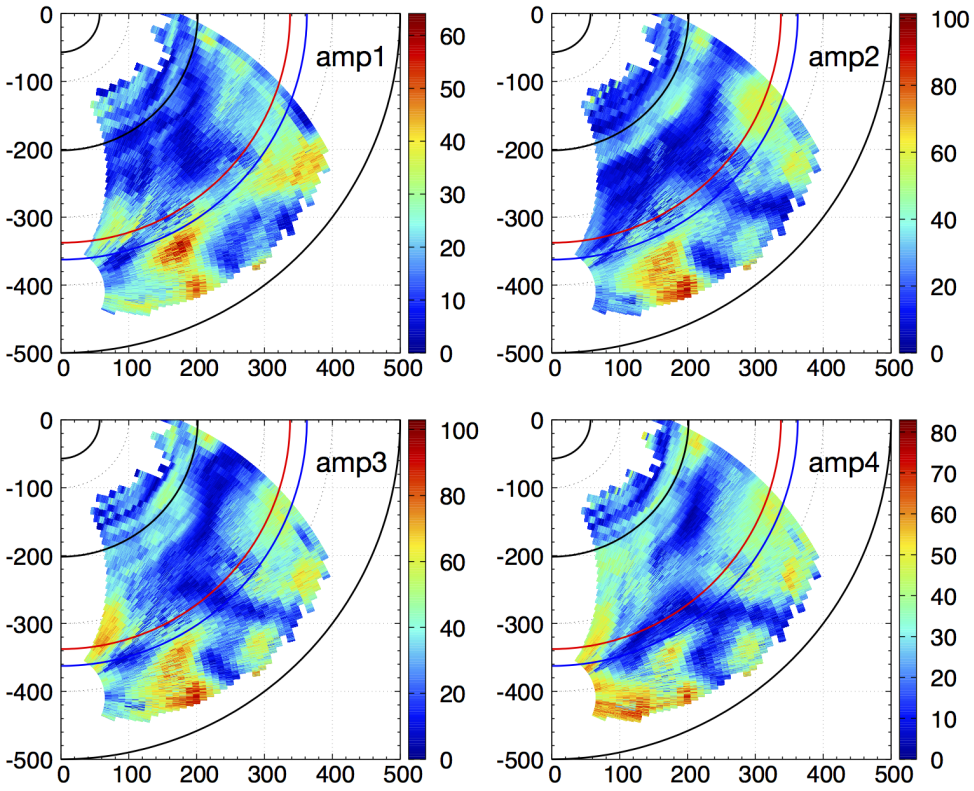

Figure 4.5: Two-dimensional plots of amplitude pattern measured by four pins for O-mode injection. Amplitude calculated from I/Q signals of pin 1 is shown by amp1, and so on. The LATE wall, UHR, PC, ECR layers and center post are marked by five solid curves from outside to inside, respectively. The amplitude and coordinate unit are millivolt and millimeter, respectively.

From figure 4.4 and figure 4.5, several results can be noted.

First, the overall wave pattern of phase and amplitude is pretty similar for both pins, yet some small differences can still be viewed. To understand this phenomenon, 2-D wave pattern in vacuum (without plasma, with only 1.5 GHz microwave injected as O-mode) is also measured, which shows that highly similar wave pattern is detected by four pins once again. As mentioned before, the potential difference between the center pin and the corner pin can induce current in the corner MI cable, while the measurement results in vacuum suggest that current can also be induced by the electric field in the vertical direction (parallel to the corner pin). Since four pins are all guided vertically, the overall wave pattern will be similar in regions where

the vertical electric field is dominant for detection. However, in regions where the short-wavelength electrostatic waves become dominant, differences of the wave pattern for different pins will emerge.

Second, a short-wavelength wave pattern is detected by pin 4 in a small region near the UHR layer. From phase 4 in figure 4.4, a rapid phase change pattern appears in a small region of about 30×35 mm near the UHR layer (x = 155 to 185 mm, $y = -300$ to -335 mm). An expanded plot of this region is shown in figure 4.6. In the experiment, the probe antenna is fixed on the antenna box and the detection direction of pins cannot be adjusted. But with appropriate initial setting of the antenna, the detection direction and moving direction of pin 2 and 4 are both almost radial in this region as shown in figure 3.4. Therefore, such short-wavelength wave pattern is electrostatic and mainly radially propagating, as the wave electric field is parallel to the wave vector (both almost radial). It is noted that there is similar pattern in phase 1, phase 2, and phase 3, and there is no such pattern in vacuum. It should be mentioned that both EBW and X-mode are present near the UHR layer, and the wave may have a small but nonzero parallel wave number as the original O-mode is injected obliquely, so there should be signals not only in the radial direction. Besides, the sensitivity of each pin and pin arrangement may also affect the measured phase pattern for short-wavelength electrostatic waves. In present experiments, clear and most convincing 1-D short-wavelength wave pattern (section 4.1.3) is only detected by pin 4, which is used for further analysis.

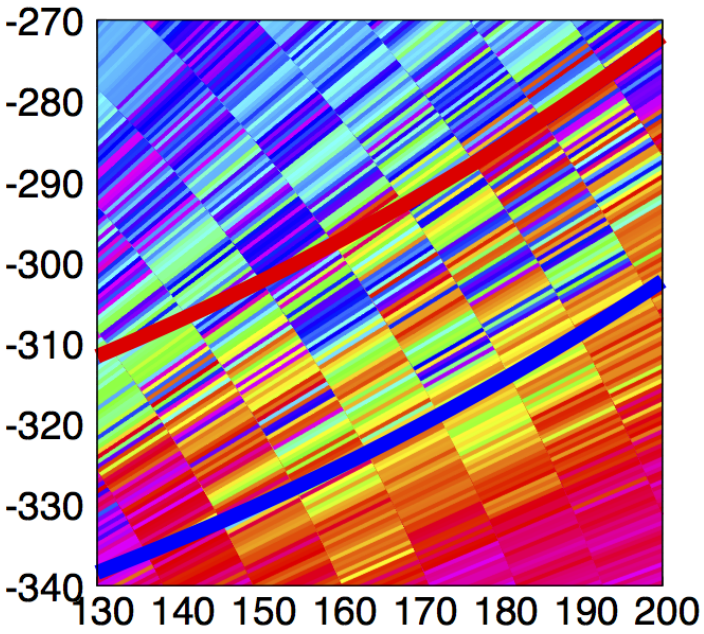

Figure 4.6: An expanded plot of the short-wavelength region for pin 4 in figure 4.4.

4.1.3 1-D variation of phase and amplitude

Since the wavelength of EBW is only a few millimeters in present experiments, such short-wavelength wave pattern cannot be precisely verified from the wide 2-D plot as shown above. Therefore, for sweeps which pass through the short-wavelength region in phase 4 of figure 4.4, 1-D variation of phase and amplitude are plotted with the horizontal axis as the large radius, which is shown in figure 4.7. The sweeping radius R_s of each sweep is also marked.

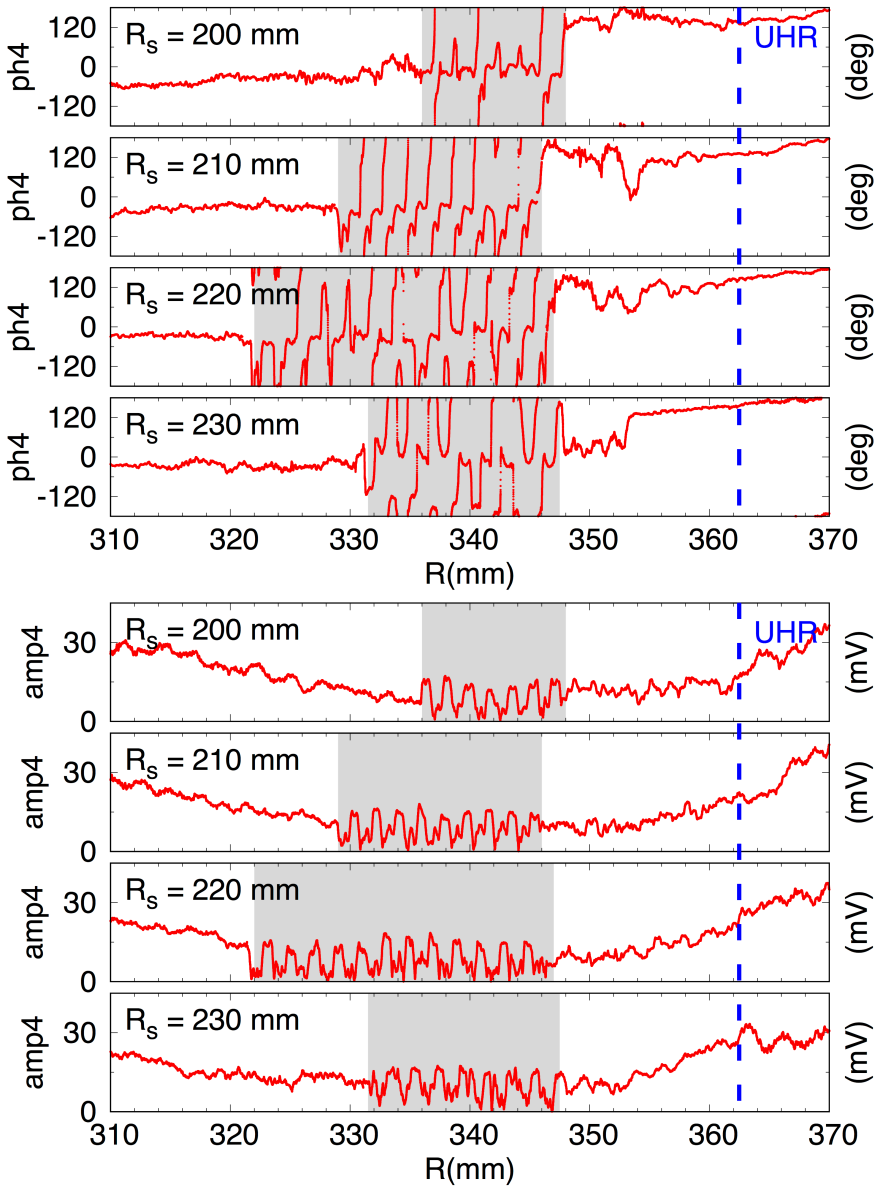

Figure 4.7: 1-D variation of phase (ph4) and amplitude (amp4) calculated from I/Q signals of pin 4 for several sweeps which pass through the short-wavelength region in figure 4.4. The sweeping radius R_s of each sweep is marked on the left top side. The UHR layer is marked by a vertical dashed line.

Here in figure 4.7, phase and amplitude are calculated after taking a

moving average along the sweeping trajectory over 0.2 mm, which clarify the short-wavelength pattern around 2 to 4 mm in the signal. The moving speed of the probe antenna is different for each sweep since the angular speed of axis 1 is fixed while sweeping radius R_s is different. The average number m of sampled data is chosen as the average length $\mathrm{m}v/10^5$ s^{-1} becomes 0.2 mm, where v is the moving speed of the probe antenna.

First, let's inspect phase variation in figure 4.7. In the range of $R \geq 350$ mm and $R \leq 320$ mm, phase variation is pretty slow. In the range of $R = 320$ to 350 mm, a rapid phase variation is detected by pin 4 in four sweeps, as shown in the masked region in figure 4.7. The corresponding wavelength of this rapid phase variation is about 2 mm. By substituting the toroidal magnetic field of 317.6 G, the electron density of 2.8×10^{16} m^{-3}, and the electron temperature of 4 eV at $R = 340$ mm into the EBW dispersion relation [28]

$$1 = \frac{\omega_\mathrm{p}^2}{\omega_\mathrm{c}^2} \frac{2}{\mu} \mathrm{e}^{-\mu} \sum_{\mathrm{n}=1}^{\infty} \frac{I_\mathrm{n}(\mu)}{(\omega/\mathrm{n}\omega_\mathrm{c})^2 - 1} \tag{4.1}$$

the wavelength of EBW is calculated as $\lambda = 2\pi/k_\perp = 2.4$ mm. The group velocity direction of such short-wavelength wave pattern cannot be directly verified from measurement results since homodyne-type circuit is used and I/Q signals are time-independent. However, it is noted that the group velocity direction is same as the wave energy flow direction. Since the UHR layer is located outside the short-wavelength region and the electron temperature is only about 4 eV, it is considered to be nearly impossible that the wave energy flow direction is from inside to outside as there is no strong source inside for exciting such short-wavelength wave pattern. Therefore, through elimination of possibilities, the group velocity direction is considered to be from outside to inside, so the monotonic decrease of phase 4 from outside to inside indicates that it is a backward wave, as the wave has a wave vector $\boldsymbol{k}$ directed outward to the plasma edge, and the phase velocity direction is opposite to the group velocity direction. As mentioned before, the detection direction and moving direction of pin 4 are both almost radial in this region, so the wave is also electrostatic and radially propagating. With all these characteristics, it is believed that the detected short-wavelength wave pattern is EBW.

It should be mentioned that such clear pattern only appears in these four sweeps as shown in figure 4.7, and lasts for several centimeters in each sweep, so the pattern is localized in both toroidal and radial directions. The reason for such localized observation of the EBW wave pattern is considered to be the critical requirement for achieving high O-X-B mode conversion efficiency,

and high collisional damping rate of EBW. First, the parallel refractive index of the injected microwave is expected to have a wide distribution at the PC layer due to its curvature, and the LC layer is not parallel to the PC layer in contrast to conventional 1-D case, therefore, EBW can only be excited in a localized region near the intersection point between the PC layer and the LC layer, which is discussed in more detail in section 4.3. Second, to study the collisional damping effect, the general EBW dispersion relation can be written as [29]

$$1 + \frac{1}{k^2\lambda_{\mathrm{D}}^2} \times \frac{1 + z_0 \sum_{\mathrm{n}=-\infty}^{\infty} \mathrm{e}^{-\mu} I_{\mathrm{n}}(\mu) Z(z_{\mathrm{n}})}{1 + \mathrm{i} z_{\mathrm{c}} \sum_{\mathrm{n}=-\infty}^{\infty} \mathrm{e}^{-\mu} I_{\mathrm{n}}(\mu) Z(z_{\mathrm{n}})} = 0 \tag{4.2}$$

where $k = (k_z^2 + k_\perp^2)^{1/2}$ is the wave number, $k_z = N_z\omega/c$, $\lambda_{\mathrm{D}} = v_{\mathrm{th}}/\sqrt{2}\omega_{\mathrm{p}}$ is the Debye length, $z_{\mathrm{n}} = (\omega + i\nu - \mathrm{n}\omega_{\mathrm{c}})/k_z v_{\mathrm{th}}$, ν is the collision frequency, $z_{\mathrm{c}} = \nu/k_z v_{\mathrm{th}}$, Z is the plasma dispersion function. The collision frequency is estimated to be $\nu \sim 5 \times 10^7$ s^{-1} under present warm plasma conditions with the electron temperature of 4 eV and gas pressure of 0.6×10^{-2} Pa [30] (both electron-ion and electron-neutral collisions are considered with the possibility of impurities from the wall), and the parallel refractive index is also estimated to be $N_z \sim 0.611$ (section 4.3). By substituting these parameters into the dispersion relation, the complex value of the perpendicular wave number can be solved as $k_\perp = 2679.5 - 334.5i$ m^{-1}, and the collisional damping length of EBW is estimated to be $\lambda_{\mathrm{damping}} = 2\pi/\mathrm{Im}(k_\perp) = 1.9$ cm in present experiments, so the EBW wave pattern is expected to quickly damp and disappear within several centimeters after being excited locally.

Next, let's inspect amplitude variation in figure 4.7. In the range of R = 320 to 350 mm, overall amplitude level becomes small and the variation shows similar periods as phase variation. As mentioned before, the probe antenna is able to detect two types of electric fields, one is electromagnetic type which is parallel to the pin, the other is electrostatic type which is perpendicular to the pin. Since the diameter of the pin is only 0.1 mm, the electrostatic type is expected to induce weaker currents in the pin than the electromagnetic type, which may be the reason of small overall amplitude level in the EBW region. To understand the amplitude variation, general relationship between EBW wave fields and phase and amplitude of each pin is described. The EBW wave potential can be written as

$$\psi(\boldsymbol{r}, t) = \sum_{\mathrm{j}} A_{\mathrm{j}}(\boldsymbol{r}) \exp[i(\phi_{\mathrm{j}0} + \boldsymbol{k}_{\mathrm{j}} \cdot \boldsymbol{r}) - i\omega t] \tag{4.3}$$

where j denotes multiple waves in different directions. The probe antenna detects the potential difference between the corner pin and the center pin as

$$\Delta\psi_{\mathrm{i}}(\boldsymbol{r},t) = \psi(\boldsymbol{r}+\boldsymbol{d}_{\mathrm{i}},t) - \psi(\boldsymbol{r},t) \tag{4.4}$$

where i = 1, 2, 3, 4 for four pins, $\boldsymbol{d}_{\mathrm{i}}$ denotes the vector from the center pin to each corner pin. A schematic diagram of the detection scenario is shown in figure 4.8.

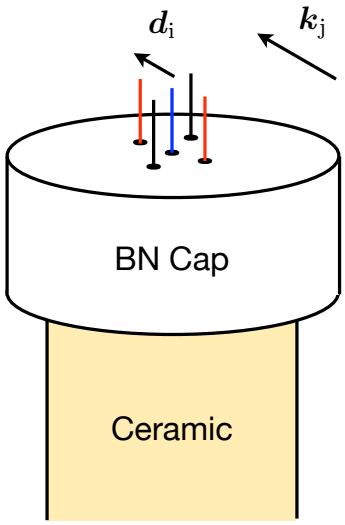

Figure 4.8: A schematic diagram of the detection scenario. i = 1, 2, 3, 4 for four pins, $\boldsymbol{d}_{\mathrm{i}}$ denotes the vector from the center pin to each corner pin, and j denotes multiple waves in different directions.

Now assuming that the wave amplitude is constant in the small distance of d_{i} (1 mm), the potential difference can be written as

$$\begin{aligned}\Delta\psi_{\mathrm{i}}(\boldsymbol{r},t) = &\sum_{\mathrm{j}} 2A_{\mathrm{j}} \sin\left(\frac{\boldsymbol{k}_{\mathrm{j}}\cdot\boldsymbol{d}_{\mathrm{i}}}{2}\right) \\ &\times \exp\left[i\left(\phi_{\mathrm{j}0} + \boldsymbol{k}_{\mathrm{j}}\cdot\boldsymbol{r} + \frac{\boldsymbol{k}_{\mathrm{j}}\cdot\boldsymbol{d}_{\mathrm{i}}}{2} + \frac{\pi}{2}\right) - i\omega t\right]\end{aligned} \tag{4.5}$$

I/Q signals are the time-independent parts as $I_{\mathrm{i}} = \mathrm{Re}(\Delta\psi_{\mathrm{i}}(\boldsymbol{r}))$, $Q_{\mathrm{i}} = \mathrm{Im}(\Delta\psi_{\mathrm{i}}(\boldsymbol{r}))$, so phase $\phi_{\mathrm{i}} = \arg(\Delta\psi_{\mathrm{i}}(\boldsymbol{r}))$, amplitude $A_{\mathrm{i}} = |\Delta\psi_{\mathrm{i}}(\boldsymbol{r})|$. It is clear that the pin detection direction, pin moving direction and wave propagation direction can both affect phase and amplitude pattern. In the ideal case where there is only one wave and the these three directions are the same for one pin,

$\phi = \phi_{\mathrm{EBW0}} + k_{\mathrm{EBW}} r + k_{\mathrm{EBW}} d/2 + \pi/2$ as phase decreases monotonically in the period of the wavelength for a backward EBW, $A = 2A_{\mathrm{EBW}} \sin(k_{\mathrm{EBW}} d/2)$ as amplitude is constant. It should be mentioned that here it is assumed $\boldsymbol{k}_{\mathrm{j}} \cdot \boldsymbol{d}_{\mathrm{i}} \neq 2\mathrm{n}\pi$, where n is an integer. In the case of $\boldsymbol{k}_{\mathrm{j}} \cdot \boldsymbol{d}_{\mathrm{i}} = 2\mathrm{n}\pi$, the potential difference between the center pin and corner pin is zero, and no pattern variation should be detected. It should also be mentioned that for waves with wavelength shorter than $2d_{\mathrm{i}}$ (2 mm), they should be detected as a spatially under-sampled pattern with effective length of variation equal to $2d_{\mathrm{i}}$.

From figure 4.7, it is noted that amplitude shows clear variation with similar periods as phase variation. This suggests that the wave potential forms an interference wave pattern rather than a pure plane wave, and the pin detection direction, pin moving direction and wave propagation directions are not exactly the same. In theory, wave interference may occur between EBWs from different directions, or between EBW and SX-mode. However, the PC layer is at $R_{\mathrm{PC}} = 337.6$ mm, and the short-wavelength region is in the range of $R = 320$ to 348 mm. Since the SX-mode is not likely to exist in the inner side of the PC layer, the interference wave pattern should be due to EBWs only. In the experiment, the density fluctuation effect cannot be neglected, and the UHR layer is not expected to be smooth, so there may exist multiple electrostatic waves in different directions near the UHR layer, which could form the interference wave pattern and result in such amplitude variation.

4.2 X-mode injection

For comparison with O-mode injection, the RF power generator is connected to the vertical side of the waveguide launcher and 1.5 GHz microwave is injected as X-mode. Both the electron density and temperature profiles, 1-D and 2-D wave pattern of phase and amplitude are measured and compared with O-mode injection results.

4.2.1 Target plasma and discharge waveform

The typical discharge waveform and I/Q signals during one sweep for X-mode injection are shown in figure 4.9 and figure 4.10, respectively. The control parameters are the same as in figure 4.1 and the sweeping trajectory is the same as in figure 4.2. Comparison between figure 4.1 and figure 4.9, figure 4.2 and figure 4.10 show that the target plasma is almost the same for both cases, while I/Q signals are quite different. For X-mode injection, typical I/Q signal level is smaller than O-mode injection case.

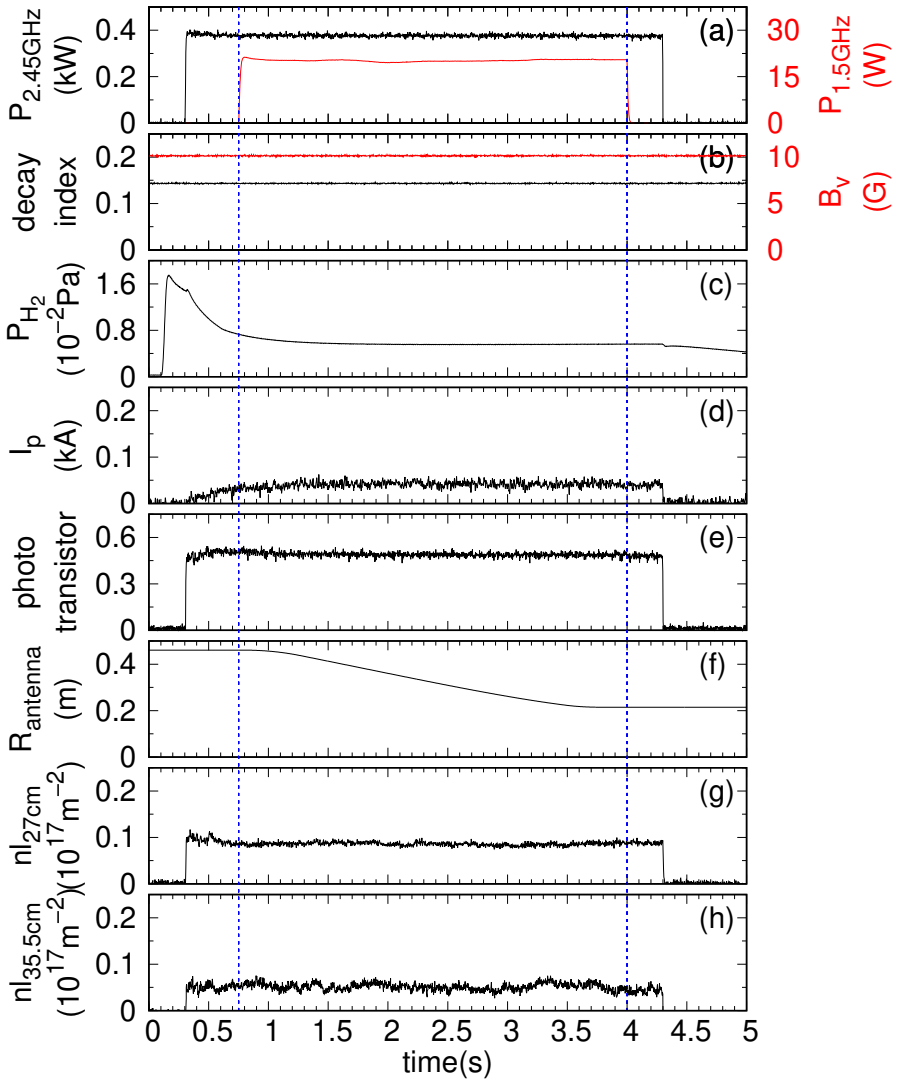

Figure 4.9: A typical discharge waveform for X-mode injection: (a) 2.45 GHz heating microwave power and 1.5 GHz detecting microwave power, (b) vertical magnetic field B_v and its decay index $-(R/B_v)\cdot(\partial B_v/\partial R)$, (c) gas pressure, (d) plasma current, (e) plasma light, (f) radial position of the probe antenna, (g) and (h) line-integrated electron densities along 27 and 35.5 cm chord. The steady state period (0.75 to 4.0 s) is marked by vertical dashed lines.

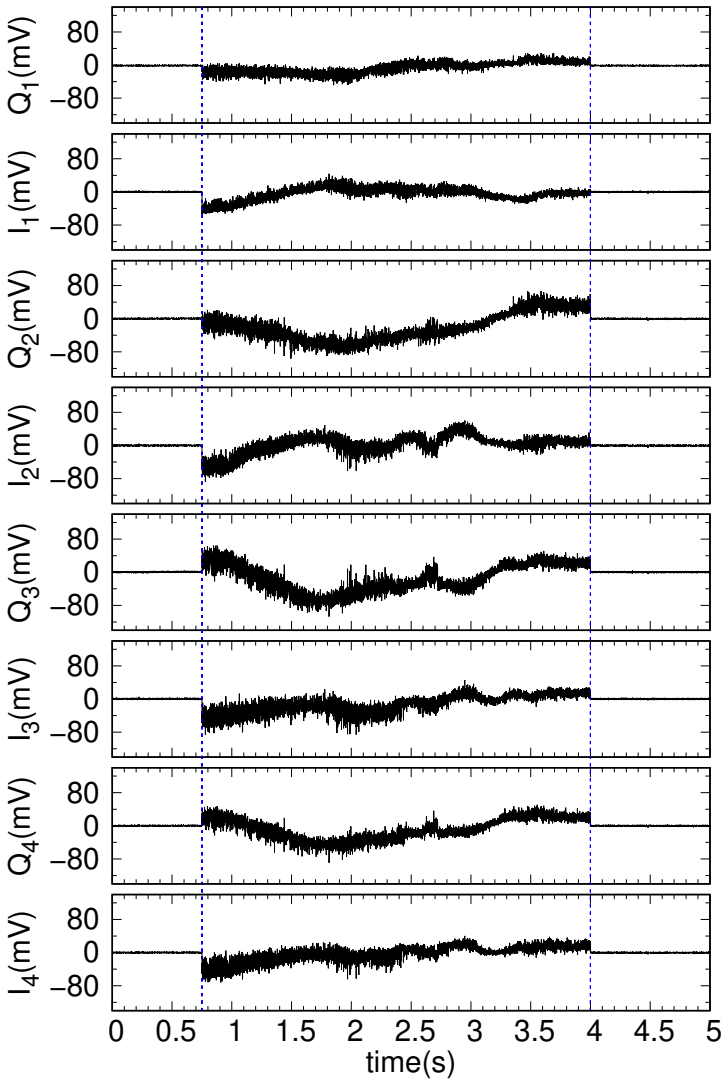

Figure 4.10: Typical I/Q signals for X-mode injection during one sweep $R_{\rm s}$ = 220 mm. The suffix numbers indicate the antenna pin numbers, and there are eight channels for four pins.

The electron density and temperature profiles are shown in figure 4.11. Compared with O-mode injection case, the UHR and PC layers move slightly from $R_{\rm UHR-O} = 362.5$ mm to $R_{\rm UHR-X} = 367.3$ mm, and $R_{\rm PC-O} = 337.6$ mm to $R_{\rm PC-X} = 345.3$ mm, respectively, while the electron temperature profile

is almost the same.

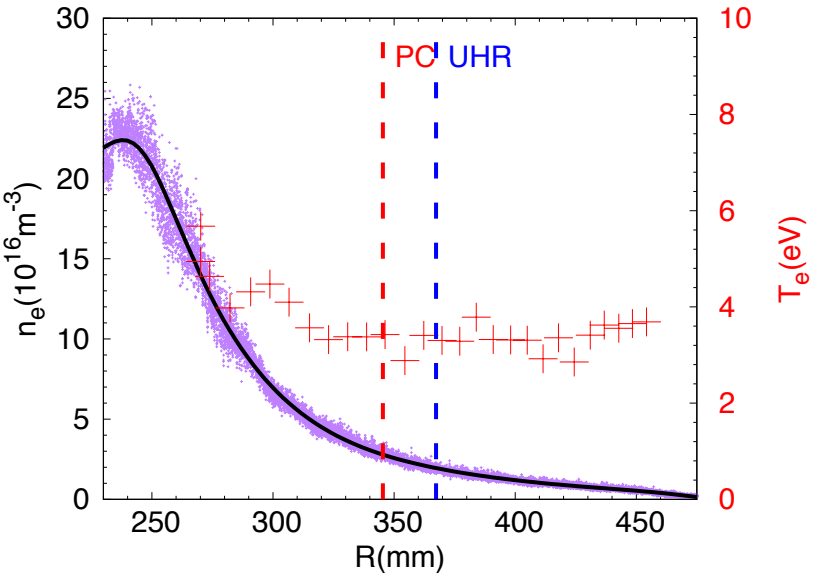

Figure 4.11: The electron density and temperature profiles for X-mode injection. The ion saturation current measurement results and the fitting curve (after 10.7×10^{16} m^{-3}/mA factor multiplication) are plotted by purple points and a black line, respectively. The electron density and temperature obtained from the $I-V$ characteristics are plotted by black stars and red crosses, respectively. The UHR and PC layers are marked by vertical dashed lines.

4.2.2 2-D wave pattern

Figure 4.12 and figure 4.13 show two-dimensional plots of phase and amplitude pattern for X-mode injection. The plot setting is the same as in figure 4.4 and figure 4.5, except that the first five sweeps near the waveguide launcher ($R_s = 70$ to 110 mm) are not measured, as the plasma is difficult to be maintained and discharge is terminated during these sweeps for X-mode injection. It is noted that the overall wave pattern of phase and amplitude is quite different from O-mode injection case for all four pins. For the 2-D wave pattern of phase, no short-wavelength wave pattern can be observed. Under present experimental conditions as the X-mode is injected obliquely, the X-B mode conversion efficiency is at a very low level of about 8.6% [31, 32] and

EBW is not expected to be excited effectively. In the case of perpendicular injection of the X-mode, the X-B mode conversion efficiency is estimated to be about 88.6%, which is much higher. The formation of a resonant cavity between the R-cutoff, UHR, and L-cutoff is the reason for such high conversion efficiency, even though the evanescent region and wave tunneling are always involved. Since the process is not fully understood in detail, the detection system is expected to be used for future study of the X-B mode conversion process with microwave perpendicularly injected. For the 2-D wave pattern of amplitude, the overall amplitude level is smaller than O-mode injection case, as FX-mode is quickly blocked at the RC layer and cannot penetrate inside the plasma. A standing wave pattern appears near the wall ($R = 380$ to 460 mm) with a wavelength of about 15 cm, due to the reflection of the FX-mode between the RC layer and the 4R and 5R ports of LATE.

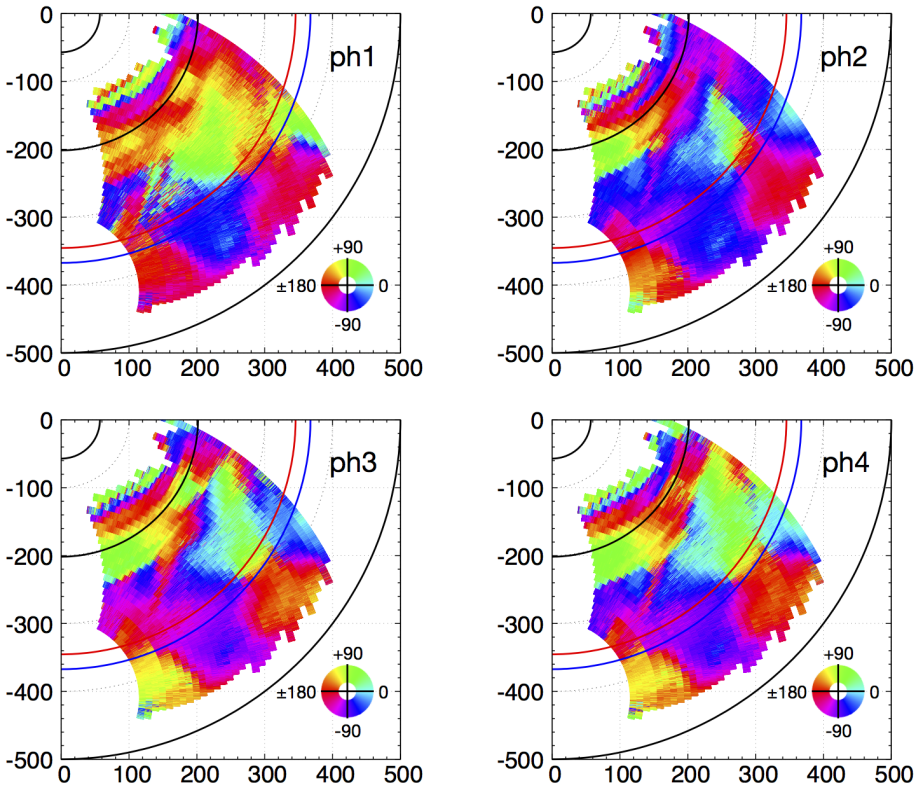

Figure 4.12: Two-dimensional plots of phase pattern measured by four pins for X-mode injection. Phase calculated from I/Q signals of pin 1 is shown by ph1, and so on. The LATE wall, UHR, PC, ECR layers and center post are marked by five solid curves from outside to inside, respectively. The phase and coordinate unit are degree and millimeter, respectively. The first five sweeps near the waveguide launcher (R_s = 70 to 110 mm) are not measured compared with figure 4.4 due to discharge termination.

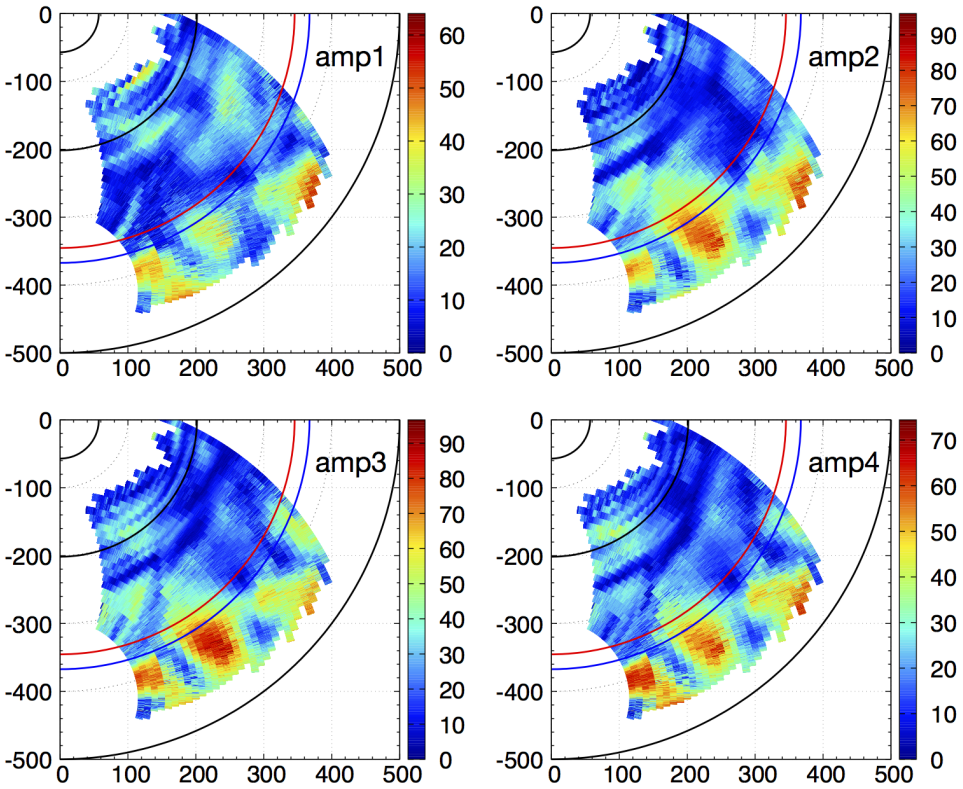

Figure 4.13: Two-dimensional plots of amplitude pattern measured by four pins for X-mode injection. Amplitude calculated from I/Q signals of pin 1 is shown by amp1, and so on. The LATE wall, UHR, PC, ECR layers and center post are marked by five solid curves from outside to inside, respectively. The amplitude and coordinate unit are millivolt and millimeter, respectively. The first five sweeps near the waveguide launcher (R_s = 70 to 110 mm) are not measured compared with figure 4.5 due to discharge termination.

4.3 Toroidal magnetic field adjustment

To further investigate the EBW wave pattern observed in figure 4.4, the toroidal magnetic field coil current is slightly adjusted to 920 A while other control parameters are kept the same as in figure 4.1, and 1.5 GHz microwave is injected as O-mode. Both the electron density and temperature profiles, 1-D and 2-D wave pattern of phase and amplitude are measured and compared with 900 A case. The results are shown in figure 4.14 and figure 4.15.

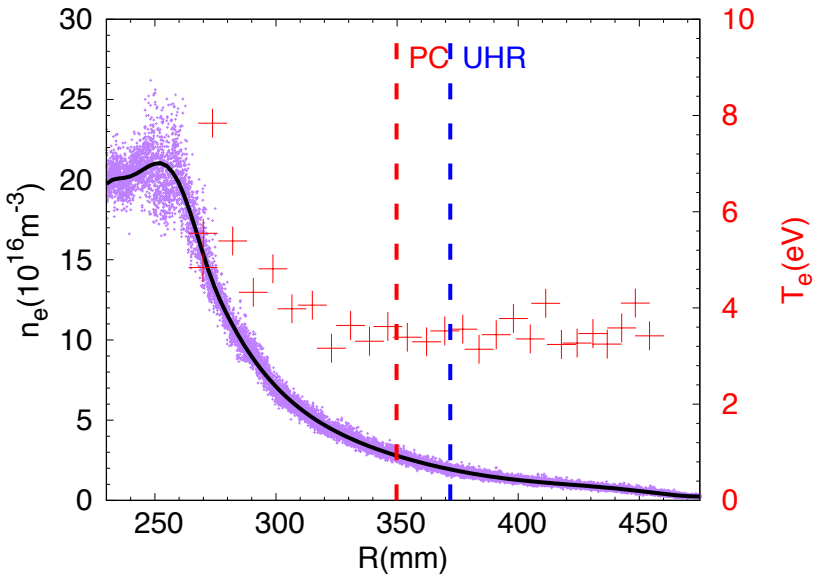

Figure 4.14: The electron density and temperature profiles for O-mode injection for 920 A toroidal magnetic field coil current. The ion saturation current measurement results and the fitting curve (after 10.7×10^{16} m^{-3}/mA factor multiplication) are plotted by purple points and a black line, respectively. The electron temperature obtained from the $I - V$ characteristics are plotted by red crosses. The UHR and PC layers are marked by vertical dashed lines.

From figure 4.14, it is noted that the electron density profile is slightly changed after increasing the toroidal magnetic field, while the electron temperature profile is almost the same. The UHR, PC, and ECR layers move from $R_{\mathrm{UHR-900}} = 362.5$ mm to $R_{\mathrm{UHR-920}} = 372.0$ mm, $R_{\mathrm{PC-900}} = 337.6$ mm to $R_{\mathrm{PC-920}} = 349.8$ mm, and $R_{\mathrm{ECR-900}} = 201.5$ mm to $R_{\mathrm{ECR-920}} = 206.0$ mm, respectively. However, the plasma is still highly overdense and three layers are also well separated.

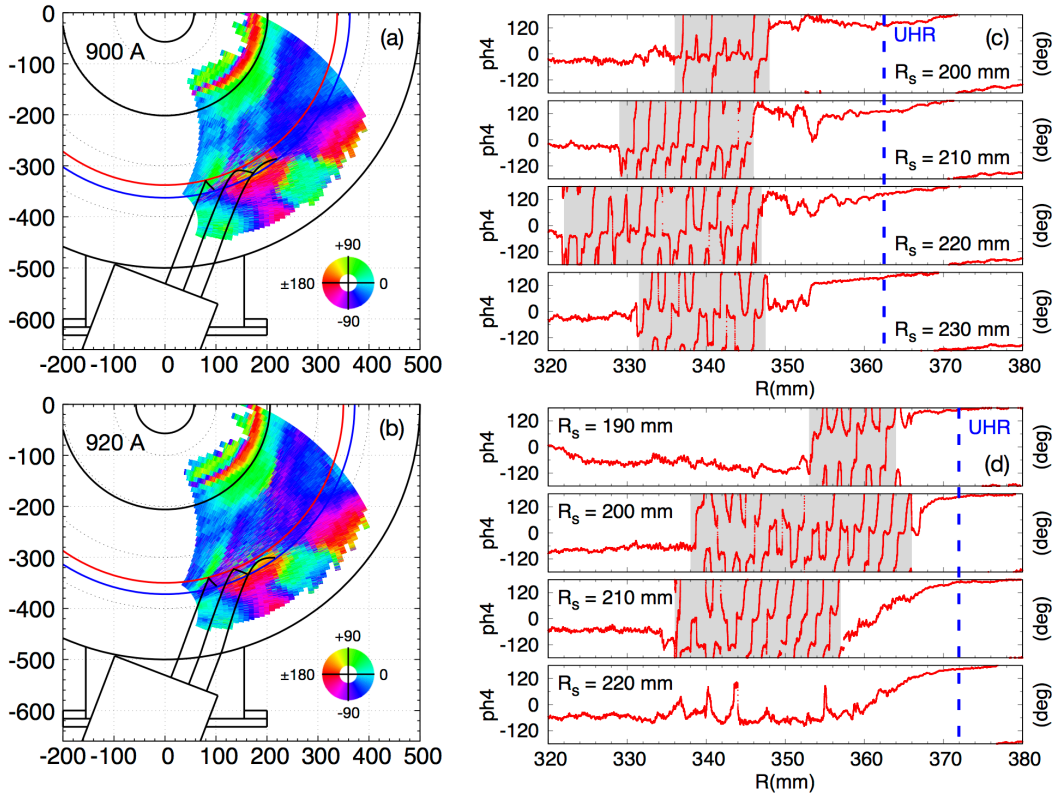

Figure 4.15: Left: comparison of 2-D wave pattern of phase measured by pin 4 for (a) 900 A and (b) 920 A toroidal magnetic field coil current. The LATE wall, UHR, PC, ECR layers and center post are marked by five solid curves from outside to inside, respectively. The phase and coordinate unit is degree and millimeter, respectively. The approximate wave trajectories from the launcher to the plasma are shown by black curves. Right: comparison of 1-D wave pattern of phase measured by pin 4 for (c) 900 A and (d) 920 A toroidal magnetic field coil current. The sweeping radius R_s of each sweep is marked. The UHR layer is marked by a vertical dashed line.

From figure 4.15, several results can be noted.

First, the overall wave pattern of phase 4 for 920 A is highly similar to 900 A case. The EBW wave pattern near the UHR layer appears once again after increasing the toroidal magnetic field.

Second, the position of the EBW region changes for different toroidal magnetic fields. From both 2-D and 1-D wave pattern of phase in figure 4.15, it is noted that the position of the EBW region moves not only radially

but also toroidally (sweeping radius becomes different) after increasing the toroidal magnetic field (from $x_{900} = 155$ to 185 mm, $y_{900} = -300$ to -335 mm, to $x_{920} = 150$ to 175 mm, $y_{920} = -320$ to -345 mm). While the radial movement is easily understood as the postion of the UHR layer is shifted, the toroidal movement of the EBW region suggests the existence of a localized region where O-X mode conversion efficiency is high. In the O-X conversion process, the O-mode tunnels through the evanescent region between the PC layer and the LC layer and converts to the X-mode. In conventional 1-D case, the evanescent region will disappear at an optimal injection angle when these two layers overlap. In present 2-D case, however, the evanescent region will not disappear since these two layers are not parallel to each other, as the parallel refractive index of the microwave is not constant at the PC layer, due to the plane wave assumption and PC layer curvature. In fact, there is an intersection point between the PC layer and the LC layer, and O-X mode conversion efficiency is expected to be high only near this intersection point. A schematic diagram of the intersection between the PC layer and the LC layer in 2-D case is shown in figure 4.16.

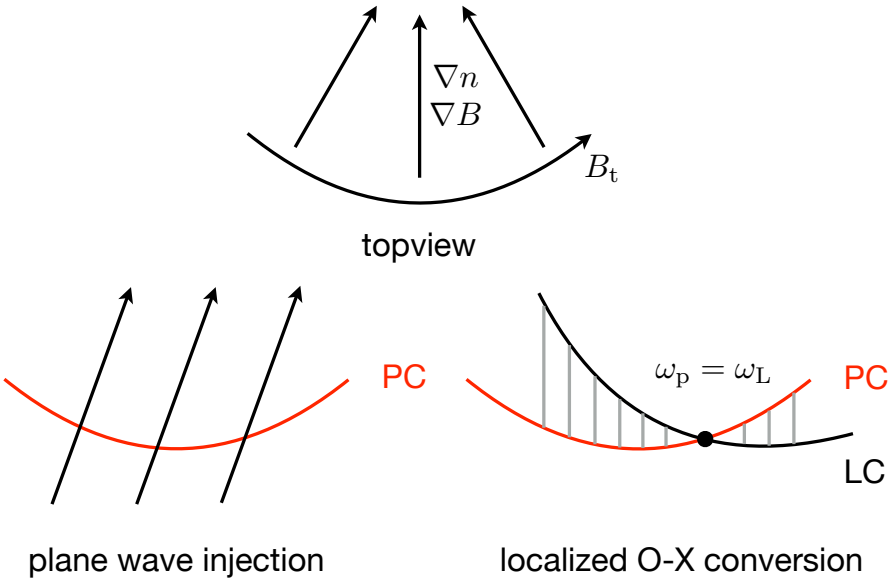

Figure 4.16: A schematic diagram of the intersection between the PC layer and the LC layer in 2-D case.

It should be mentioned that both the plasma current and vertical magnetic field are very small in present experiments, so the total magnetic field

profile is mainly determined by the toroidal magnetic field coil current, and the electron density gradient direction is almost the same as the magnetic field gradient direction. The parallel refractive index of the microwave at the intersection point can be calculated as follows,

$$\omega = \frac{1}{2}\left(\sqrt{\omega_c^2 + \frac{4\omega_p^2}{1 - N_z^2}} - \omega_c\right) = \omega_L \tag{4.6}$$

At $R = R_{PC}$, $\omega_p = \omega$, the equation gives the well-known $N_z = N_{zc} = \sqrt{\omega_c/(\omega + \omega_c)}$. By substituting with the toroidal magnetic field at the PC layer $B_{900} = 320.0$ G and $B_{920} = 315.6$ G, one gets $N_{z-900} = 0.611$, $N_{z-920} = 0.609$, so the corresponding angle between k and k_z is $\theta_{900} = 52.3^o$, $\theta_{920} = 52.5^o$. It is noted that both shifts are very small due to slight adjustment of the toroidal magnetic field. In the experiment, such slight adjustment will keep the plasma and 2-D wave pattern highly similar and make it possible for intuitive comparison. Larger adjustment of the toroidal magnetic field will unavoidably change the plasma profile and 2-D wave pattern will also become dramatically different. The position of the intersection point between the PC layer and the LC layer is difficult to be calculated accurately as the wave trajectory cannot be determined from conventional ray tracing technique (wavelength is comparable to LATE radius). However, such ray tracing calculation is still performed and approximate wave trajectories from the launcher to the plasma are plotted in figure 4.15, in order to demonstrate the process. The microwave is obliquely injected to the plasma, while only certain wave trajectories may reach the region adjacent to the intersection point between the PC layer and the LC layer where O-X conversion efficiency is high. After O-X conversion, converted SX-mode propagates back to the UHR layer, and eventually converts to EBW. Therefore, the position of the EBW region becomes localized and is determined by such certain wave trajectories.

Third, the size of the EBW region changes for different toroidal magnetic fields. From 1-D wave pattern of phase in figure 4.15, it is noted that there are only three sweeps where the EBW wave pattern is clearly observed after increasing the toroidal magnetic field as shown in the masked region, while the length of the masked region is almost the same. It should be noted that the interval between the sweeps is 1 cm, so much smaller size change may not be verified precisely in present experiments. By substituting with the plasma parameters in 920 A case, the complex value of the perpendicular wave number can be solved as $k_{\perp-920} = 2597.6 - 341.9i$ m^{-1}, so the collisional damping length of EBW is nearly the same with 900 A case. Besides collisional damping, the size of the EBW region depends on the total O-X-B

conversion efficiency, which includes two processes. For the first process, as mentioned before, O-X mode conversion efficiency is high near the intersection point between the PC layer and the LC layer. The total O-X conversion efficiency, however, cannot be calculated by Mjølhus' formula [25]

$$C_{\mathrm{O-SX}} = \exp\left\{-\pi k_0 L_n \sqrt{\frac{\omega_{\mathrm{c}}}{2\omega}}\left[2\left(1+\frac{\omega_{\mathrm{c}}}{\omega}\right)(N_z - N_{zc})^2 + N_y^2\right]\right\} \tag{4.7}$$

Since the evanescent region between the PC layer and the LC layer only disappears at the intersection point and the wave energy has a spatial distribution, the total penetration rate for O-X conversion is dependent on both the evanescent region shape and wave energy spatial distribution. For the second process, there is a possibility that the converted SX-mode tunnels through another evanescent region between the UHR layer and the RC layer and propagates outside, which will decrease the conversion efficiency. Similarly, the total tunneling rate is also dependent on the evanescent region shape and the wave energy spatial distribution. Though the total O-X-B conversion efficiency is difficult to be calculated precisely, it should be mentioned that the EBW wave pattern is still observed for much higher toroidal magnetic field ($I_{\mathrm{t}} = 1000$ A), and the size becomes slightly smaller (only two sweeps). Such results suggest that localized efficient O-X-B conversion can always be achieved in present 2-D case due to the existence of the intersection point, while the total conversion efficiency may be different.

Chapter 5

Discussion

5.1 Comparison with 1-D full wave simulation

For comparison with the experimental results in the EBW region, 1-D full wave simulation is performed by solving the simplified kinetic full wave equation [23]. The kinetic full wave equation is

$$\frac{\mathrm{d}\boldsymbol{F}_{\mathrm{K}}}{\mathrm{d}\xi} = i\boldsymbol{A}_{\mathrm{K}} \cdot \boldsymbol{F}_{\mathrm{K}} \tag{5.1}$$

where

$$\begin{aligned}
&\xi = \omega x/c \\
&\boldsymbol{F}_{\mathrm{K}} = \left[E_x, E_y, E_z, \left(i\widetilde{\chi}E_x'\right), cB_z, \left(-cB_y\right)\right]^{\mathrm{T}} \\
&\boldsymbol{A}_{\mathrm{K}} = \begin{pmatrix}
0 & 0 & 0 & -\widetilde{\chi}^{-1} & 0 & 0 \\
N_y & 0 & 0 & 0 & 1 & 0 \\
N_z & 0 & 0 & 0 & 0 & 1 \\
K_1 & -iK_2 & 0 & 0 & N_y & N_z \\
iK_2 & K_1 - N_z^2 & N_yN_z & 0 & 0 & 0 \\
0 & N_yN_z & K_3 - N_y^2 & 0 & 0 & 0
\end{pmatrix} \\
&\widetilde{\chi} = \frac{-3\omega_{\mathrm{p}}^2\left(\omega + i\nu\right)^2}{\left[\left(\omega + i\nu\right)^2 - \omega_{\mathrm{c}}^2\right]\left[\left(\omega + i\nu\right)^2 - 4\omega_{\mathrm{c}}^2\right]}\left(\frac{v_{\mathrm{th}}}{c}\right)^2
\end{aligned} \tag{5.2}$$

The full wave equation 5.1 cannot be solved until the appropriate boundary conditions for the differential equations are specified. In order to formulate these boundary conditions, it is first necessary to investigate the wave propagation in a homogeneous plasma.

In a homogeneous plasma, $\boldsymbol{F}_{\mathrm{K}}(\xi)$ can be written as

$$\boldsymbol{F}_{\mathrm{K}}(\xi) = \boldsymbol{F}_0 \exp\left(iN_x\xi\right) \tag{5.3}$$

Inserting equation 5.3 into 5.1 reduces the differential equation to the linear eigenvalue problem

$$\boldsymbol{A}_{\mathrm{K}} \cdot \boldsymbol{F}_0 = N_x \boldsymbol{F}_0 \tag{5.4}$$

The eigenvalues belonging to equation 5.4 can be written in the form

$$\begin{aligned} N_{x1}^2 &= \frac{-b - 2\sqrt{A}\cos(\theta/3)}{3a} \\ N_{x2}^2 &= \frac{-b + \sqrt{A}(\cos(\theta/3) + \sqrt{3}\sin(\theta/3))}{3a} \\ N_{x3}^2 &= \frac{-b + \sqrt{A}(\cos(\theta/3) - \sqrt{3}\sin(\theta/3))}{3a} \end{aligned} \tag{5.5}$$

where

$$\begin{aligned} a &= \widetilde{\chi} \\ b &= K_1 + \widetilde{\chi}\left(N_y^2 + N_z^2 - K_1 - K_3\right) \\ c &= K_2^2 + K_1\left(2N_y^2 + N_z^2 - K_1 - K_3\right) \\ &\quad + K_3 N_z^2 - \widetilde{\chi}\left(K_1 N_y^2 + K_3 N_z^2 - K_1 K_3\right) \\ d &= -K_2^2\left(K_3 - N_y^2\right) \\ &\quad + \left(N_y^2 + N_z^2 - K_1\right)\left(K_1 N_y^2 + K_3 N_z^2 - K_1 K_3\right) \\ A &= b^2 - 3ac \\ B &= bc - 9ad \\ C &= c^2 - 3bd \\ T &= \frac{2Ab - 3aB}{2\sqrt{A^3}} \\ \theta &= \arccos T \end{aligned} \tag{5.6}$$

In figure 5.1 we show the variation of N_x^2 with normalized density.

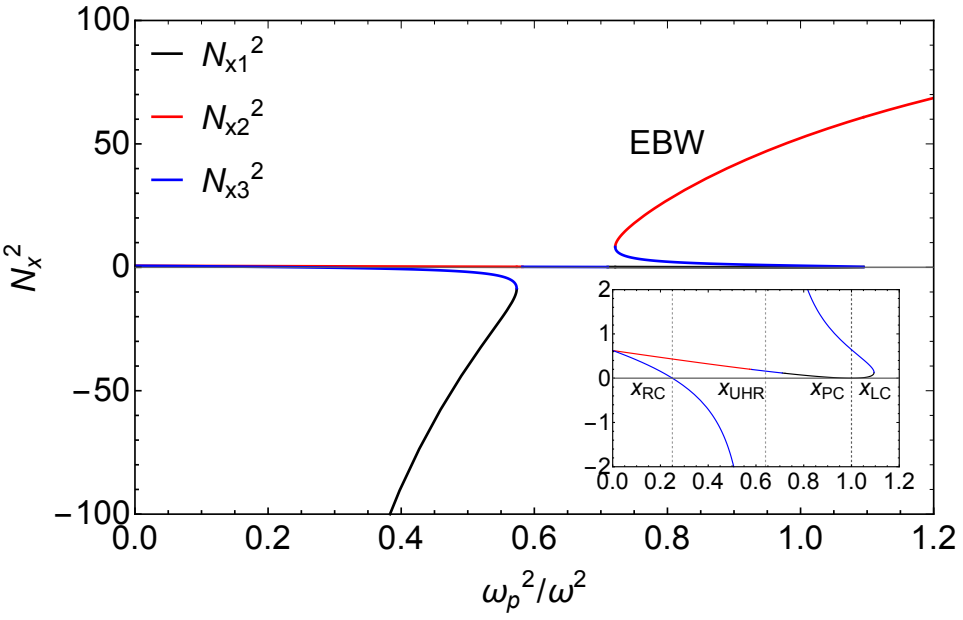

Figure 5.1: Variation of N_x^2 with normalized density. $N_z = N_{zc}$, $\omega_c/\omega = 0.6$, $T_e = 500$ eV.

We recognize that in the low density region, the N_{x1}^2 solution corresponds to the decaying wave, the N_{x2}^2 solution corresponds to the O-wave, and the N_{x3}^2 solution corresponds to the fast X-wave. While in the high density region, the N_{x1}^2 solution corresponds to the decaying wave, the N_{x2}^2 solution corresponds to the electron Bernstein wave, and the N_{x3}^2 solution corresponds to another decaying wave.

Once the eigenvalues N_x corresponding to equation 5.4 are found, we can calculate the eigenvectors $\boldsymbol{F}_{\text{eigen}}(N_x) = (p_1, p_2, p_3, p_4, p_5, p_6)^{\text{T}}$ as

$$\begin{pmatrix} -N_x & 0 & 0 & -\widetilde{\chi}^{-1} & 0 & 0 \\ N_y & -N_x & 0 & 0 & 1 & 0 \\ N_z & 0 & -N_x & 0 & 0 & 1 \\ K_1 & -iK_2 & 0 & -N_x & N_y & N_z \\ iK_2 & K_1 - N_z^2 & N_y N_z & 0 & -N_x & 0 \\ 0 & N_y N_z & K_3 - N_y^2 & 0 & 0 & -N_x \end{pmatrix} \cdot \begin{pmatrix} p_1 \\ p_2 \\ p_3 \\ p_4 \\ p_5 \\ p_6 \end{pmatrix} = \begin{pmatrix} 0 \\ 0 \\ 0 \\ 0 \\ 0 \\ 0 \end{pmatrix} \tag{5.7}$$

The total solution for $\boldsymbol{F}_{\text{K}}(\xi)$ in a homogeneous plasma can now be written

as a linear combination of the six independent eigenmodes:

$$\boldsymbol{F}_{\mathrm{K}}(\xi) = \sum_{\mathrm{j}=1}^{6} \boldsymbol{F}_{\mathrm{Kj}} \exp\left(iN_{\mathrm{j}}\xi\right) = \sum_{\mathrm{j}=1}^{6} c_{\mathrm{j}} \boldsymbol{P}_{\mathrm{j}} \exp\left(iN_{\mathrm{j}}\xi\right) \tag{5.8}$$

where c_{j} is a complex constant with the dimensions of an electric field. The components $p_{1\mathrm{j}}$, $p_{2\mathrm{j}}$, $p_{3\mathrm{j}}$, $p_{4\mathrm{j}}$, $p_{5\mathrm{j}}$ and $p_{6\mathrm{j}}$ of the polarization vector $\boldsymbol{P}_{\mathrm{j}}$ are determined by equation 5.7 with $N_x = N_{\mathrm{j}}$. And $\boldsymbol{F}_{\mathrm{Kj}}$ is determined by

$$\boldsymbol{A}_{\mathrm{K}} \cdot \boldsymbol{F}_{\mathrm{Kj}} = N_{\mathrm{j}} \boldsymbol{F}_{\mathrm{Kj}} \tag{5.9}$$

In table 5.1 we show the distinction between N_1, N_2, N_3, N_4, N_5 and N_6. Here, outgoing and incoming refers to propagating waves with their energy flow density towards the low density and the high density regions, respectively.

Table 5.1: Distinction between N_1, N_2, N_3, N_4, N_5 and N_6.

	value	representation	
		low density region (ξ_1)	high density region (ξ_2)
N_1	$\sqrt{N_{x1}^2}$	decaying wave	growing wave 1
N_2	$-\sqrt{N_{x1}^2}$	growing wave	decaying wave 1
N_3	$\sqrt{N_{x2}^2}$	incoming O-wave	outgoing EBW
N_4	$-\sqrt{N_{x2}^2}$	outgoing O-wave	incoming EBW
N_5	$\sqrt{N_{x3}^2}$	incoming fast X-wave	decaying wave 2
N_6	$-\sqrt{N_{x3}^2}$	outgoing fast X-wave	growing wave 2

Now, the two boundaries are taken to be away from the mode conversion region where the perpendicular wave vectors, obtained from the WKB dispersion relation, change slowly compared to the density scale length. Then, at the two boundaries, the six waves are assumed to be independent and uncoupled, and the solutions to equation 5.1 can be obtained by using the WKB approximation.

The solutions at the two boundaries $\boldsymbol{F}_{\mathrm{K}}(\xi_1)$ and $\boldsymbol{F}_{\mathrm{K}}(\xi_2)$ are determined by the amplitudes of the eigenmodes c_{j} at the two boundaries as

$$\begin{bmatrix} c_1 \exp\left(iN_1\xi\right) \\ c_2 \exp\left(iN_2\xi\right) \\ c_3 \exp\left(iN_3\xi\right) \\ c_4 \exp\left(iN_4\xi\right) \\ c_5 \exp\left(iN_5\xi\right) \\ c_6 \exp\left(iN_6\xi\right) \end{bmatrix}_{\xi=\xi_1} = \left(\begin{array}{cccccc} \boldsymbol{P}_1 & \boldsymbol{P}_2 & \boldsymbol{P}_3 & \boldsymbol{P}_4 & \boldsymbol{P}_5 & \boldsymbol{P}_6 \end{array} \right)^{-1}_{\xi=\xi_1} \cdot \boldsymbol{F}_{\mathrm{K}}(\xi_1) \tag{5.10}$$

$$\begin{bmatrix} c_1 \exp(iN_1\xi) \\ c_2 \exp(iN_2\xi) \\ c_3 \exp(iN_3\xi) \\ c_4 \exp(iN_4\xi) \\ c_5 \exp(iN_5\xi) \\ c_6 \exp(iN_6\xi) \end{bmatrix}_{\xi=\xi_2} = \begin{pmatrix} \boldsymbol{P}_1 & \boldsymbol{P}_2 & \boldsymbol{P}_3 & \boldsymbol{P}_4 & \boldsymbol{P}_5 & \boldsymbol{P}_6 \end{pmatrix}^{-1}_{\xi=\xi_2} \cdot \boldsymbol{F}_{\mathrm{K}}(\xi_2) \quad (5.11)$$

For present experiments of mode conversion and excitation of EBW, the boundary conditions are set as follows.

At the low density boundary, the field amplitude of the incoming O-mode is preset, and the field amplitudes of the incoming X-mode and spatially growing wave are set to zero.

$$\begin{aligned} I_{\mathrm{O}} &= I_{\mathrm{O}} \\ I_{\mathrm{X}} &= 0 \\ G &= 0 \end{aligned} \quad (5.12)$$

At the high density boundary, the field amplitudes of the spatially growing O-mode and X-mode, and of the outgoing EBW are set to zero.

$$\begin{aligned} G_{\mathrm{O}} &= 0 \\ G_{\mathrm{X}} &= 0 \\ I_{\mathrm{B}} &= 0 \end{aligned} \quad (5.13)$$

The formation of a standard two-point boundary value problem is now complete. The kinetic full wave equation 5.1 can be solved subject to the algebraic boundary conditions. A schematic diagram of the boundary conditions is shown in 5.2.

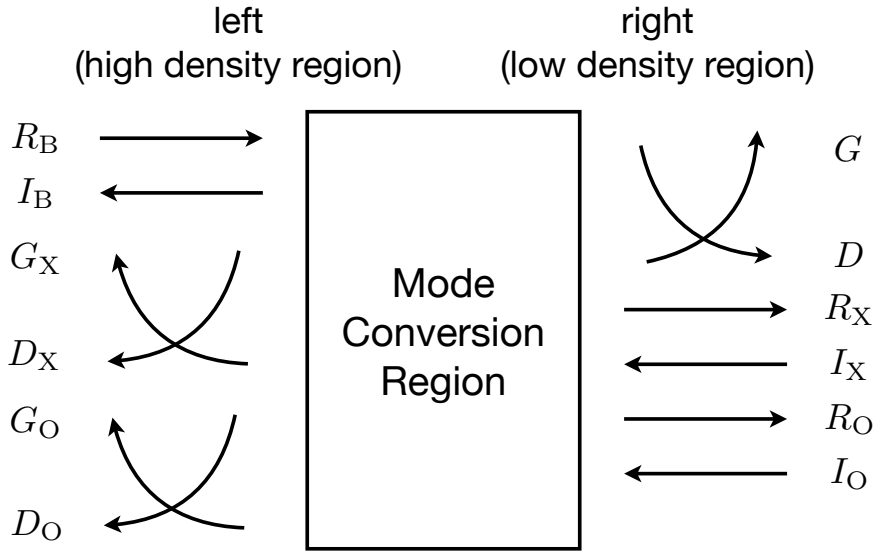

Figure 5.2: A schematic diagram of the boundary conditions. The EBW is indicated by the letter B. The arrows indicate the direction of the energy flow density. The other labels are, respectively, as follows: G and D represent spatially (exponentially) growing and decaying modes, and I and R indicate the inward and outward propagating waves.

The time-averaged energy flow density is given by

$$\langle \boldsymbol{s} \rangle = \frac{1}{4}\sqrt{\frac{\epsilon_0}{\mu_0}}\boldsymbol{F}_{\rm K}^{\dagger} \cdot \boldsymbol{R} \cdot \boldsymbol{F}_{\rm K}\hat{x} \tag{5.14}$$

where the dagger denotes complex conjugate and

$$\boldsymbol{R} = \begin{pmatrix} 0 & 0 & 0 & 1 & 0 & 0 \\ 0 & 0 & 0 & 0 & 1 & 0 \\ 0 & 0 & 0 & 0 & 0 & 1 \\ 1 & 0 & 0 & 0 & 0 & 0 \\ 0 & 1 & 0 & 0 & 0 & 0 \\ 0 & 0 & 1 & 0 & 0 & 0 \end{pmatrix} \tag{5.15}$$

Therefore, the conversion efficiency can be calculated by comparing the time-averaged energy flow density of different eigenmodes at the two boundaries.

The setting parameters of the toroidal magnetic field, electron density and temperature profiles are

$$
\begin{aligned}
B(R) &= 60 \times \frac{\mu_0 I_\mathrm{t}}{2\pi R} \\
n_\mathrm{e}(R) &= \frac{n_\mathrm{core} - n_\mathrm{edge}}{2} \tanh\left(-\frac{R - R_{n_0}}{L_n}\right) + \frac{n_\mathrm{core} + n_\mathrm{edge}}{2} \\
T_\mathrm{e}(R) &= \frac{T_\mathrm{core} - T_\mathrm{edge}}{2} \tanh\left(-\frac{R - R_{T_0}}{L_T}\right) + \frac{T_\mathrm{core} + T_\mathrm{edge}}{2}
\end{aligned}
\tag{5.16}
$$

where $I_\mathrm{t} = 900$ A, $n_\mathrm{core} = 1.8 \times 10^{17}$ m^{-3}, $n_\mathrm{edge} = 3.6 \times 10^{15}$ m^{-3}, $L_n = 5.1$ cm, $T_\mathrm{core} = 7.1$ eV, $T_\mathrm{edge} = 3.7$ eV, $L_T = 3.8$ cm, $R_{n_0} = R_{T_0} = 29.8$ cm. Such parameters are similar to figure 4.3 in the range of $R = 310$ to 380 mm where the PC and UHR layers are included, and 1.5 GHz microwave is injected as O-mode with a parallel refractive index of 0.611. The collisional frequency is $\nu = 5 \times 10^7$ s^{-1}. The calculation results are shown in figure 5.3.

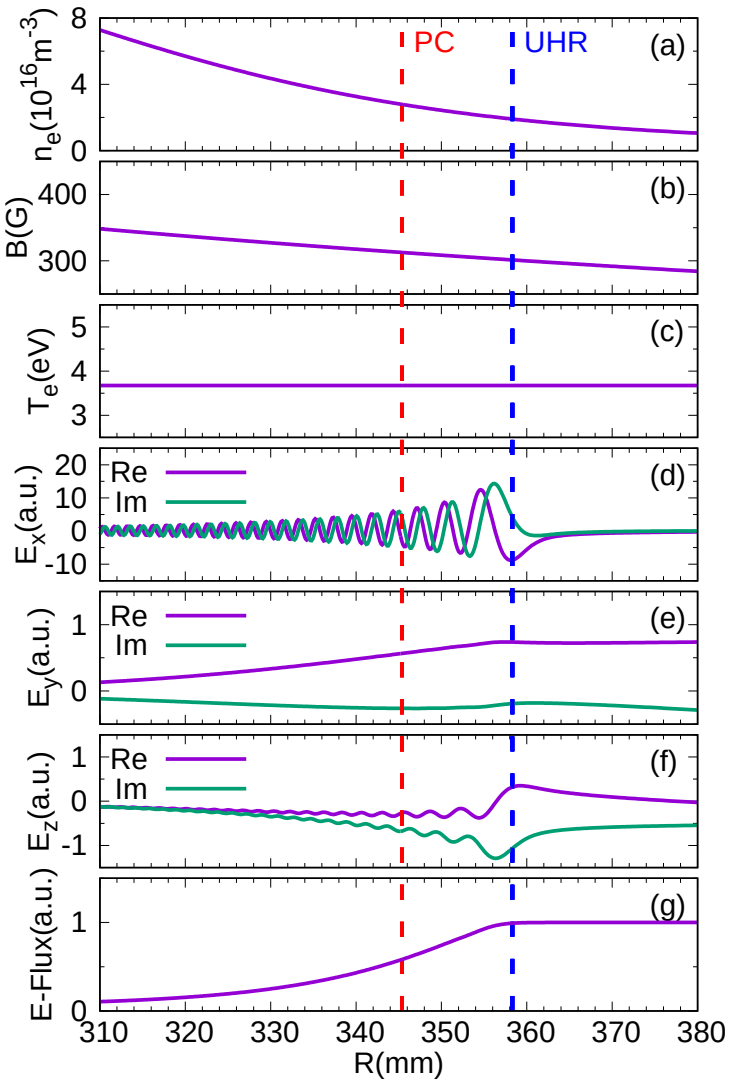

Figure 5.3: 1-D full wave calculation results: (a) the electron density profile, (b) the toroidal magnetic field profile, (c) the electron temperature profile, (d), (e) and (f) real and imaginary part of the wave field E_x, E_y and E_z, (g) the total wave energy flow density. The UHR ($R_{\mathrm{UHR}} = 358.3$ mm) and PC ($R_{\mathrm{PC}} = 345.4$ mm) layers are marked by vertical dashed lines.

From figure 5.3, it is clear that EBW can be excited near the UHR layer under present experimental conditions, and the wavelength is about 2 mm, which is in agreement with measurement results. The reflection rate is cal-

culated to be 10.2%, so the O-X-B mode conversion efficiency is 89.8%. It is also noted that the total wave energy flow density quickly decreases after the UHR layer, due to the collisional damping of EBW, and the damping length is about several centimeters, which is also in agreement with measurement results.

From figure 4.7, it is noted that measured EBW region is about 1 cm inside the UHR layer and highly localized within about 2 cm, while the wavelength of EBW is almost the same in the whole region. However, comparison with figure 5.3 in the same region shows that EBW wavelength should decrease about several tenths of a millimeter from outside to inside, due to the increase of the toroidal magnetic field and electron density. The reason for such difference is not clear. It may be partly because the probe antenna moves in a curve and the angle between the pin direction and wave propagation direction also change as mentioned in chapter 3, although such effects on the EBW wavelength are pretty small as the region is highly localized and the change of directions are also slight.

5.2 Limitations and future plans

Here we discuss some limitations of present experiments and future plans.

First, the five-pin probe antenna itself cannot be rotated in the experiment. There are only two rotation axes in the 2-D mechanical probe driving system, which rotate the pulley box and the arm, while the probe antenna is fixed on the antenna box. Although the probe antenna can cover a large region for 2-D measurement, the detection direction is fixed at each point. Since there may exist multiple electrostatic waves in different directions near the UHR layer, it is difficult to verify the exact portion and direction of each wave as the antenna direction cannot be adjusted.

Second, both the frequency and injection angle of the microwave cannot be adjusted. The waveguide launcher is designed for a pretty narrow frequency band, and the angle between the injection line and 6R port is fixed. Therefore, only 1.5 GHz and 70° are used in present experiments. It is noted that adjusting the toroidal magnetic field will unavoidably change the target plasma, so it is of interest how the wave pattern will change if only the wave frequency and injection angle are adjusted while the target plasma is kept the same.

There are several potential plans for the future experiments.

First, the excitation and detection system can be upgraded. Microwave frequency adjustment, microwave injection angle adjustment, and five-pin probe antenna rotation experiments can be performed.

Second, the X-B mode conversion can be measured directly. The X-B mode conversion process is not fully understood in detail yet, as it always involves wave tunneling but perfect conversion can still be achieved. Besides, EBW trajectory in a spherical tokamak is important.

Third, 3-D kinetic full wave simulation can be developed. Present 1-D simulation cannot reflect 2-D effect in the experiment, and 3-D geometry is considered to be more realistic.

At last, scattering detection of EBW can be compared with antenna detection results. Collective Thompson scattering method is another direct detection method for EBW measurement, and it relies on sub-THz gyrotron development.

Chapter 6

Summary

In order to detect the wave pattern of electron Bernstein waves (EBWs), an excitation and detection system has been developed in Low Aspect ratio Torus Experiment (LATE). The system consists of a waveguide launcher with arbitrary polarization, a specially designed five-pin probe antenna, a two-dimensional (2-D) mechanical probe driving system, and a homodyne-type mixer circuit. The system has been tested in the air and shows reliable results.

By using the excitation and detection system, the 2-D wave pattern of phase and amplitude has been directly measured in LATE, for an overdense ECR plasma with 1.5 GHz microwave obliquely injected. The electron density and temperature profiles are measured by using a movable Langmuir probe and two 70 GHz microwave interferometers.

In the case of O-mode injection, an EBW-like wave pattern has been detected for the first time, in a localized region (30×35 mm) near the UHR layer. 1-D variation of phase shows that the pattern has a short wavelength of about 2 mm, the pattern is backward as the phase velocity direction is opposite to the group velocity direction, and the pattern is electrostatic as the pin detection direction is nearly the same as the wave propagation direction (both almost radial). All these characteristics suggest that EBW has been directly observed. The pattern only appears in several sweeps and lasts for several centimeters in each sweep. The reason for localized observation of the EBW wave pattern is considered to be the critical requirement for achieving high O-X-B mode conversion efficiency, and high collisional damping rate of EBW. The parallel refractive index of the injected microwave has a wide distribution at the PC layer due to its curvature, and the LC layer is not parallel to the PC layer in contrast to conventional 1-D case, therefore, EBW can only be excited in a localized region near the intersection point between the PC layer and the LC layer. Under present warm plasma conditions

with the electron temperature of 4 eV and gas pressure of 0.6×10^{-2} Pa, the collision frequency is at 5×10^7 s^{-1} level, and the complex value of the perpendicular wave number solved from the general EBW dispersion relation is $k_\perp = 2679.5 - 334.5i$ m^{-1}, so the collisional damping length of EBW is estimated to be about several centimeters in present experiments. Amplitude variation shows similar periods as phase variation, which indicates that the wave potential forms an interference wave pattern rather than a pure plane wave. In the experiment, the density fluctuation effect cannot be neglected, and the UHR layer is not expected to be smooth, so there may exist multiple electrostatic waves in different directions near the UHR layer, which could form the interference wave pattern and result in such amplitude variation.

In the case of X-mode injection, 2-D wave pattern is quite different from O-mode injection case, although the electron density and temperature profiles are almost the same. For phase pattern, no short-wavelength wave pattern can be observed. Under present experimental conditions, the X-B mode conversion efficiency is at a very low level and EBW is not expected to be excited effectively. For amplitude pattern, the overall amplitude level is smaller than O-mode injection case, as FX-mode is quickly blocked at the RC layer and cannot penetrate inside the plasma. A standing wave pattern appears near the wall ($R = 380$ to 460 mm) with a wavelength of about 15 cm, due to the reflection of the FX-mode between the RC layer and the 4R and 5R ports of LATE.

By slightly adjusting the toroidal magnetic field coil current from 900 A to 920 A in O-mode injection, while keeping other control parameters the same, it is found that both the position and size of the localized EBW region have changed. The position of the EBW region moves not only radially but also toroidally, due to the movement of the intersection point between the PC layer and the LC layer where O-X conversion efficiency is high, and the change of wave trajectory which passes through this point, propagates back to the UHR layer and eventually converts to EBW. The size of the EBW region becomes slightly smaller as there are fewer sweeps where the EBW wave pattern is clearly observed in 920 A case. While the EBW collisional damping length is calculated to be nearly the same as in 900 A case, the total O-X-B conversion efficiency cannot be precisely calculated in present 2-D case, which depends on both the evanescent region shape and the wave energy spatial distribution. It is noted that, however, the EBW wave pattern can still be observed for much higher toroidal magnetic field coil current 1000 A. Such results suggest that localized efficient O-X-B conversion can always be achieved in present 2-D case due to the existence of the intersection point, while the total conversion efficiency may be different.

For comparison with experimental results, 1-D full wave simulation is

performed by solving the simplified kinetic full wave equation. ω in $\widetilde{\chi}$ is replaced with $\omega + i\nu$ to include the EBW collisional damping effect, and the setting parameters of the toroidal magnetic field, electron density and temperature profiles are similar to 900 A O-mode injection case. Comparison between the simulation results and the experimental results confirm that EBW can be excited near the UHR layer under present conditions with a high O-X-B conversion efficiency of 89.8%, and the EBW wavelength is about 2 mm. The collisional damping of EBW is also confirmed as the total wave energy flow density quickly decreases after the UHR layer, and the damping length is about several centimeters.

The present excitation and detection system can be upgraded in the future, for microwave frequency adjustment, microwave injection angle adjustment, and five-pin probe antenna rotation experiments. The X-B mode conversion process can also be measured directly with perpendicular injection and steep density profile.

Bibliography

[1] Dudley B 2019 *BP Statistical Review of World Energy*

[2] Wesson J *et al* 2011 *Tokamaks* (London: Oxford University Press)

[3] Sykes A 2008 ICPP Fukuoka

[4] Peng Y K M 1984 ORNL/FEDC-87/7

[5] Prater R 2004 *Phys. Plasmas* **11** 2349

[6] Laqua H P 2007 *Plasma Phys. Control. Fusion* **49** R1

[7] Bernstein I B 1958 *Phys. Rev.* **109** 10

[8] Laqua H P *et al* 1997 *Phys. Rev. Lett.* **78** 3467

[9] Igami H *et al* 2006 *Rev. Sci. Instrum.* **77** 10E931

[10] Yoshimura Y *et al* 2007 *Fusion. Sci. Technol.* **52** 216

[11] Mueck A *et al* 2007 *Phys. Rev. Lett.* **98** 175004

[12] Podoba Y Y *et al* 2007 *Phys. Rev. Lett.* **98** 255003

[13] Shevchenko V *et al* 2007 *Fusion. Sci. Technol.* **52** 202

[14] Uchida M *et al* 2010 *Phys. Rev. Lett.* **104** 065001

[15] Maekawa T *et al* 2001 *Phys. Rev. Lett.* **86** 3783

[16] Shevchenko V *et al* 2002 *Phys. Rev. Lett.* **89** 265005

[17] Igami H *et al* 2009 *Nuc. Fusion* **49** 115005

[18] Shevchenko V *et al* 2010 *Nuc. Fusion* **50** 022004

[19] Shiraiwa S *et al* 2006 *Phys. Rev. Lett.* **96** 185003

[20] Seltzman A *et al* 2017 *Phys. Rev. Lett.* **119** 185001

[21] Sugai H 1981 *Phys. Rev. Lett.* **47** 1899

[22] Uchijima K *et al* 2015 *Plasma Phys. Control. Fusion* **57** 065003

[23] Ram A K and Schultz S D 2000 *Phys. Plasmas* **7** 4084

[24] Preinhaelter J and Kopecký V 1973 *J. Plasma Phys.* **10** 1

[25] Mjølhus E 1984 *J. Plasma Phys.* **31** 7

[26] Maekawa T *et al* 2005 *Nuc. Fusion* **45** 1439

[27] Kuroda K *et al* 2016 *Plasma Phys. Control. Fusion* **58** 025013

[28] Stix T H 1992 *Waves in Plasmas* (New York: American Institute of Physics)

[29] Pešić S 1984 *Physica B+C* **125** 118

[30] Richardson A S 2019 *NRL Plasma Formulary* (Washington: U.S. Naval Research Laboratory)

[31] Igami H *et al* 2003 *Plasma Phys. Control. Fusion* **46** 261

[32] Igami H *et al* 2006 *Plasma Phys. Control. Fusion* **48** 573

Acknowledgement

First, I would like to thank my advisor, Prof. Hitoshi Tanaka, for his continuous support during my Ph.D. study. His guidance carried me through all the stages of conducting research and writing papers.

Next, I would like to thank Mr. Ryo Ashida, who helped me all the way from experimental preparation to data analysis. His contribution to this work must be acknowledged.

I would like to thank Mr. Yoshitaka Nozawa and Mr. Ryusuke Kajita, who helped me not only in research, but also in my daily life in Japan.

I would like to thank Prof. Takashi Maekawa and Prof. Masaki Uchida, for their valuable comments on the research and papers.

I would like to thank all the other members in the LATE laboratory, Mr. Haruka Shirai, Mr. Yuji Omura, Mr. Yosuke Sakai, Mr. Wataru Tsukamoto, Mr. Junki Ootani, Mr. Keisuke Goto, Mr. Tetsuo Noguchi, Mr. Takahiro Nakai, Mr. Sanshiro Matsui, Mr. Shuhei Yamagata, Mr. Tetsuto Kuzuma, Mr. Ryotaro Nakai, Mr. Takumi Nagaeki, Mr. Yuuki Ideta, Mr. Shintaro Yoshioka, Mr. Wataru Ootaka, Mr. Shohei Ozaki, Mr. Mutsuhiro Hamaguchi, and our secretary, Ms. Komane Tanaka. They gave me so much help at different time periods during my four-year study in this laboratory. Thank you all!

At last, I would like to thank my family, for their continuous understanding and support.

List of Publications

Journal Publications

- **Xingyu Guo**, Zhe Gao and Guozhang Jia. "One-dimensional ordinary–slow extraordinary–Bernstein mode conversion in the electron cyclotron range of frequencies." *Plasma Science and Technology* 19 (2017): 085101.

- **Xingyu Guo**, Ryo Ashida, Yuto Noguchi, Ryusuke Kajita, Hitoshi Tanaka, Masaki Uchida and Takashi Maekawa. "Development of an Excitation and Detection System of Electron Bernstein Waves in LATE." *Plasma Fusion Res.* (2022) accepted and in press.

- **Xingyu Guo**, Ryo Ashida, Yuto Noguchi, Ryusuke Kajita, Hitoshi Tanaka, Masaki Uchida and Takashi Maekawa. "Direct measurement of electron Bernstein waves in Low Aspect ratio Torus Experiment (LATE)." *Plasma Phys. Control. Fusion* 64 (2022): 035008.

Academic Conferences

- **Xingyu Guo**, Ryo Ashida, Yoshitaka Nozawa, Ryusuke Kajita, Takahiro Nakai, Sanshiro Matsui, Shuhei Yamagata, Tetsuto Kuzuma, Ryotaro Nakai, Takumi Nagaeki, Hitoshi Tanaka, Masaki Uchida and Takashi Maekawa. "Development of A Direct Detection System of Electron Bernstein Waves on LATE." JSPF Annual Meeting 2019

- **Xingyu Guo**, Ryo Ashida, Yoshitaka Nozawa, Ryusuke Kajita, Ryotaro Nakai, Takumi Nagaeki, Yuuki Ideta, Shintaro Yoshioka, Hitoshi Tanaka, Masaki Uchida and Takashi Maekawa. "Direct Measurement of Electron Bernstein Waves on LATE Device." Experimental Research Group Program for Advanced Tokamak Development 2020

- **Xingyu Guo**, Ryo Ashida, Yoshitaka Nozawa, Ryusuke Kajita, Ryotaro Nakai, Takumi Nagaeki, Masaki Uchida, Hitoshi Tanaka and Takashi Maekawa. "Measurement of Mode-Conversion Process to Electron Bernstein Waves in Low Aspect ratio Torus Experiment." The 29th International Toki Conference 2020

- **Xingyu Guo**, Ryo Ashida, Yoshitaka Nozawa, Ryusuke Kajita, Ryotaro Nakai, Takumi Nagaeki, Yuuki Ideta, Shintaro Yoshioka, Hitoshi Tanaka, Masaki Uchida and Takashi Maekawa. "Experimental Result on Direct Measurement of Electron Bernstein Waves in LATE." JSPF Annual Meeting 2020

- **Xingyu Guo**, Ryusuke Kajita, Yuuki Ideta, Shintaro Yoshioka, Wataru Ootaka, Shohei Ozaki, Mutsuhiro Hamaguchi, Masaki Uchida, Hitoshi Tanaka and Takashi Maekawa. "Two-dimensional Measurement of Wave Pattern for Mode Conversion and EBW Verification in LATE." JSPF Annual Meeting 2021 (**Young Scientist Presentation Award**)